Aus der

Medizinischen Klinik und Poliklinik II

Klinikum der Ludwig-Maximilians-Universität München

Comparative analysis of Rho-GTPase pathway dynamics and epigenetic drug responses in subtype-specific pancreatic cancer cell lines

Dissertation
zum Erwerb des Doctor of Philosophy (Ph.D.)
an der Medizinischen Fakultät
der Ludwig-Maximilians-Universität München

vorgelegt von
Quan Zhou

aus
Benxi / China

Jahr
2024

Mit Genehmigung der Medizinischen Fakultät der
Ludwig-Maximilians-Universität München

Erstes Gutachten:	Priv. Doz. Dr. Ivonne Regel
Zweites Gutachten:	Prof. Dr. Roland Kappler
Drittes Gutachten:	Prof. Dr. Iris Helfrich
Viertes Gutachten:	Priv. Doz. Dr. Barbara Mayer

Dekan: Prof. Dr. med. Thomas Gudermann

Tag der mündlichen Prüfung: 05.12.2024

Table of content

Publication

Parts of the present doctoral thesis are published:

Zhou Q, Pichlmeier S, Denz AM, Schreiner N, Straub T, Benitz S, Wolff J, Fahr L, Del Socorro Escobar Lopez M, Kleeff J, Mayerle J, Mahajan UM, Regel I. Altered histone acetylation patterns in pancreatic cancer cell lines induce subtype-specific transcriptomic and phenotypical changes. Int J Oncol. 2024 Mar;64(3):26. doi: 10.3892/ijo.2024.5614. Epub 2024 Jan 19. PMID: 38240084; PMCID: PMC10807649.

Abstract (English)

Background: Pancreatic ductal adenocarcinoma (PDAC) is commonly detected at advanced stages, with chemotherapy being the main treatment possibility. Large-scale gene expression studies have identified two major PDAC subtypes, a classical and a basal-like subtype, characterized by an epithelial and mesenchymal phenotype, respectively, that are additionally associated with changes in cytoskeleton organization. The specific transcriptional networks of these subtypes are regulated by epigenetic modifications. Considering the reversible nature of cytoskeleton organization and epigenetic modifications, the presented study aims to explore whether human PDAC cell lines can undergo a subtype-specific reprogramming of cytoskeleton organization and epigenetic modifications towards a less aggressive phenotype.

Method: Transcriptional profiles from seven human PDAC cell lines were generated by RNA-sequencing (RNA-seq) to classify the cell lines into a classical and basal-like phenotype. Differentially expressed genes, which are important in regulating epithelial-to-mesenchymal transition (EMT), and cytoskeletal organization as well as Rho-GTPase/ROCK pathway activity, were determined by chromatin-immunoprecipitation (ChIP) followed by qPCR for their histone acetylation status. Differences in Rho-GTPase/ROCK pathway activity were assessed in classical and basal-like cell lines by immunoblot analysis. A ROCK-inhibitor as well as histone acetyltransferase (HAT) and histone deacetylase (HDAC) inhibitors were tested as therapeutic options to induce phenotypical changes towards a less aggressive cancer phenotype.

Results: The PDAC cell lines were classified into classical and basal-like subtypes using RNA sequencing and bioinformatic approaches. Classical cell lines exhibited higher expression of epithelial markers and showed enriched H3K27ac at their promoters, while basal-like cell lines had reduced overall histone acetylation levels and increased HDAC2 activity. Basal-like cell lines also demonstrated significant cytoskeletal changes, including increased stress fiber formation, regulated by the Rho-GTPase/ROCK pathway, although ROCK inhibition did not show any treatment effects at the used conditions. Treatment with a HAT inhibitor led to a more aggressive tumor phenotype of classical PDAC cells, marked by the loss of epithelial markers, higher EMT scores, and enhanced cell migration. In contrast, HDAC inhibitors had minimal effects on the reprogramming of both subtypes.

Conclusion: The study highlights a crucial role of epigenetic regulation in PDAC subtypes and driving EMT characteristics, particularly through the RhoA-GTPase/ROCK pathway, which significantly influences EMT and cytoskeletal dynamics in basal-like PDAC cell lines. The distinct and heterogeneous cellular responses to HAT and HDAC

inhibitors between the two subtypes further emphasize the need for subtype-specific epigenetic therapies. Targeting epigenetic modifications could provide a strategic approach to mitigating tumor aggressiveness.

List of figures

List of tables

List of abbreviations

%	Percent
°C	Degree celsius
4-PB	4-phenylbutyrate
Ac	Acetylation
ACTA2	actin alpha 2, smooth muscle
ADEX	Aberrantly differentiated endocrine-exocrine
ADT	Androgen deprivation therapy
AFP	Alpha-fetoprotein
AR	Androgen receptor
ARHGDIB	Rho GDP dissociationinhibitor beta
Arp2/3	actin-related protein 2/3
Beleodaq/PXD101	Belinostat
BHLHA15A	basic helix-loop-helix family member a15
bp	Base pair
BRCA1/2	BRCA1/2 DNA Repair Associated
BRDs	bromodomains
BSC	Biological safety cabinets
CA19-9	Carbohydrate antigen 19-9
CAF	cell lines and cancer associated fibroblast
CBP	CREB binding protein
CCS1477	inobrodib
CDC42	Cell division cycle 42
CDH1	cadherin 1
CDH2	cadherin 2
CDKN2A	Cyclin dependent kinase inhibitor 2A
cDNA	Complementary DNA
CDX2	Caudal type homeobox 2
CFAP54	cilia and flagella associated protein 54
ChIP	Chromatin immunoprecipitation
Citron	Citron kinase
cm^2	Square centimeter
CoREST	REST corepressor 1
CREBBP	CREB binding protein
CST6	cystatin E/M
CT	Computed Tomography
CTCs	Circulating tumor cells
ctDNA	Circulating tumor DNA
CXCR4	C-X-C motif chemokine receptor 4
dCK	Deoxycytidine kinase
DEGs	Differentially-expressed genes
DES	desmin
dH_2O	Distilled water
ddH_2O	Double distilled water
DMR	DNA mismatch repair
DNA	Deoxyribonucleic Acid
DRC1	dynein regulatory complex subunit 1

ECM	Extensive extracellular matrix
ECOG	Eastern Cooperative Oncology Group
EGFR	Epidermal growth factor receptor
EIF5A	eukaryotic translation initiation factor 5A
ELF3	E74 like ETS transcription factor 3
EMP	Epithelial-mesenchymal plasticity
EMT	Epithelial-to-mesenchymal transition
EMT-TFs	transcription factors related to EMT
EP300	E1A binding protein p300
EPCAM	epithelial cell adhesion molecule
ERBB2	erb-b2 receptor tyrosine kinase 2
ERBB3	erb-b2 receptor tyrosine kinase 3
EUS-FNB	Endoscopic ultrasound-guided fine-needle biopsy
F-actin	Filamentous actin
FAP	fibroblast activation protein alpha
FDA	U.S. Food and Drug Administration
FFPE	formalin-fixed paraffin-embedded
FOLFIRINOX	a combination of 5-FU, leucovorin, irinotecan, and oxaliplatin
FOS	Fos proto-oncogene, AP-1 transcription factor subunit
FOXA2/3	forkhead box A2/3
FOXJ1	forkhead box J1
FOXP1	forkhead box P1
FOXP4	forkhead box P4
FOXO1	forkhead box O1
GAPs	GTPase-activating proteins
GATA6	GATA binding protein 6
GDIs	Guanine-nucleotide dissociation inhibitors
GEFs	Guanine-nucleotide exchange factors
Gemcitabine	2′,2′-difluorodeoxycytidine
GN	A combination of gemcitabine and albumin nanoparticle conjugate of paclitaxel
GNAT	GCN5-related N-acetyltransferase
GO	Gene Ontology
GR	Growth rate
GSEA	Gene set enrichment analysis
GTPases	Small guanine triphosphatases
H1	Histon H1
H2A	Histon H2A
H2AK119Ub1	Monoubiquitination of histone H2A at lysine119
H2B	Histon H2B
H3	Histon H3
H3K18ac	Acetylation of histone 3 at lysine 18
H3K27ac	Acetylation of histone 3 at lysine 27
H3K27me3	Trimethylation of histone 3 at lysine 27
H3K36me3	Trimethylation of histone 3 at lysine 36
H3K4me3	Trimethylation of histone 3 at lysine 4
H3K79me3	Trimethylation of histone 3 at lysine 79

H3K9ac	Acetylation of histone 3 at lysine 9
H3K9me2	Dimethylation of histone 3 at lysine 9
H3K9me3	Trimethylation of histone 3 at lysine 9
H4	Histon H4
H4K16ac	Acetylation of histone 4 at lysine 16
H4K20me3	Trimethylation of histone 4 at lysine 20
HATi	histone acetyltransferase inhibitor
HATs	Histone acetyltransferases
HCC	Hepatocellular carcinoma
HDACi	histone deacetylase inhibitor
HDACs	Histone deacetylases
hENT1	human equilibrative nucleoside transporter 1
HNF4A	hepatocyte nuclear factor 4 alpha
IF	Immunofluorescence
IFN	Interferon
IgG	Immunoglobin G
IL-6	Interleukin-6
INS	insulin
IRSp53	Insulin receptor tyrosine kinase substrate p53
KDM6A	Lysine demethylase 6A
KEGG	Kyoto Encyclopedia of Genes and Genomes
KLF10	KLF transcription factor 10
KLF4	KLF transcription factor 4
KLF5	KLF transcription factor 5
KRAS	KRAS proto-oncogene, GTPase
KRT14	keratin 14
KRT5	keratin 5
KRT6A	keratin 6A
KRT6B	keratin 6B
LCM	Laser capture microdissection
MAFA	MAF bZIP transcription factor A
MDCT	Multi-detector row computed tomography
mDia	mammalian Diaphanous-related formin
Me	Methylation
MET	mesenchymal-to- epithelial transition
MiDAC	Mitotic deacetylase complex
miRNAs	MicroRNAs
Mnase	Micrococcal nuclease
MNX1	Motor neuron and pancreas homeobox 1
MRCK	myotonic dystrophy kinase-related Cdc42-binding kinase
MRCP	Magnetic resonance cholangiopancreatography
MRI	Resonance Imaging
mRNA	Messenger RNA
MSI-H	Microsatellite instability
Myc	MYC proto-oncogene, BHLH transcription factor
NADPH	Nicotinamide adenine dinucleotide phosphate
NCI	National Cancer Institute

NES	Nuclear export signal
NEUROD1	neuronal differentiation 1
ng	Nanogram
NKX2-2	NK2 homeobox 2
NLS	Nuclear import signals
nm	Nanometer
NMF	Non-negative Matrix Factorization
NOXA	BH3-only protein NOXA
NR5A2	nuclear receptor subfamily 5 group A member 2
NTRK1-3	neurotrophic receptor tyrosine kinase 1-3
NuRD	Nucleosome remodeling and deacetylase
OD	Optical density
OS	Overall survival
p300/CBP	p300/CREB-binding protein
PAK	P21-activated kinase
PALB2	Partner and localizer of BRCA2
PBX1	PBX homeobox 1
PCA	Principal Component Analysis
PDAC	pancreatic ductal adenocarcinoma
PDOs	patient-derived organoids
PDTXs	patient-derived tumor xenografts
PDX	patient-derived xenografts
PDX1	Pancreatic and duodenal homeobox 1
PET	Positron Emission Tomography
PFA	PBS-buffered formaldehyde
PH	Pleckstrin homology
pH	Potential of Hydrogen
PKN	Protein kinase N
PS	performance status
PTMs	Post-translational modifications
QM-PDA	quasi-mesenchymal
qPCR	Quantitative real-time PCR
RAC1	Rac family small GTPase 1
RBD	Rho-binding domain
RBPJL	recombination signal binding protein for immunoglobulin kappa J region like
RHOA	Ras Homolog Family Member A
RHOBTB2	Rho Related BTB Domain Containing 2
RIN	RNA integrity number
Ring1A	Ring finger protein 1A
Ring1B	Ring finger protein 1B
RNA	Ribonucleic Acid
RNA-seq	RNA sequencing
RND3	Rho family GTPase 3
ROCK	Rho associated coiled-coil containing protein kinase
ROS1	ROS proto-oncogene 1, receptor tyrosine kinase
RRM1	ribonucleotide reductase subunit 1

RT	Room temperature
s	Second
S	Svedberg units
S100A2	S100 calcium binding protein A2
SAHA	Vorinostat
SEs	Super enhancers
SDS-PAGE	SDS polyacrylamide gel electrophoresis
Sin3	Switch-independent 3
Slug	Snail family transcriptional repressor 2
SMAD	SMAD family member
SMAD4	SMAD family member 4
Snail1	Snail family transcriptional repressor 1
SOX2	SRY-box transcription factor 2
SPARC	secreted protein acidic and cysteine rich
TBP	TATA box binding protein
TFF1	trefoil factor 1
TFs	transcription factors
TFIID	Transcription factor II D
TGF-β	Transforming growth factor β
TP53	Tumor protein P53
TRAIL	Tumor necrosis factor-related apoptosis-inducing ligand
TSA	Trichostatin A
Twist1/2	Basic helix-loop-helix transcription factor family's Twist1/2
U	Unit
US	Ultrasonography
UV	Ultraviolet
v/v	Volume concentration
VIM	vimentin
VPA	Valproic acid
w/v	Mass concentration
WASP	Wiskott-Aldrich syndrome protein
WAVE	WASP-family verprolin-homologous protein
xg	Times gravity
ZBBX	zinc finger B-box domain containing
ZEB1/2	Zinc finger E-box binding homeobox family's ZEB1/2
µg	Microgram
µl	Microliter
µM	Micromolar

1. Introduction

1.1 Epidemiology, diagnosis and treatment status of pancreatic ductal adenocarcinoma

Pancreatic ductal adenocarcinoma (PDAC) is the most common type of pancreatic cancer, contributing to 90% of all pancreatic cancer diagnoses. Tumor formation occurs predominantly in the head of the pancreas [1]. Smoking, drinking, obesity, chronic pancreatitis, and hereditary syndromes are recognized as risk factors for PDAC [2]. Despite PDAC accounts only for 3.3% of all new cancer cases in the United States, its incidence rate is increasing by approximately 0.9% per year. Moreover, it has a poor five-year survival rate of only 13% [3]. According to the report by the National Cancer Institute (NCI), PDAC is currently the third most prevalent cause of cancer-related mortality in the United States. It is anticipated to rise to the second position in the upcoming years [3]. The situation in Europe presents a similarly dismal perspective. Although the annual incidence rate of PDAC remains consistent at 6.85 per 100,000 individuals [4], PDAC is currently the fourth leading cause of cancer-related deaths in Europe, with projections indicating it will become the second leading cause of cancer-related deaths within the next four years [5].

Early detection of PDAC, appropriate selection of surgical candidates, and improvements in patient prognosis are key to increasing PDAC survival rates. However, several factors contribute to the challenge of early PDAC detection, including nonspecific symptoms, the absence of effective diagnostic biomarkers, and the high cost of imaging examinations. Non-invasive serological testing is considered an ideal method for the early diagnosis of tumors. Currently, CA19-9 (Carbohydrate antigen 19-9) is the most valuable serological biomarker for PDAC and used for monitoring treatment efficacy and detecting recurrence. Unfortunately, its specificity is limited as it can also be elevated in various gastrointestinal tumors and benign gastrointestinal conditions, such as obstructive jaundice, making it unsuitable for screening for PDAC [6]. Additionally, CA19-9 demonstrates moderate sensitivity and specificity for monitoring PDAC recurrence post-surgery, with efficiencies of 79% and 82%, respectively [7]. Moreover, markers such as circulating tumor cells (CTCs), cell-free tumor DNA (ctDNA), microRNAs (miRNAs), and exosomes are being investigated in experimental and clinical studies. Nonetheless, these markers currently exhibit a specificity of less than 70%, and their low concentrations in the blood, coupled with the lack of effective enrichment methods, render them inadequate for PDAC diagnosis at present [8]. Early identification of PDAC predominantly relies on imaging diagnostics. Techniques such as Magnetic Resonance

Imaging (MRI), Ultrasonography (US), Computed Tomography (CT), and Positron Emission Tomography (PET) provide the highest sensitivity and specificity for PDAC screening [9]. While imaging diagnostics are beneficial for high-risk populations, such as those with hereditary PDAC, their application is not feasible for the general population due to the relatively low incidence of PDAC.

Only 20% of PDAC patients are considered appropriate for surgery at initial diagnosis, and 80% of these patients experience relapse and metastasis post-surgery, contributing to the high mortality rate associated with PDAC [10]. Distant metastases and vascular invasion are major challenges in the surgical resection of PDAC. Additionally, its anatomical proximity to major vascular systems like the portal vein, superior mesenteric vein and artery, and common hepatic artery complicates surgical resection due to extensive vascular involvement and the risk of vascular occlusion [11]. Therefore, imaging can assist in the proper selection of surgical candidates. Endoscopic ultrasound-guided fine-needle biopsy (EUS-FNB) is optimal for diagnosing small tumors, especially those smaller than 3 cm [12]. Multi-detector row computed tomography (MDCT) is excellent for evaluating vascular involvement [13]. PET scans are effective in assessing tumor metastasis [14], and magnetic resonance cholangiopancreatography (MRCP) efficiently identifies tumors in the pancreatic head, where duct dilation and obstruction indicate pancreatic or ampullary cancer [15]. The Clinical Practice Guidelines for PDAC indicate that neoadjuvant chemotherapy can reduce tumor stage and increase the chances of surgical success [16]. However, there is controversy regarding its impact on patient prognosis.

Chemotherapy is the primary option for unresectable locally advanced or metastatic PDAC. The main chemotherapy strategies for advanced PDAC patients in clinical practice depend among other factors on the patient's Eastern Cooperative Oncology Group (ECOG) performance status (PS) score. Patients with scores of 0 or 1 are eligible to receive intensive treatments such as FOLFIRINOX (a combination of 5-FU, leucovorin, irinotecan, and oxaliplatin) and GN (a combination of gemcitabine and albumin nanoparticle conjugate of paclitaxel). Patients with an ECOG PS score of 2, who are not suitable for more toxic chemotherapy strategies, are treated with gemcitabine alone [17]. According to the NCI report, the median overall survival (OS) for locally advanced and metastatic PDAC was around 6.7 months with gemcitabine treatment, 11.1 months with FOLFIRINOX treatment, and 8.5 months with GN treatment [18]. Although Gemcitabine (2′,2′-difluorodeoxycytidine) is the predominant chemotherapy regimen utilized for

treating PDAC, the resistance to gemcitabine remains a significant challenge in PDAC treatment as compared to other chemotherapeutic agents.

In addition, combining first-line therapy with targeted therapy for PDAC can enhance prognosis. Patients with mutations in *BRCA1/2* (BRCA1/2 DNA repair associated) and *PALB2* (partner and localizer of BRCA2) genes demonstrate a greater positive reaction to platinum-containing treatment [19]. Patients who have gene fusions involving *NTRK1-3* (neurotrophic receptor tyrosine kinase 1-3) or *ROS1* (ROS proto-oncogene 1, receptor tyrosine kinase) have been found to respond to specific inhibitors that target TRK and ROS1, such as larotrectinib and entrectinib [20]. Furthermore, patients who have a deficiency in DNA mismatch repair (DMR) and have high levels of microsatellite instability (MSI-H) exhibit a favorable response to the immune checkpoint inhibitor Pembrolizumab [21]. However, the proportion of PDAC patients who benefit from these approaches are still limited. The mutation rate is around 1.5% for *BRCA1/2* and 0.54% for *PALB2* [22]. Similarly, *NTRK1-3* and *ROS1* fusions occurs in less than 1% of advanced PDAC cases [23]. DMR and MSI was identified in 1–2% of resectable PDAC patients [24]. In general, early diagnostic markers of PDAC are not existing, and the efficacy of chemotherapy drugs and targeted therapies for advanced PDAC is still too low. Therefore, there is an urgent need for improvements in diagnosis and more effective treatment strategies.

1.2 Molecular subtypes of pancreatic ductal adenocarcinoma

Tumor heterogeneity, including variations in tumor cells and the tumor microenvironment, presents a significant challenge in chemotherapy for solid tumors. Molecular classification, which is based on genomic, epigenomic, transcriptomic, proteomic, and metabolic profiling, is essential for discerning tumor characteristics, optimizing chemotherapy strategies, stratifying patient risk, and directing clinical management. Initially, the transcriptomic classification was based on microarray technology, the advent of high-throughput transcriptomics has since fostered a more comprehensive and precise understanding of tumor tissue composition through molecular subtypes. Collisson et al. were the first to describe transcriptome subtypes in PDAC [25]. They conducted a comprehensive transcriptomic analysis of human primary resected PDAC tissues by using mRNA-arrays that revealed three distinct subtypes of PDAC: **classical subtype** with increased expression of adhesion and epithelial-related genes; **quasi-mesenchymal (QM-PDA) subtype** showing increased expression of mesenchymal genes; and **exocrine-like subtype** with high expression of tumor cell-derived genes encoding for digestive enzymes. Furthermore, the endodermal lineage-specific transcription factor *GATA6* (GATA binding protein 6) was shown to be related with the

classical subtype, as confirmed in human PDAC cell lines and mouse models [25]. Moffitt et al. then used an optimized transcriptional profiling analysis method and Non-negative Matrix Factorization (NMF) to virtually microdissect bulk tumor tissue into tumor cells and stroma compartments [26]. Transcriptional profiling from microarray data of primary and metastatic PDAC samples, PDAC cell lines and normal adjacent pancreas from distant site were assessed. They verified their finding by performing RNA sequencing on primary PDAC, PDAC patient-derived xenografts (PDX), cell lines and cancer-associated fibroblast (CAF) cell lines derived from PDAC patients. The authors performed a NMF analysis of the complex tumor tissue, categorizing the bulk tumor tissues into normal, tumor, and stroma types, and classified tumor types into a **classical subtype**, similar to the classical subtype defined by Collison et al. and a **basal-like subtype**, which mainly expresses genes like laminin and keratin. Furthermore, the stroma type was also divided into two stromal subtypes: **normal stromal subtype**, characterized by high expression of *ACTA2* (actin alpha 2, smooth muscle), *VIM* (vimentin), and *DES* (desmin), and the **activated stromal subtype**, characterized by expression of genes associated with macrophages [26]. Bailey et al. analyzed RNA-seq data from bulk tumor tissue with epithelial content over 40% and identified four distinct PDAC subtypes: **squamous**, **pancreatic progenitor**, **aberrantly differentiated endocrine-exocrine (ADEX)**, and **immunogenic** [27]. The squamous subtype exhibited the expression of ΔNp63, an isoform of p63 characteristic of squamous epithelia, and decreased expression of pancreatic development-related genes. The pancreatic progenitor subtype exhibited elevated expression of early pancreatic development genes, such as *FOXA2/3* (forkhead box A2/3), *PDX1* (pancreatic and duodenal homeobox 1), and *MNX1* (motor neuron and pancreas homeobox 1). Additionally, the ADEX subtype was identified by two upregulated gene networks, associated with transcription factors of acinar cell differentiation, such as *NR5A2* (nuclear receptor subfamily 5 group A member 2), *BHLHA15A* (basic helix-loop-helix family member a15) and *RBPJL* (recombination signal binding protein for immunoglobulin kappa J region like), and another network related to endocrine differentiation, including *INS* (insulin), *NEUROD1* (neuronal differentiation 1), *NKX2-2* (NK2 homeobox 2) and *MAFA* (MAF bZIP transcription factor A) gene expression. The immunogenic subtype was linked to the presence of substantial immune infiltration [27]. Puleo et al. examined the transcriptome of PDAC samples from formalin-fixed paraffin-embedded (FFPE) blocks [28]. They identified also a **classical** and **basal-like** subtype in samples with high-tumor cellularity. In the classical subtype, genes such as *HNF4A* (hepatocyte nuclear factor 4 alpha), *TFF1* (trefoil factor 1), and *GATA6* were highly expressed. In contrast, the basal-like subtype showed enhanced gene expression for *S100A2* (S100 calcium binding protein A2) and *EGFR* (epidermal growth factor

receptor). Furthermore, tumor tissue samples with a low tumor cellularity were categorized into five subtypes based on transcriptome data: **pure classical**, **immune classical**, **desmoplastic**, **stroma activated**, and **pure basal-like**. The first two subtypes demonstrated classical/progenitor characteristics, for which the pure classical was identified with a low stromal signal, whereas the immune classical subtype was associated with increased immune infiltrates. The remaining three subtypes exhibited basal-like/stromal features. The desmoplastic subtype was characterized by its elevated expression of structural and vascularized stroma components. The stroma activated subtype was defined by its high expression of *ACTA2*, *SPARC* (secreted protein acidic and cysteine rich), and *FAP* (fibroblast activation protein alpha). Lastly, the pure basal-like subtype displayed a low stromal signal [28]. Additionally, Dijk et al. grouped 90 PDAC tissue samples into four subtypes based again on transcriptome data and according to their biological characteristics: **secretory**, **epithelial**, **compound pancreatic**, and **mesenchymal** [29]. The secretory subtype featured both endocrine and exocrine functions, the epithelial subtype was identified by MYC signaling, the mesenchymal subtype was rich in genes associated with EMT and TGF-β signaling, and the compound pancreatic subtype combined features of the mesenchymal and endocrine subtypes [29]. Another study by Chan-Seng-Yue et al. included advanced PDAC tissue samples for the first time [30]. They performed laser capture microdissection (LCM) to enrich tumor cells. Subsequently, bulk RNA-seq was performed and tumor samples were categorized into five subtypes based on gene expression: **basal-like A**, **basal-like B**, **classical A**, **classical B**, and **hybrid**. Among them, the basal-like A subtype showed high expression of squamous differentiation-related genes, such as *KRT5* (keratin 5), *KRT6A* (keratin 6A), *KRT6B* (keratin 6B), and *KRT14* (keratin 14). The basal-like B subtype showed the expression of callogenesis-related genes, such as *FOXJ1* (forkhead box J1), *CST6* (cystatin E/M), *DRC1* (dynein regulatory complex subunit 1), *CFAP54* (cilia and flagella associated protein 54), and *ZBBX* (zinc finger B-box domain containing). The classical A and classical B subtype were two distinct transcriptional signatures within the previous ‘classical’ signature defined by Moffitt et al.; the hybrids subtype had no significantly associated genes with the classical or basal-like subtype. Interestingly, their scRNA-seq data generated from freshly resected tumor tissue samples and from biopsies of advanced tumor samples revealed an intratumoral coexistence of basal-like and classical tumor signatures [30]. In order to address a classification bias caused by the complex composition of PDAC tissues, Hayashi et al. utilized multi-site sampling within tumor tissues for RNA-seq analysis and compared the findings with histological staining [31]. The results suggested that histologically squamous regions correlated with the basal-like subtype identified through transcriptomic analysis [31]. To better understand

tumor cell heterogeneity of PDAC, Juiz et al. performed scRNA-seq analysis on 20 patient-derived organoids (PDOs). Although they selected six PDOs with the most pronounced classical and the least basal-like features for their transcriptome analysis, their analysis revealed substantial heterogeneity within purely classical PDOs, which contained a high proportion of basal-like cells [32].

Molecular subtypes of PDAC have a major impact on patient prognosis. Patients with the classical subtype generally experience better post-surgery outcomes than those with the QM-PDA subtype as shown by Collisson et al. [25]. Similarly, the study by Moffitt et al. confirmed that the basal-like subtype is associated with poorer prognoses [26]. Additionally, the data from Puleo et al. demonstrated that patients with well-differentiated tumors of the pure classical subtype had a median survival of 43 months and a favorable prognosis. In contrast, patients with a poorly differentiated, pure basal-like subtype had a median survival of only 10 months [28]. The study by Dijk et al. revealed similar results showing that the secretory tumor subtype had a more favorable prognosis compared to the mesenchymal subtype [29].

Several studies have used transcriptomic data to categorize previously established human PDAC cell lines based on the aforementioned molecular subtype classification. For instance, in the study conducted by Dijk et. al., the PDAC cell lines Hs 766T, T3M-4, PANC-1, and PSN-1 were categorized as mesenchymal, while HPAF-II, BxPC-3, AsPC-1, Capan-2, and Capan-1 were classified as non-mesenchymal [29]. The mesenchymal subtype is highly associated with the expression of the mesenchymal marker gene *VIM* (vimentin) and the invasive growth marker gene *CXCR4* (C-X-C motif chemokine receptor 4). In contrast, non-mesenchymal or classical cell lines exhibited a high gene expression of *CDH1* (cadherin 1), *EPCAM* (epithelial cell adhesion molecule) and *ERBB3* (erb-b2 receptor tyrosine kinase 3) [29]. In addition, Diaferia et al. conducted RNA-seq analysis on nine established human PDAC cell lines and classified them into two categories. CFPAC-1, Capan-2, HPAF-II and Capan-1 were classified as low-grade PDAC cell lines that exhibit the classical PDAC signature. BxPC-3, AsPC-1, PANC-1, MiaPaCa-2 and PT45-P1 were classified as high-grade PDAC cell lines which showed mesenchymal morphology and expressed mesenchymal genes [33].

Overall, these studies indicate that PDAC tumor cells can be primarily classified into classical and basal-like subtypes. The classical subtype displays an epithelial phenotype, whereas the basal-like subtype shows a mesenchymal phenotype and is closely linked to an EMT program. In recent years, the methodical analysis for studying molecular subtypes of PDAC has been continuously broadened, including nowadays also scRNA-seq, to precisely identify tumor cells and differentiate them from the tumor microenvironment for correct classification of molecular tumor cell subtypes. In addition,

established PDAC cell lines as simplified models have been categorized into classical and basal-like subtypes. This model aids in our comprehension of the distinctions and transition between classical and basal-like PDAC, as well as their response to chemotherapeutic drugs.

1.3 Histone acetylation in pancreatic ductal adenocarcinoma

1.3.1 Histone acetylation

In eukaryotic organisms, chromatin is organized in nucleosomes, each consisting of 146 bp of DNA wrapped 1.6 times around an octamer of core histones (H2A, H2B, H3, H4). There are two main kinds of chromatin found in the nucleus. Heterochromatin is a dense form of chromatin characterized by the wrapping around histones and a closed chromatin structure. This compact structure conserves storage space and prevents the binding of transcription complexes to DNA, therefore functioning as a repression system for gene expression. Euchromatin, in contrast, exhibits a loose structure and is commonly seen in regions associated with active gene transcription. Histone post-translational modification (PTMs) mainly appear on the N-terminal tails of core histones and influence higher-order chromatin structure. Histone PTMs are regulated by two types of histone-modifying enzymes: "writers," which add modifications, and "erasers," which remove the modifications. Another group of proteins, which are called "readers" recognize histone modification [34]. Eight types of histone PTMs have been identified: methylation, acetylation, phosphorylation, ubiquitylation, SUMOylating, ADP ribosylation, deamination, and proline isomerization [35].

Histone acetylation is the most extensively studied histone PTM and is a key modification of transcriptional activation that occurs predominantly at enhancers, promoters, and 5' coding regions of genes [36]. Histone acetylation primarily counterbalance the positive charges on lysine residues, influencing the interactions between nucleosomes and DNA binding. It facilitates the conversion of heterochromatin to euchromatin and opens the DNA for transcription factor binding [37]. For example, H3K9ac and H3K14ac play a crucial role in attracting the transcription factor TFIID (Transcription factor II D) to the promoter of *IFNB1* (interferon beta 1) gene in HeLa cells [38]. In addition to directly impacting chromatin structure, histone acetylation can also influence transcription by recruiting proteins, that contain bromodomains (BRDs), which are “readers” and directly bind to histone acetylation modifications [39].

H3K27ac is widely recognized as a marker of active enhancers and promoters. Several studies have investigated the acetylation of lysine 27 on histone H3 across the entire

genome in PDAC and its effect on gene expression, thereby influencing tumor development and progression. One study conducted a comprehensive genome-wide assessment of H3K27ac profiles in PDAC cell lines, S2-007 and MiaPaCa-2, revealing significantly increased acetylation at enhancer regions of oncogenes such as *SOX2* (SRY-box transcription factor 2), *FOXO1* (forkhead box O1), and *CDX2* (caudal type homeobox 2), which was associated with elevated transcription levels [40]. Furthermore, the study of Diaferia et al. classified nine previously established PDAC cell lines into low-grade and high-grade tumor cell lines, which correspond to classical and basal-like subtypes, respectively, based on transcriptome data [33]. The parallel analysis of H3K27ac profiles in these cell lines revealed that low-grade and high-grade PDAC cell lines clustered separately. In low-grade cell lines, H3K27ac was found at the enhancer regions of genes with epithelial identity, such as *KLF5* (KLF transcription factor 5) and *PBX1* (PBX homeobox 1). In contrast, the high-grade PDAC cell lines revealed a loss of their epithelial characteristics, which was linked to a reduction of H3K27ac at enhancers of epithelial genes [33]. McDonald et al. performed immunoblot analysis on PDAC cells collected from peritoneal subclones and from liver and lung metastatic subclones from the same patient. The result showed increased acetylation at the H3K27 site in distant metastatic subclones compared to peritoneal [41]. The acetylation status of histone lysine residues is tightly controlled by the balance of two counteracting enzymes, which are histone acetyltransferases (HATs) as histone acetylation “writers” and histone deacetylases (HDACs) as histone acetylation “erasers”. Therefore, an imbalance between HATs and HDACs can lead to abnormal gene expression, contributing to tumor development and progression.

1.3.2 Histone acetyltransferases

Based on cellular localization, HATs are categorized into type A, mainly localized in the nucleus, and type B, found in the cytoplasm. Type A HATs have two conserved domains: a BRD that binds at histone acetylation sites, and a catalytic domain that facilitates the transfer of acetyl groups. In contrast, type B HATs lack BRDs and modify newly synthesized histones in the cytoplasm [42]. In addition, HATs can be classified into three families: the p300/CREB-binding protein (p300/CBP), the MYST family (Moz, Ybf2, Sas2, Tip60), and the GCN5-related N-acetyltransferase (GNAT) family, based on sequences homologies to yeast [43]. The HATs of the p300/CBP family function as transcriptional co-activators and are closely associated with tumorigenesis. The enzymes prefer the acetylation of lysine residues K18/27 on histone H3 (H3K18ac or H3K27ac) located at enhancer and promoter regions [44]. However, reports on the role of p300/CBP family members in tumors are context and tumor type dependent. Some studies suggest that

the HAT *CREBBP* (CREB binding protein) acts as a tumor suppressor, due to its absence in around 10-15% of small cell and non-small cell lung cancer cells [45]. Moreover, inactivating mutations of the HAT *EP300* (E1A binding protein p300) were identified to promote tumor development of bladder cancer [46, 47]. In contrast, other research studies indicate that p300/CBP can induce tumor progression. In hepatocellular carcinoma (HCC), high expression of *EP300* is associated with elevated levels of the clinical biomarker serum alpha-fetoprotein (AFP) and a poor prognosis for HCC patients [48]. In addition, a strong correlation between *EP300* expression and the prostate cancer biomarker androgen receptor (AR) expression was identified, noting that high expression of *EP300* is associated with resistance to androgen deprivation therapy (ADT) [49].

The role of HATs in PDAC is not clearly defined. A study indicated elevated expression of *EP300* in most human PDAC tissues [50], while PDAC cell lines with a high propensity for metastasis showed reduced expression of *EP300* [51]. Another study demonstrated that the loss of p300 resulted in decreased expression of *GATA6*, impairing cell differentiation and leading to a transition from a classical to a basal-like/squamous subtype in PDAC [52]. Additionally, treatment of PDAC cell line PANC-1 with histone acetyltransferases inhibitor (HATi) significantly reduced the H3K27ac enrichment on genes associated with adherents junctions [53]. Although HATs have the potential to be a target for tumor therapy, the progress in developing HATi is significantly behind that of histone deacetylase inhibitors (HDACi). The U.S. Food and Drug Administration (FDA) has approved five HDACi, but no HATi [54]. Due to the fact that the complex members p300 and CBP exhibit significant sequence similarities in their BRD and catalytic domain, it is necessary to target both domains in the proteins. Some HATi are available, such as the BRD inhibitors CCS1477 (inobrodib) and ICG-001, as well as catalytic inhibitors such as A485, DS-9300, and CPI-1612. However, only HATi ICG-001 has been tested in advanced PDAC as a phase 1 clinical trial (NCT01764477) as second-line therapy following FOLFIRINOX or FOLFOX chemotherapy, but it has shown limited efficacy [55].

1.3.3 Histone deacetylases

So far, 18 human HDACs have been identified, which are divided into four classes (I-IV). Class I is homologous to yeast Rpd3 and includes HDAC 1, 2, 3, and 8. Class II is homologous to yeast Hda1 and is divided into type IIa and type IIb HDACs, which contains HDAC (4, 5, 7 and 9) and HDAC10, respectively. Class III is homologous to yeast Sir2 and consists of SIRT 1, 2, 3, 4, 5, 6 and 7. Lastly, class IV consists of HDAC11, which shares structural similarities with class I and II, but its function remains unclear [56]. Class I, II, and IV HDACs utilize zinc as a cofactor for enzymatic activity [57], whereas class III HDACs depend on NAD+ for their activity [58]. Class I and IV HDACs

are located only in the cell nucleus, while class IIb HDACs are in the cytoplasm. Class IIa HDACs possess a nuclear export signal (NES) and a nuclear import signal (NLS) and shuttle between the nucleus and cytoplasm. Class III HDACs are located in the nucleus and cytoplasm [59]. HDACs are commonly overexpressed in various tumor tissues [60]. The nuclear histone deacetylases HDAC1 and HDAC2 are crucial in regulating cell proliferation and the cell cycle [61, 62]. They also influence stem cell development and differentiation [63], and therefore participating in tumor development [64, 65]. Additionally, they promote an EMT phenotype of tumor cells and thereby accelerating tumor invasion and metastasis formation [66-68]. While HDAC1 and HDAC2 have the ability to function independently as free histone deacetylases, they can also serve as core components of large transcriptional repression complexes that regulate histone acetylation during tumorigenesis [69-72].

HDAC1/2 are regarded as oncogenes in PDAC. For example, the study of Lehmann et al. found elevated *HDAC2* expression in undifferentiated PDAC samples [73]. Also, other studies identified HDAC2 as a crucial factor for maintaining gene expression that is associated with undifferentiated PDAC and for activating the expression of TGF-β pathway genes [66]. Different approaches have investigated the consequences of HDAC2 depletion in human PDAC cell lines and in PDAC mouse models. Thus, a genetic deletion of Hdac2 in a pancreatic cancer mouse model not only inhibits basal-like tumor cell clone formation, but also reduces the tumor metastasis rate by 50% [66]. Moreover, loss of HDAC2 expression resulted in an enhanced sensitivity to the chemotherapy drug etoposide in PDAC cell lines MIAPaCa2 and PANC-1 [74]. Similarly, a reduction of *HDAC2* expression in MIAPaCa2 cells increased sensitivity to tumor necrosis factor-related apoptosis-inducing ligand (TRAIL), activating tumor cell apoptosis [75]. Currently, more than 40 varieties of HDAC inhibitors have been developed and entered clinical trials [76]. Five of them including Vorinostat (SAHA), Belinostat (Beleodaq/PXD101), Panobinostat (LBH-589), Romidepsin (Depsipeptide/FK228) have been approved by the FDA [54]. However, clinical trials for HDACi, such as Entinostat (NCT00020579), Vorinostat (NCT00948688), Romidepsin (NCT00379639, NCT04257448), 4-phenylbutyrate (4-PB) and Valproic acid (VPA) for patients with PDAC are still in phase I/II [77]. More research on the role of HDACs and their mechanism in PDAC is needed to elucidate its potential as a therapeutic target and to optimize HDAC treatment strategies for PDAC.

1.4 Epithelial to mesenchymal transition in pancreatic ductal adenocarcinoma

PDAC is characterized by high invasiveness and early metastases, resulting in severe tumor aggressiveness and devastating overall survival rates for PDAC patients. PDAC consists of up to 80-85% stroma and the unique tumor microenvironment is believed to drive tumor invasiveness and early metastasis formation. The extensive extracellular matrix (ECM) in the tumor stroma functions in early carcinogenesis as a barrier that limits intake of oxygen and nutrients by PDAC cells, compelling cancer cells to undergo EMT to find more suitable growth conditions [78].

The EMT program is not a unique characteristic of tumor cells. Type I EMT is known as a key program in embryonic morphogenesis, and type II EMT participates in the inflammatory response to assist in wound healing and tissue regeneration [79]. Tumor cells hijack the normal EMT program, initiating the transformation from tightly packed epithelial structures to loosely organized, spindle-shaped mesenchymal forms and acquire mesenchymal characteristics, a process regarded as type III EMT [80]. After tumor cells evade and metastasize, they may revert to their epithelial phenotypes via the mesenchymal-to-epithelial transition (MET) program, thereby supporting the continued growth of metastatic tumors [81].

The mechanism behind type III EMT remains uncertain. Existing evidence indicates that the cause of this complex procedure may be attributed to gene mutations, epigenetic modifications, aberrant intracellular signal transduction, or responses to abnormal extracellular signals [82-84]. During this process, transcription factors (TFs) related to EMT (EMT-TFs) are activated in response to signaling pathways, leading to the downregulation of epithelial marker genes, including *CDH1* (which encodes the protein E-cadherin) and *EPCAM*, and the upregulation of mesenchymal marker genes, such as *VIM* and *CDH2* (which encodes the protein N-cadherin) [85-87]. Ultimately, the cytoskeleton is rearranged, resulting in epithelial cells acquiring a mesenchymal character [88].

EMT-TFs and EMT-related signaling pathways are two key players in the tumor-related EMT process. Specifically, several EMT-TFs have been identified, including the Zinc finger E-box binding homeobox (ZEB) family's ZEB1 and ZEB2, the Zinc finger protein family's SNAI1 (known as SNAIL) and SNAI2 (known as SLUG), and the basic helix-loop-helix transcription factor family's TWIST1 and TWIST2 [89, 90]. Additionally, several signaling pathways play a role in regulating the expression of EMT-TFs, such as SMAD-dependent canonical TGF-β signaling and SMAD-independent non-canonical TGF-β signaling, WNT signaling, JAK/STAT signaling and Notch signaling [88, 91-94].

An activation of these pathways during cancer development results in an EMT phenotype of the tumor cells promoting tumor progression and aggressiveness.

1.5 Rho-GTPase family in pancreatic ductal adenocarcinoma

Small guanine triphosphatases (GTPases) and their downstream signals are crucial in regulating actin cytoskeleton dynamics and play significant roles in EMT in tumor progression. Rho-GTPases are key regulators of the filamentous actin (F-actin) cytoskeleton system, and are involved in microtubule organization, cell-cell adhesion, and epithelial morphogenesis [95-98]. Different members of the Rho-GTPase family influence the subcellular localization of actin filaments, orchestrating the formation of actin filament subcompartments, such as lamellipodia, filopodia, and stress fibers. Lamellipodia and filopodia consist of branched actin filaments, whereas stress fibers are composed of linear actin filaments [99].

1.5.1 Subgroups and regulators of Rho-GTPase

The mammalian Rho-GTPase family consists of 20 members, categorized into seven subgroups based on similarities in amino acid sequence. Rac, Cdc42, and Rho subgroups are considered typical Rho-GTPases with a GDP-/GTP-binding domain, whereas the Rnd, RhoD, RhoH and RhoBTB subgroups are classified as atypical Rho-GTPases [100] (Figure 1.1).

Typical Rho-GTPases:

- Rho subgroup (RhoA, RhoB, and RhoC)
- Rac subgroup (Rac1, Rac2, Rac3, and RhoG)
- Cdc42 subgroup (Cdc42, RhoQ, RhoJ, RhoV, RhoU)

Atypical Rho-GTPases:

- Rnd subgroup (Rnd1, Rnd2, Rnd3)
- RhoD subgroup (RhoD and RhoF)
- RhoH
- RhoBTB subgroup (RhoBTB1, RhoBTB2)

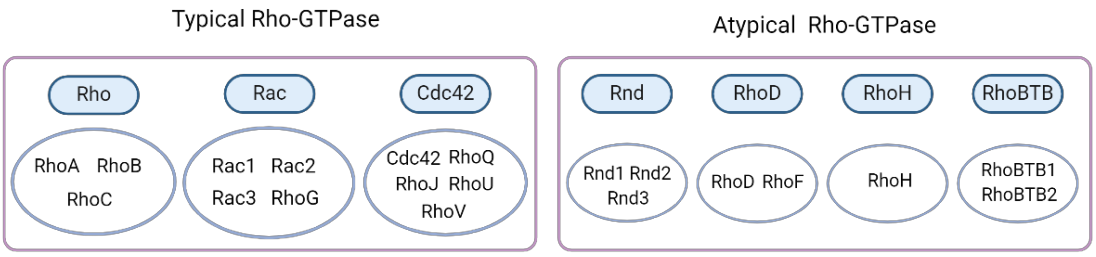

Figure 1.1: Overview of the mammalian Rho-GTPase family. The Rho-GTPase family comprises 20 members, categorized into seven subgroups. These subgroups are divided into typical and atypical GTPases based on the presence of a GDP-/GTP-binding domain.

Typical Rho-GTPases switch between an active GTP- and inactive GDP-bound form, which are named Rho-GTP and Rho-GDP, respectively. This switch is regulated by three major classes of proteins: guanine-nucleotide exchange factors (GEFs), which facilitate GDP replacement by GTP to activate Rho-GTPases [101]; GTPase-activating proteins (GAPs), which enhance intrinsic GTPase activity and hydrolyze GTP to GDP to inactivate Rho-GTPases [102]; and guanine-nucleotide dissociation inhibitors (GDIs) that bind Rho-GTPase in its inactive Rho-GDP form to prevent GEF-mediated activation of Rho (Figure 1.2) [103].

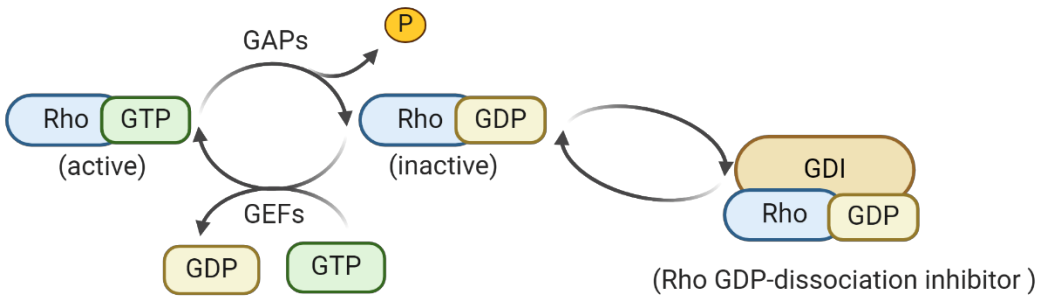

Figure 1.2: Schematic diagram of the Rho-GTPase cycle. Rho-GTPase alternates between active Rho-GTP and inactive Rho-GDP forms, catalyzed by three protein classes. GEFs (guanine-nucleotide exchange factors) activate Rho-GTPase by replacing GDP with GTP. GAPs (GTPase-activating proteins) accelerate GTP hydrolysis, converting it back to the inactive Rho-GDP form. GDIs (guanine-nucleotide dissociation inhibitors) inhibit the activation of Rho-GDPs through binding whereby they block GEF-mediated activation and preserve the inactive state.

1.5.2 Typical Rho-GTPases

RhoA promotes the formation of linear filaments through two effectors Rho kinase (ROCK) and mammalian Diaphanous-related formin (mDia). ROCK1 and ROCK2, which have a 65% sequence homology, act as the main downstream effectors of RhoA. The ROCK structure comprises multiple different domains, including an N-terminal kinase domain, a coiled-coil domain in the center, and a C-terminal region that contains both the Rho-binding domain (RBD) and a Pleckstrin homology (PH) domain [104-106]. The kinase activity of ROCK is inhibited by the PH domain. When RhoA-GTP binds to the RBD of ROCK, this interaction relieves the auto-inhibition imposed by the PH domain, thereby activating the kinase ROCK [106-108]. Alternatively, ROCK activation can occur through C-terminal cleavage. Specifically, ROCK1 is cleaved by Caspase-3, and ROCK2 by Granzyme B, which allows for activation independent of RhoA (Figure 1.3) [109, 110].

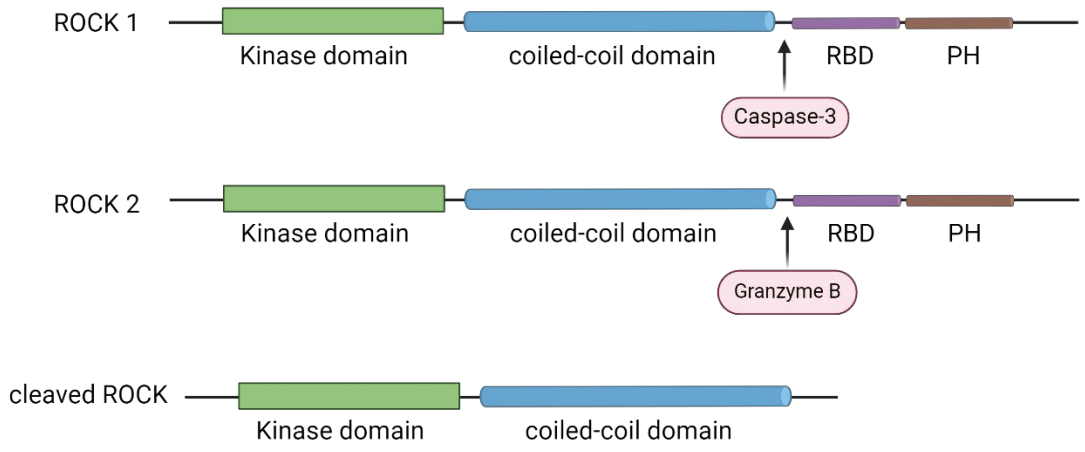

Figure 1.3: Structure of the RhoA effector ROCK. ROCK consists of an N-terminal kinase domain, a central coiled-coil domain, and a C-terminal region comprising an RBD (Rho-binding domain) domain that interacts with activated RhoA-GTPase, and a PH (Pleckstrin homology) domain that auto-inhibits kinase activity. Cleaved ROCK retains the N-terminal kinase domain and the central coiled-coil domain. Specifically, ROCK1 is cleaved by Caspase-3, and ROCK2 is cleaved by Granzyme B.

Activated ROCK enhances the formation and stability of linear stress fibers by inhibiting the actin depolymerizing factor, Cofilin. Another important effector of RhoA is mDia, which assembles actin and accelerates the extension of actin filaments. In contrast, Rac and Cdc42 primarily drive the formation of branched actin filaments. Insulin receptor tyrosine kinase substrate p53 (IRSp53) is an effector of Rac and Cdc42 that can activate the actin-related protein 2/3 (Arp2/3) complex, promoting actin branching formation [111, 112]. The WASP-family verprolin-homologous protein (WAVE) functions as a Rac effector. It is directly regulated by Rac and also acts downstream of IRSp53 to enhance the activity of the Arp2/3 complex, leading to the formation of lamellipodia [111, 113].

Wiskott-Aldrich syndrome protein (WASP) and myotonic dystrophy kinase-related Cdc42-binding kinase (MRCK) are specialized effectors of Cdc42. WASP acts through the Arp2/3 complex, while MRCK phosphorylates membrane-organizing extension spike protein (Moesin) to facilitate the formation of filopodia [114, 115]. In addition to enhancing branched filament formation, Rac and Cdc42 can also enhance linear filament formation by inhibiting Cofilin through the effector P21-activated kinase (PAK) [116] (Figure 1.4).

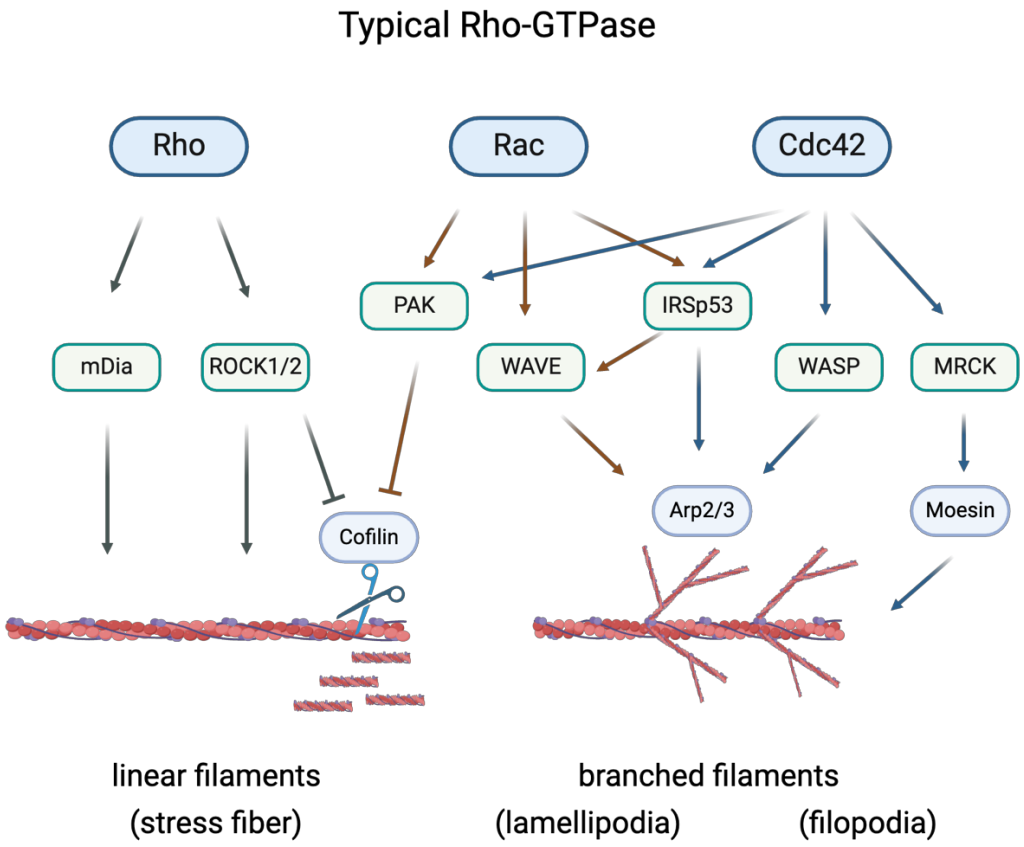

Figure 1.4: Effectors of the typical Rho-GTPase. Typical Rho GTPases (Rho, Rac, and Cdc42) regulate the organization of actin filaments into linear or branched structures. Rho activates mDia and ROCK1/2 to form linear actin filaments (stress fibers) and inhibits Cofilin to stabilize these filaments. Rac activates WAVE and IRSp53 to promote Arp2/3-mediated branched filaments (lamellipodia) and activates PAK to inhibit Cofilin to stabilize linear actin filaments. Cdc42 activates IRSp53 and WASP to promote Arp2/3-mediated branched filaments (filopodia) and phosphorylates MRCK to form filopodia via Moesin.

Typical Rho-GTPases are crucial factors in tumor progression as they participate throughout the entire EMT process. Rho-GTP activation plays a pivotal role in promoting actin-myosin contraction, which leads to the formation of stress fibers and focal adhesions. These structures provide the necessary force and attachment points for cells to change shape and migrate, thus facilitating EMT process [117]. In PDAC cell lines PANC-1 and Panc 02.03, inhibiting RhoA can reduce the formation of stress fibers [118].

In PANC1 cells, a high expression of *EIF5A* (eukaryotic translation initiation factor 5A) activates RhoA/ROCK signaling, which drives metastasis formation [119]. On the other hand, Rac-GTP is essential for maintaining cell-cell adhesion. A deficiency in Rac-GTP reduces cell-cell adhesion at the initial stage of tumor metastatic spreading. This reduction destabilizes cell-cell junctions and makes it easier for the tumor cells to detach from the primary tumor. Hence it was shown that Rac1B maintains cell-cell adhesion by promoting E-cadherin expression and interfering with TGF-β-induced MEK-ERK signaling to preserve epithelial characteristics and prevent EMT to reduce cell migration and invasion [120]. In normal epithelial cells, Cdc42-GTP collaborates with E-cadherin to maintain cell-cell adhesion [121, 122]. However, during EMT, Cdc42-GTP shifts its role to enhance cell invasiveness by promoting the formation of filopodia, which facilitates cell migration [123, 124]. In the PANC-1 cell line, Interleukin-6 (IL-6) activates Cdc42 through the JAK/STAT signaling pathway, enhancing filopodia formation and promoting cell invasion and metastasis [125].

Overall, Rho-GTPases are crucial factors in tumor progression, participating throughout the entire EMT process. Understanding their roles and mechanisms offers potential therapeutic targets for combating PDAC aggressiveness and metastasis formation.

2. Aim of study

Tumor heterogeneity and EMT are significant contributors to poor chemotherapy response. Currently, two major molecular subtypes of PDAC, classical and basal-like, have been identified, which exhibit differences in phenotypic characteristics and chemotherapy response. Better potential therapeutic regimens for advanced PDAC patients are urgently needed, particularly for stratified treatment options based on PDAC subtype classification.

This study aims to identify molecular and epigenetic changes in the transcriptional signatures and beyond in classical and basal-like PDAC cell lines that are associated with EMT marker genes and Rho-GTPase/ROCK signaling. An inhibitor for ROCK and epigenetic drugs for histone acetyltransferases (HAT) and histone deacetylases (HDAC) are investigated to show tumor subtype specific treatment effects. Deregulating the cytoskeleton and EMT features, as well as changing the epigenetic landscape of the tumor cells should reprogram the tumor cells towards a less aggressive phenotype that might be better targetable (Figure 2.1).

To explore the mechanisms underlying the differential transcriptomic signatures of EMT and cytoskeleton in classical and basal-like PDAC cell lines, this study plans to first perform RNA sequencing on seven PDAC cell lines to classify them into classical and basal subtypes, followed by validation of the identified markers through qPCR. To confirm the differential expression and cellular localization of Rho-GTPases and the effector ROCK2 in these cell lines, immunofluorescence, nuclear-cytoplasmic fractionation, and immunoblot are conducted. To further investigate the role of Rho-GTPase/ROCK signaling in regulating cytoskeletal morphology and EMT, specifically whether this pathway is inactive in classical cell lines and active in basal-like cell lines, the study uses the ROCK inhibitor Y-27632 to evaluate its subtype-specific effects on stress fiber formation and to explore the potential link between ROCK signaling and HDAC phosphorylation. Finally, to validate the role of histone acetylation levels and epigenetic regulation in these processes, the study aims to treat classical and basal-like cell lines with HAT and HDAC inhibitors on a long-term basis to assess changes in epigenetic modifications, transcriptomic signatures, and tumor cell phenotypes.

In conclusion, a comprehensive understanding of the molecular mechanisms underlying the phenotypic plasticity of PDAC cells is aimed to be provided by this study, and potential therapeutic strategies targeting Rho-GTPase pathways and histone acetylation for the treatment of different PDAC subtypes are intended to be identified.

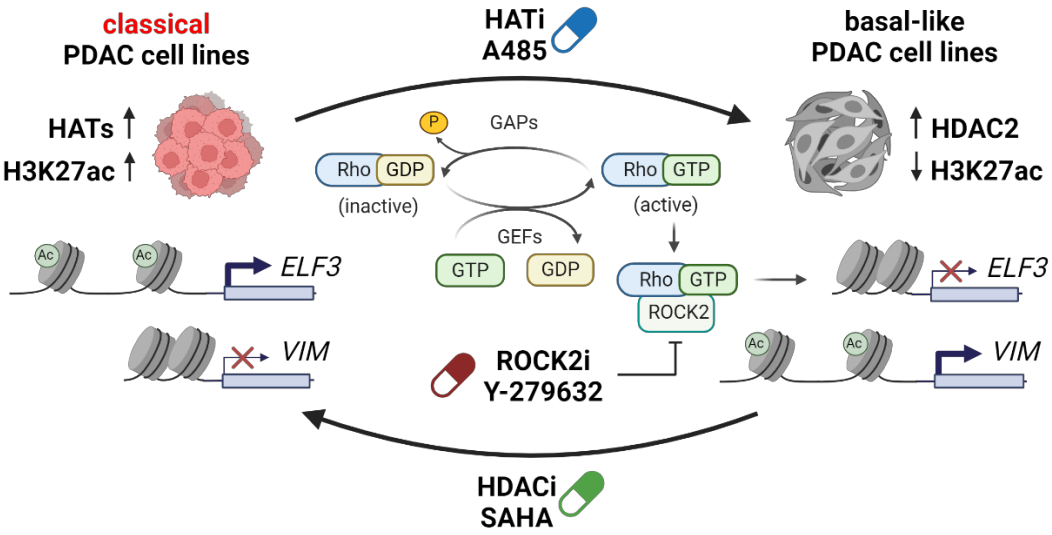

Figure 2.1: Schematic diagram of the study aims.

3. Material and Methods

3.1 Material

3.1.1 Chemicals and reagents

Table 1 Chemicals and reagents

Reagent	Manufacturer
(D)PBS-Trockensubstanz	Bio&SELL GmbH, Nürnberg, Germany
1,4-Piperazinediethanesulfonic acid (PIPES)	Sigma-Aldrich, St. Louis, USA
Paraformaldehyde (PFA), 16%	Electron Microscopy Sciences, Hatfield, Germany
1-bromo-3-chloropropane (BCP)	Sigma-Aldrich, St. Louis, USA
3-(4,5-dimethylthiazol-2-yl) -2,5-diphenyltetrazolium bromide (MTT)	Sigma-Aldrich, St. Louis, USA
Acrylamide, 30%	Carl Roth GmbH, Karlsruhe, Germany
Paraformaldehyde (PFA), 4%	Morphisto GmbH, Offenbach am Main, Germany
TriTrack DNA dye, 6x	Thermo Fisher Scientific, Waltham, USA
Agarose SERVA for DNA Electrophoresis	SERVA, Heidelberg, Germany
Ammonium persulfate (APS)	Sigma-Aldrich, St. Louis, USA
AURION BSA-c™ (10%)	AURION: Lab chemicals
Bovine serum albumin (BSA)	Carl Roth GmbH, Karlsruhe, Germany
Calcium chloride dihydrate (CaCl2 · 2H2O)	Roche, Basel, Switzerland
Crystal violet	Sigma-Aldrich, St. Louis, USA
Dimethyl sulfoxid (DMSO)	Sigma-Aldrich, St. Louis, USA
Donkey serum	Sigma-Aldrich, St. Louis, USA
Dulbecco´s phosphate buffered saline (DPBS)	Sigma-Aldrich, St. Louis, USA
Dulbecco's Modified Eagle Medium - high glucose (DMEM)	Sigma-Aldrich, St. Louis, USA

Ethanol for molecular biology	Sigma-Aldrich, St. Louis, USA
Ethylene glycol bis(β-aminoethylether) tetraacetic acid (EGTA)	Roche, Basel, Switzerland
Ethylenediaminetetraacetic acid disodium salt dihydrate (EDTA)	Sigma-Aldrich, St. Louis, USA
FastStart Essential DNA Green Master	Roche, Basel, Switzerland
Fetal Bovine Serum (FBS)	Sigma-Aldrich, St. Louis, USA
Fluoroshield Mounting Medium With DAPI	Abcam, Cambridge, GB
Formamide	Merck, Darmstadt, Germany
GeneRuler (100 bp)	Thermo Fisher Scientific, Waltham, USA
Glycine	Carl Roth GmbH, Karlsruhe, Germany
Isopropanol	SAV Liquid Production GmbH, Flintsbach, Germany
Kalium chloride (KCl)	Roche, Basel, Switzerland
Lithium chlorid (LiCl)	Roche, Basel, Switzerland
Methanol	Merck, Darmstadt, Germany
Micrococcal Nuclease Solution (MNase)	Thermo Fisher Scientific, Waltham, USA
Milk powder, Blotting-Grade	Carl Roth GmbH, Karlsruhe, Germany
Natrium chlorid (NaCl)	Roche, Basel, Switzerland
Nonident P-40 (NP-40)	Sigma-Aldrich, St. Louis, USA
PageRegular Plus Prestained Protein Ladder (10 to 180 kDa)	Thermo Fisher Scientific, Waltham, USA
Penicillin – Streptomycin (P/S)	Sigma-Aldrich, St. Louis, USA
Pierce™ Phosphatase Inhibitor Tablets	Thermo Fisher Scientific, Waltham, USA
Pierce™ Protease Inhibitor Tablets	Thermo Fisher Scientific, Waltham, USA
Protein A agarose/salmon sperm DNA	Merck Millipore, Billerica, USA
Proteinase K	Thermo Fisher Scientific, Waltham, USA
Ribonuclease A (RNase A)	QIAGEN, Hilden, Germany
Rnase-ExitusPlus	PanReac AppliChem, Darmstadt, Germany

Roswell park memorial institute medium 1640 with L-Glutamine Medium (RPMI)	Capricorn Scientific, Ebsdorfergrund, Germany
Sodium bicarbonate (NaHCO3)	Sigma-Aldrich, St. Louis, USA
Sodium deoxycholate (DOC)	Sigma-Aldrich, St. Louis, USA
Sodium dodecyl sulfate (SDS) Pellets	Carl Roth GmbH, Karlsruhe, Germany
SYBR™ Safe DNA Gel Stain	Thermo Fisher Scientific, Waltham, USA
Tetramethylethylendiamine (TEMED)	Carl Roth GmbH, Karlsruhe, Germany
TRIS base	Carl Roth GmbH, Karlsruhe, Germany
Triton X- 100	Sigma-Aldrich, St. Louis, USA
TRIzol™ Reagent	Life technologies, Carlsbad, California, USA
Trypan Blue solution, 0.4%	Sigma-Aldrich, St. Louis, USA
Tween 20	Merck, Darmstadt, Germany

3.1.2 Kits

Table 2 Kits

Kit	Manufacturer
Clarity Western ECL Substrate	Bio-Rad, Herkules, USA
CytoPainter, Phalloidin- iFluor 488 Reagent	Abcam, Cambridge, GB
NE-PER™ Nuclear and Cytoplasmic Extraction Reagents	Thermo Fisher Scientific, Waltham, USA
Pierce™ BCA Protein Assay Kit	Thermo Fisher Scientific, Waltham, USA
QIAquick PCR purification Kit	QIAGEN, Hilden, Germany
RevertAid First Strand cDNA Synthesis Kit	Thermo Fisher Scientific, Waltham, USA
RNeasy Plus Mini Kit	QIAGEN, Hilden, Germany

3.1.3 Drugs

Table 3 Drugs

Drug	Manufacturer
A485 (HAT inhibitor)	Tocris Bioscience, Bristol, UK
Mitomycin C (DNA synthesis inhibitor)	Carl Roth GmbH, Karlsruhe, Germany
Vorinostat or suberoylanilide hydroxamic acid (SAHA) (HDAC ihibitor)	Sigma-Aldrich, St. Louis, USA
Y-27632 dihydrochloride (ROCK inhibitor)	Tocris Bioscience, Bristol, UK

3.1.4 Antibodies

3.1.4.1 Primary antibodies

Table 4 Primary antibodies, IF: Immunofluorescence, WB: Western blot, ChIP: Chromatin immunoprecipitation

Primary antibody	Host	Application	Manufacturer/ Ref
EpCAM	Mouse	(IF) 1:200 in 5% donkey serum, 1% BSA, 0.1% Triton-X/PBS	Cell Signaling Technology, Danvers, USA/ #2929
Vimentin	Rabbit	(IF) 1:200 in 5% donkey serum, 1% BSA, 0.1% Triton-X/PBS	Cell Signaling Technology, Danvers, USA/ #5741
ROCK2	Mouse	(IF) 1:50 in 5% donkey serum, 1% BSA, 0.1% Triton-X/PBS; (WB) 1:100 in 5% Milk/TBS-T	Santa Cruz, Dallas, USA/ sc-398519
RHOA	Mouse	(IF) 1:50 in 5% donkey serum, 1% BSA, 0.1% Triton-X/PBS; (WB) 1:200 in 5% BSA/TBS-T	Santa Cruz, Dallas, USA/ sc-418
Phospho-HDAC2 (Ser394)	Rabbit	(WB) 1:1000 in 5% BSA/TBS-T	Cell Signaling Technology, Danvers, USA/ #69238
HDAC2	Mouse	(WB) 1:1000 in 5% Milk/TBS-T	Cell Signaling Technology, Danvers, USA/ #5113

H3K27ac	Rabbit	(WB) 1:1000 in 5% Milk/TBS-T; (ChIP) 0.3µg	Cell Signaling Technology, Danvers, USA/ #8173
Histone 3	Rabbit	(WB) 1:1000 in 5% Milk/TBS-T	Cell Signaling Technology, Danvers, USA/ #4499
GAPDH	Mouse	(WB) 1:5000 in 5% Milk/TBS-T	Meridian Bioscience Inc., Cincinnati, USA/ H86504M
β-actin	Rabbit	(WB) 1:1000 in 5% BSA/TBS-T	Cell Signaling Technology, Danvers, USA/ #4968
Normal Rabbit IgG	Rabbit	(ChIP) 1µg	Cell Signaling Technology, Danvers, USA/ #2729

3.1.4.2 Secondary antibodies

Table 5 Secondary antibodies, IF: Immunofluorescence, WB: Western blot

Secondary antibody	Host	Application	Manufacturer/ Ref
Anti-Mouse IgG (H+L) (Cyanine Cy™3)	Donkey	(IF) 1:500 in 5% donkey serum, 1%BSA, 0.1% Triton-X/PBS	Jackson ImmunoResearch, Baltimore, USA/715-165-150
Anti-Rabbit IgG (H+L) Fluorescein (FITC)	Donkey	(IF) 1:500 in 5% donkey serum, 1%BSA, 0.1% Triton-X/PBS	Jackson ImmunoResearch, Baltimore, USA/711-095-152
Anti-rabbit IgG Horseradish peroxidase	Donkey	(WB) 1:2000 in 5% Milk/TBS-T	GE Healthcare, Little Chalfont, UK/ NA934V
Anti-mouse IgG Horseradish peroxidase	Donkey	(WB) 1:5000 in 5% Milk/TBS-T	GE Healthcare, Little Chalfont, UK/ NA931V

3.1.5 Primer

3.1.5.1 Gene expression primer (for qRT-PCR)

Table 6 Gene expression primer

Gene	Forward Primer (5‘-3‘)	Reverse Primer (5‘-3‘)
TBP	ACTCCACTGTATCCCTCCCC	CAGCAAACCGCTTGGGATTA
ELF3	GACCTACGAGAAGCTGAGCC	TCGAGTGGTCCGTGAGTTTG
VIM	GGCGAGGAGAGCAGGATTTC	TGGGTATCAACCAGAGGGAGT
EP300	TGGCAGAAAGTTGGAGTTCTCTC	AAGAAACGCTCTCCCCTTGG
CREBBP	GTACCATTCCTCGCGATGCT	ATCAACGAAAGGTTCGGGGT
ARHGAP18	TCAGGCTGTCCAGAATCTTCC	GGGCCATGACCATTGCTACA

3.1.5.2 ChIP primer (for qRT-PCR)

Table 7 ChIP primer

Gene	Forward Primer (5‘-3‘)	Reverse Primer (5‘-3‘)
ELF3	CCCTTCCTCTAACAGCCGTG	AGCTCAGGATACCCACGCTA
VIM	CCCCAAGGTCAATTGCACGA	CACAGTACAGGGTTCACGGT
ARHGAP18	GTCTGACAGCCCATATAGCCC	AGTAGCAACGTTTGGCGTGA

3.1.6 Cell lines

Table 8 Cell lines

Cell line	Resource Identification Initiative (RRID)	Characteristics
PaTu-S	CVCL_1846	Human PDAC cell line
PaTu-T	CVCL_1847	Human PDAC cell line
MiaPaCa-2	CVCL_0428	Human PDAC cell line
PANC-1	CVCL_0480	Human PDAC cell line
Colo357	CVCL_0221	Human PDAC cell line
Capan-1	CVCL_0237	Human PDAC cell line
Capan-2	CVCL_0026	Human PDAC cell line

3.1.7 Consumables

Table 9 Consumables

Material	Manufacturer
96-well plate (qRT-PCR)	STARLAB, Hamburg, Germany
Bacillol surface rapid disinfection	Hartmann, Heidenheim, Germany
Cell counting slides	Bio-Rad, Hercules, USA
Cell culture flasks (25 cm, 75 cm)	Sarstedt, Nürnbrecht, Germany
Cell culture plates (6-well, 12-well, 24-well, 96-well)	Greiner Bio-One, Kremsmünster, Austria
Cell culture plates, TC dish (10 cm)	Sarstedt, Nürnbrecht, Germany
Cell Scraper	Sarstedt, Nürnbrecht, Germany
Chamber slide (8-well)	ibidi GmbH, Gräfelfing, Deutschland
Cover slips (24 X 60 mm)	Epredia, Michigan, USA
Cryogenic tube	STARLAB, Hamburg, Germany
Cytiva Amersham™ Protran™ NC Nitrocellulose Membranes (0.45 µm)	Cytiva Amersham™, Marlborough, Massachusetts, USA
Eppendorf Tubes (1.5 ml, 2 ml)	Sarstedt, Nürnbrecht, Germany
Falcon tubes (15 ml, 50 ml)	Sarstedt, Nürnbrecht, Germany
PCR reaction tube	Biozym, Oldendorf, Germany
Pipette filter tips (10 µl, 200 µl, 1000 µl)	Sarstedt, Nürnbrecht, Germany
Pipette tips (10 µl, 200 µl, 1000 µl)	Sarstedt, Nürnbrecht, Germany
Weighting paper	Roche, Basel, Switzerland
Whatman filter paper	Cytiva Amersham™, Marlborough, Massachusetts, USA

3.1.8 Equipment

Table 10 Equipment

Equipment	Manufacturer
AEJ200-4CM (220 grams/ 0.1 milligrams)	Kern & Sohn, Stuttgart, Germany
Bio-Rad 1000/500 Constant Voltage Power Supply	Bio-Rad, Hercules, USA
Branson 450 Digital Sonifier	Marshall Scientific, Hampton, USA
Centrifuge 5417R	Eppendorf, Hamburg, Germany
Centrifuge 5418R	Eppendorf, Hamburg, Germany
Centrifuge 5702R	Eppendorf, Hamburg, Germany
Corning™ Axygen™ Mini Plate Spinner Centrifuge	Corning, New York, USA
Eppendorf Mastercycler® PCR cycle	Eppendorf, Hamburg, Germany
EW4200-2NM (4200 grams/ 0.01 grams)	Kern & Sohn, Stuttgart, Germany
FLUOstar Omega	BMG LABTECH, Ortenberg, Germany
Fusion FX	Vilber Lourmat GmbH, Eberhardzell, Germany
Heracell 240 CO2 Incubator	Marshall Scientific, Hampton, USA
Heraeus HS18/2, biological safety cabinet	Heraeus instruments, Germany
IKA magnetic stirrer with heating, RET basic	IKA-Werke, Staufen im Breisgau, Germany
inoLab pH 720	WTW, Weilheim, Germany
IX50 Phase contrast inverted microscope	Olympus, Shinjuku, Japan
Zeiss Axio Imager M2	Carl Zeiss Microscopy GmbH, Jena, Germany
LightCycler® 96	Roche, Basel, Switzerland
Medingen W22 water bath	Medingen, Preiss-Daimler, Germany
Mini PROTEAN® Tetra Cell	Bio-Rad, Herkules, USA
Mini Trans-Blot® Module	Bio-Rad, Herkules, USA
Mini-Sub Cell GT Cell	Bio-Rad, Hercules, USA
neoLab® Vortex Genie 2, 2700 UpM	NeoLab, Heidelberg, Germany
Pipetboy acu 2	Integra, Biebertal, Germany

PIPETTE (10µL, 100µL, 200µL, 1mL)	Eppendorf, Hamburg, Germany
PowerPac™ HC Power Supply	Bio-Rad, Hercules, USA
SpectraMax® Plus 384 Microplate Reader	Molecular Devices, San José, USA
TC20 Automated cell counter	Bio-Rad, Hercules, USA
Trans-Blot Turbo Transfer System	Bio-Rad, Hercules, USA
TS1 ThermoShaker	Biometra GmbH, Göttingen, Germany
Freezing Container Mr. Frosty	Nalgene Thermo Scientific, Rochester, New York, USA

3.1.9 Software

Table 11 Software

Software	Manufacturer
FusionCaptAdvance (7.17.02a)	Vilber Lourmat GmbH, Eberhardzell, Germany
GraphPad Prism (10.2.1 (339))	GraphPad Software, Inc., La Jolla, USA
ImageJ (1.53e)	Wayne Rasband, NIH, Bethesda, USA
Leica MM AF (Version 1.6.0)	Leica Microsystems, Wetzlar, Germany
Lightcycler®96 software	Roche, Basel, Switzerland
Primer-BLAST (using Primer3 and BLAST)	National Library of Medicin, Bethesda, USA
Rstudio (Version 2023.06.1+524)	POSIT Community, Boston, USA
Softmax Pro 7.0	Molecular Devices, San José, USA
The R Project for Statistical Computing (Version 4.3.1)	R Development Core Team, USA
UCSC Genome Browser Home	The University of California, California, USA
Biorender	Science Suite Inc., Toronto, Canada

3.1.10 Bioconda and R Packages

Table 12 Bioconda and R Packages

Packages	Research Resource Identifiers (RRID)
Trim Galore (version 0.6.5)	SCR_011847
SortMeRNA (version 4.3.6)	SCR_014402
STAR (version 2.7.3a)	SCR_004463
Samtools (version 1.17)	SCR_002105
HTSeq-count (version 2.0.2)	SCR_00447
DESeq2 (version 1.40.2)	SCR_015687
ggplot2 (version 3.5.0)	SCR_014601
clusterProfiler (version 4.8.2)	SCR_016884
complexHeatmap (version 2.16.0)	SCR_017270

3.2 Methods

3.2.1 Cell biological methods

3.2.1.1 Cell culture

Table 13 Composition culture media

Cell line	Composition culture media
PaTu-S	1X DMEM high glucose media (with L-glutamine) 1% Penicillin/Streptomycin (P/S) (v/v) 10% Fetal Bovine Serum (FBS) (v/v)
PaTu-T	
MiaPaCa-2	
PANC-1	
Colo357	
Capan-1	1X RPMI Medium 1640 (with L-glutamine) 1% Penicillin/Streptomycin (P/S) (v/v) 20% Fetal Bovine Serum (FBS) (v/v)
Capan-2	

Cell culture procedures were conducted in biological safety cabinets. Cell lines were mycoplasma-negative as tested by PCR prior to experiments. Cells were provided with fresh medium every three days; media components for each cell type are listed in Table 13. Cells were washed with 1X PBS before adding fresh culture medium. Cells were incubated at 37°C in a humidified chamber with saturated atmosphere containing 5% CO2.

3.2.1.2 Cell Passaging

Cell lines were passaged at a confluency of 80 - 90%. The culture medium was removed, and cells was washed once with 1X PBS. Cell lines PaTu-S, Colo357, PaTu-T, PANC-1, Capan-1, and MIAPaCa-2 were incubated with 1.5 ml of 1X Trypsin/EDTA in 1X PBS and Capan-1 with 1.5 ml of 2X Trypsin/EDTA in 1X PBS at 37°C for 10 minutes or 15 minutes, respectively, for cell dissociation. 8.5 ml culture medium was used to stop the reaction. The cell suspension was collected in 15ml falcon tube, centrifuged at 300 xg at room temperature (RT) for 5 minutes and resuspended in fresh cell culture medium. The cell splitting ratio is displayed in Table 14

Table 14 Cell splitting ratio

Cell line	Splitting ratio
PaTu-S	1:10
PaTu-T	1:40
MiaPaCa-2	1:20
PANC-1	1:20
Colo357	1:10
Capan-1	1:4
Capan-2	1:8

3.2.1.3 Cell counting

Cells were counted and seeded into wells and chambers for subsequent experiments. 10 µl of resuspended cells were mixed with an equal volume of 0.4% Trypan Blue solution. 10 µl of the mixture was added to a cell counting slide placed on a TC20 Automated cell counter. The results were presented as live cells/ml.

3.2.1.4 Cell cryopreservation

For cell cryopreservation, the cell suspension was centrifuged after trypsinization at 300 xg for 5 minutes at RT. 3 x 10^6 cells/ml were resuspended in cryopreservation medium in a 1:1 ratio of fresh medium and freezing medium according to the size of the pellet. The freezing medium consists of 80% FBS and 20% DMSO. One ml of the cell suspension was transferred to a 2 ml cryotube. The cryotubes was placed in a cell freezing container filled with isopropanol and store at -80°C for gradient cooling overnight. The next day, the cryotubes were transferred to -150°C for long-term storage.

3.2.1.5 Epigenetic drug treatment

Two inhibitors, A485, which targets the CBP HAT domain, and SAHA (Vorinostat), a pan-HDAC inhibitor affecting class I and class II HDACs, were utilized to treat seven PDAC cell lines for short-term (24h or 96h) and long-term (4-30 weeks) periods. Both inhibitors were dissolved in DMSO, with SAHA at a stock concentration of 50 mM and A485 at a stock concentration of 10 mM, and stored at -80°C up to one year.

Short-term Epigenetic drug treatment

For short-term treatment, all cell lines were treated with either 10 nM or 1 µM of A485 and 10 nM or 0.5 µM of SAHA. The cell culture media containing the epigenetic drugs was changed at 48 hours during the 96-hour treatment period before being used for further experiments.

Long-term epigenetic drug treatment

For long-term treatment, all cell lines were maintained in either 1 µM A485 or 0.5 µM SAHA, with the exception of MIAPaCa-2, which received 0.05 µM SAHA, as MIAPaCa-2 could not survive under 0.5 µM SAHA conditions during long-term treatment. The cell culture media containing epigenetic drugs was exchanged on Mondays, Wednesdays, and Fridays. The treatment duration ranged from 4 to 30 weeks before used for further experiments. Controls were treated with the 1‰ solvent DMSO. Long-term epigenetic drug-treated PDAC cells were cryopreserved after 20 rounds of treatment.

3.2.1.6 Cell proliferation

Cell proliferation was measured by the reduction of soluble yellow 3-(4,5-dimethylthiazol-2-yl)-2,5-diphenyltetrazolium bromide (MTT) into an insoluble purple formazan product. To determine cell proliferation ability after long-term drug treatment, PaTu-S, Colo357, PaTu-T, PANC-1 and MIAPaCa-2 cells were seeded at a density of 2000 cells per well; Capan-1 and Capan-2 at a density of 5000 cells per well in 96-well plates. Directly after seeding, at 0 hours and after 24, 48, 72 and 96 hours, 20 µl of 2.5 mg/ml MTT was added per well and cells were incubated at 37°C with 5% CO2 for 3 hours. After removing the medium carefully, it was replaced with 100 µl DMSO. After 30 minutes incubation, optical density (OD) value was measured at 570 nm and 690 nm using the SpectraMax Plus 384 Microplate Reader.

The growth rate (GR) at 72 hours was measured using the following formula:

$OD_{\text{time point}} = OD_{570nm} - OD_{690nm}$

$GR = ((OD_{96h} / OD_{24h}) * e^{1/72}) - 1) * 100$

3.2.1.7 Colony formation assay

To determine cell colony formation ability after long-term drug treatment, 500 PaTu-T and MIAPaCa2 cells, and 2000 PaTu-S, Capan-1, Capan-2, Colo357 and PANC-1 cells were seeded in one well of 6-well plates. Capan-2, PaTu-T and MIAPaCa2 cell were cultured for 10 days. PaTu-S, Capan-1, Colo357 and PANC-1 cells were cultured for 14 days. During this period, the culture medium containing epigenetic drugs was refreshed every three days to maintain long-term drug treatment conditions. After two times

washing with 1X PBS, cells were fixed with 1 ml of 100% methanol on ice for 10 minutes. The colonies were stained for 15 minutes at RT with 750 µl of 1% crystal violet, prepared by dissolving crystal violet in 100% ethanol. Crystal violet solution was aspirated and plates were washed with distilled water (dH_2O) till free of stain. The plates were left uncovered on lab bench overnight to dry and be photographed next day. Colony density was measured with ImageJ software. Colony formation was expressed as the percentage of colonies per area and normalized to control cells.

3.2.1.8 Cell migration assay

PDAC cell lines were seeded in one well of 6-well plates and grown to confluence. To suppress proliferation PANC-1 cells were treated with 3 µg/ml Mitomycin C at 37°C with 5% CO2 for 3 hours prior to inducing wound scratches. PaTu-S, Capan-2, Colo357, PaTu-T and MIAPaCa-2 cells were treated with 15 µg/ml Mitomycin C under the same conditions. Capan-1 was excluded from the experiment due to cell death when exposed even to very low concentration of Mitomycin C. A wound was inflicted with a scratch by a 200 µl sterile pipette-tip. Cells were washed with 1X PBS and incubated in fresh cell culture medium at 37°C with 5% CO2. Microscopic images of wound healing were captured directly after the scratch at 0 hour and after 6, 15 and 24 hours. The size of the area was quantified by using ImageJ software. Cell migration was quantified as percentage of migrated cells into the scratched area from 0 hour to the measured time point.

The migration in percentage was measured using the following formula:

$$\text{Migration in percentage} = 100 - (\text{Area}_{\text{time point}} / \text{Area}_{\text{0 hour}}) * 100$$

3.2.2 Molecular-biological methods

3.2.2.1 RNA isolation

Total RNA was isolated from cultured cells following the manufacturer's instructions from the RNeasy Plus Mini Kit. The concentration and integrity of the extracted RNA was measured as described below. Extracted RNAs were stored at -80°C for further experiments.

3.2.2.2 RNA-concentration and -integrity measurement

1X TAE buffer	40 mM	Tris-base
	1 mM	EDTA
	20 mM	Acetic acid

The RNA concentration was measured at 260 nm and 280 nm using the SpectraMax Plus 384 Microplate Reader according to manufacturer's instructions. The quality of RNA samples (RNA integrity) was analyzed using agarose gel electrophoresis. RNASE-Existus-Plus was used to clean all equipment before electrophoresis in order to eliminate RNases. To prepare an agarose gel, the components listed below were heated in a microwave at 600 watts for 3 minutes, then transferred to the chamber to cool down at RT. Concurrently, the samples were prepared as listed below and heated at 60°C for 10 minutes. The quality of RNA was assessed based on the integrity of 18S and 28S RNA using UV light in a Fusion FX device.

Components for 120 ml 0.8% RNA agarose gel:

Reagents	Weight/ Volume
Agarose	0.96 g
16%PFA	3 ml
SYBR Safe gel stain	12 µl
1X TAE buffer	117 ml

Components of loading sample:

Reagents	Volume
Formamide	4 µl
6X DNA loading dye	2 µl
Nuclease free water	5 µl
RNA sample	1 µl

3.2.2.3 cDNA synthesis

2 µg of total extracted RNA was reverse transcribed to complementary DNA (cDNA) with the RevertAid First Strand cDNA Synthesis Kit following the manufacturer's instructions. cDNA was diluted with double distilled water (ddH_2O) to 20 ng/µl and stored at -20°C.

3.2.2.4 Quantitative real-time PCR

Gene expression was determined and quantified with quantitative real-time PCR (qRT-PCR) using previously synthesized cDNA. The reaction was performed on a Roche LightCycler®96. The sample preparation scheme is outlined below and qRT-PCR program is given in detail in Table 15. Primer pairs are listed in Table 6. The gene *TBP* (TATA box binding protein) was used as housekeeping gene. Gene expression was quantified by relative mRNA expression (ΔCt-value) or normalized mRNA expression (ΔΔCt-value) in comparison to controls with the formulas provided below.

Pipetting scheme for 15 µl single reaction:

Reagents	Volume
2X FastStart Essential DNA Green Master	7.5 µl
Forward primer (10 µM)	1 µl
Reverse primer (10 µM)	1 µl
Nuclease free water	4.5 µl
cDNA (20 ng/ µl)	1 µl
Total volume	**15 µl**

Table 15 qRT-PCR program

	Step	Temperature	Time	Cycle
Profile	Preincubation	95°C	600s	1 cycle
	3 step amplification	95°C	15s	45 cycles
		55°C	15s	
		68°C	15s	
	Melting curve	95°C	10s	1 cycle
		65°C	60s	
		97°C	1s	
	Cooling	4°C	∞	∞

Formula: Calculation of relative expression and normalized expression

$2^{-\Delta CT} = 2^{-(CT\ target\ gene\ -\ CT\ housekeeper\ (TBP))}$

$2^{-(\Delta\Delta CT)} = 2^{-(\Delta CT\ treatment\ sample\ -\ \Delta CT\ control\ sample)}$

3.2.2.5 RNA sequencing

The packages involved in RNA-seq data analysis processing are listed in Table 12.

The process of RNA sequencing was performed at LAFUGA Lab at the Gene Center of Ludwig-Maximilians-Universität in Munich. The quality of the total RNA was assessed using the 2100 Bioanalyzer (Agilent Technologies, Inc.). RNA integrity number (RIN) greater than 8 is suitable for library construction. Libraries were prepared to enrich Poly(A)-mRNA for RNA sequencing using Version 2: CORALL RNA-Seq V2 Library Prep Kits. Sequencing was executed on the Illumina Nextseq 1000/2000 system. For one sample, 50 base pair single-end reads were generated, resulting in a total of approximately 10 to 20 million reads. The RNA-seq reads underwent trimming using Trim Galore (RRID:SCR_011847; version 0.6.5) to remove adapters and low-quality bases. SortMeRNA was employed to filter out ribosomal (r)RNA and non-eukaryotic

contaminants (RRID:SCR_014402; version 4.3.6). The reads were then aligned to the human genome reference GRCh38 (Ensembl annotation release 100) utilizing the STAR (RRID:SCR_004463; version 2.7.3a). Followed by sorting and indexing the alignments using Samtools (RRID:SCR_002105; version 1.17), raw read counts were generated using HTSeq-count (RRID:SCR_004473; version 2.0.2) based on GRCh38 (Ensembl annotation release 100) annotation. Read counts were normalized via the DESeq2 package (RRID:SCR_015687; version 1.40.2). To facilitate Principal Component Analysis (PCA), log transformation was applied and data were visualized using ggplot2 package (RRID:SCR_014601; version 3.5.0). The differential expression analysis was performed using DESeq2, with thresholds set at a p-value of less than 0.05 and log2 fold change (log2FC) greater than 1 to identify differentially expressed genes (DEGs) between classical and basal-like cell lines. These genes were then subjected to further analysis utilizing the Kyoto Encyclopedia of Genes and Genomes (KEGG) pathways, Gene Ontology (GO) keywords, and Gene Set Enrichment Analysis (GSEA) with the clusterProfiler package (RRID:SCR_016884, version 4.8.2). Genes related to the Rho-GTPases pathway were visualized with a heatmap via the complexHeatmap package (RRID:SCR_017270; version 2.16.0), and EMT scores were derived from existing gene signatures [126].

3.2.3 Epigenetic methods

3.2.3.1 Chromatin immunoprecipitation

Cell lysis buffer	5 mM	PIPES (pH 8)
	85 mM	KCl
	0.5%	Nonidet P-40 (NP-40) (v/v)
Mnase reaction buffer	50 mM	Tris-HCl (pH 8)
	5 mM	CaCl2
Nuclei lysis buffer	1%	SDS (w/v)
	10 mM	EDTA
	50 mM	Tris-HCl (pH 8)
ChIP Dilutionbuffer	0.01%	SDS (w/v)
	1%	Triton X-100 (v/v)
	1.2 mM	EDTA
	16.7 mM	Tris-HCl (pH 8)
	167 mM	NaCl
Low salt wah buffer	0.1%	SDS (w/v)
	1%	Triton X-100 (v/v)
	2 mM	EDTA
	20 mM	Tris-HCl (pH 8)

	150	mM	NaCl
High salt wash buffer	0.1%		SDS (w/v)
	1%		Triton X-100 (v/v)
	2	mM	EDTA
	20	mM	Tris-HCl (pH 8)
	500	mM	NaCl
LiCl wash buffer	250	mM	LiCl
	1%		Nonidet P-40 (NP-40) (v/v)
	1%		DOC (Sodiumdeoxycholat) (w/v)
	1	mM	EDTA
	10	mM	Tris-HCl (pH 8)
Elution buffer	1%		SDS (w/v)
	100	mM	NaHCO3
TE buffer	10	mM	Tris-HCl (pH 8)
	1	mM	EDTA

Establishment of the optimal incubation time of micrococcal nuclease treatment

Before performing chromatin immunoprecipitation (ChIP) analysis, one important step is to adjust the correct DNA fragment size. To do so, cells were seeded in 10 cm² dish and grown to 70%-80% confluence. Afterwards, cells were cross-linked with 1% PBS-buffered formaldehyde (PFA) for 10 minutes at RT. The reaction was stopped with 125 mM glycine for 5 minutes and washed twice with cold 1X PBS on ice. Subsequently, cells were carefully lysed in 500 µl cell lysis buffer containing 1X protease inhibitor on ice to extract nuclei. Lysed cell content was collected and centrifuged at 500 xg for 5 minutes at 4°C. Isolated nuclei were resuspended in 500 µl of MNase reaction buffer and treated with 20 U MNase for 3, 5, 7 and 9 minutes at RT. The reaction was deactivated by adding EGTA at a final concentration of 20 mM. Nuclei were centrifuged at 500 xg for 10 minutes at 4°C and lysed in 200 µl of nuclei lysis buffer containing 1X protease inhibitor on ice for 1 hour and then sonicated for six on-off cycles, 10 seconds each at 10% amplitude. Samples were centrifuged at 12,000 xg for 10 minutes at 4°C. The supernatant was transferred to a new 2 ml reaction tube and incubated with 75 µM NaCl at 65°C overnight to reverse the cross-linking process. Afterwards, RNA and proteins were digested in 0.05 µg/µl RNase for 30 minutes at 37°C and 0.05 µg/µl proteinase K in 10 µM EDTA and 30 µM Tris-HCl for 2 hours at 45°C, respectively. DNA was obtained by ethanol precipitation method. Two volumes of pre-chilled 100% ethanol were added and incubated at -20°C for 2 hours. After 20 minutes centrifugation at full speed at 4°C, the DNA pellet was washed with 70% ethanol and again centrifuged at full speed at 4°C for 15 minutes. Tubes were left open on the lab bench to dry the DNA pellet and DNA was dissolved in

50 µl of nuclease free water. The concentration of DNA was measured at 260 nm and 280 nm using the SpectraMax Plus 384 Microplate Reader. 1.5% Agarose gel was used to detect DNA fragment lengths. DNA fragments ranging from 200 bp to 600 bp were accepted. The agarose gel composition and sample composition are listed below.

Components of 120ml 1.5% agarose Gel:

Reagents	Weight/ Volume
Agarose	1.8 g
SYBR Safe gel stain	12 µl
1X TAE buffer	120 ml

Components of loading:

Reagent	Weight/ Volume
6X DNA loading dye	2 µl
DNA sample	2.5 µg
Nuclease free water	up to 12 µl

Chromatin immunoprecipitation

Once the optimal MNase incubation time has been established, complete chromatin immunoprecipitation (ChIP) experiments were performed. The experimental procedures before MNase incubation are consistent with those described above. Isolated nuclei from the different PDAC cell lines were resuspended in 500 µl of MNase reaction buffer with 20 U MNase and incubated for: 3 minutes for PANC-1, 5 minutes for Capan-1, Capan-2, PaTu-T and MIAPaCa-2 and 6 minutes for PaTu-S and Colo357 at RT. The reaction was inactivated by adding EGTA at a final concentration of 20 mM. Nuclei were centrifuged at 500 xg for 10 minutes at 4°C. The pellet was then lysed in 200 µl nuclei lysis buffer containing 1X protease inhibitor on ice for 1 hour. Following lysis, the samples were sonicated for six on-off cycles, 10 seconds each at 10% amplitude. The sonicated samples were centrifuged at 12,000 xg for 10 minutes at 4°C. Meanwhile, 100 µl Protein an Agarose/Salmon Sperm DNA beads were pre-cleared with 1 ml chilled 1X PBS in a 2 ml reaction tube and centrifuged at 4,000 xg for 1 minute at 4°C. The supernatant was removed, leaving the beads in the tube. The supernatant collected from the nuclei lysis step was then mixed with 1,800 µl ChIP Dilution buffer and transferred to the tube

containing the pre-cleared beads. The mixture was rotated for 1 hour at 4°C. After centrifuging at 4,000 xg for 1 minute at 4°C, 1% Input was collected from each sample and stored at 4°C for later processing. Subsequently, the rest of the supernatant was equally divided for ChIP antibody reaction using 0.3 µg of an H3K27ac antibody and 1 µg of an IgG control antibody, and rotated at 4°C overnight. Immunoprecipitation was enriched with 60 µl agarose beads on a roller for 1 hour at 4°C. Agarose beads were sequentially washed with 1 ml low salt, high salt, LiCl, and twice with TE washing buffer. Each washing step was performed on a shaker for 5 minutes on ice, followed by centrifugation at 4,000 xg for 1 minute at 4°C. Immunoprecipitated chromatin (DNA fragments) was eluted in 100 µl elution buffer for 15 minutes at RT on a roller, then centrifuged at 4,000 xg for 1 minute at 4°C. The supernatant containing the DNA fragment was collected in a new 1.5 ml reaction tube, and this process was repeated once. Input samples were incubated with 200 µl elution buffer for 30 minutes at RT. Afterwards, both the H3K27ac-immunoprecipitated and Input samples were reverse cross-linked in 75 µM NaCl overnight at 65°C. RNA and proteins were digested with 0.05 µg RNase for 30 minutes at 37°C and 0.05 µg proteinase K with 10 µM EDTA and 30 µM Tris-HCl for 2 hours at 45°C. DNA was purified using the QIAquick PCR Purification Kit according to the manufacturer's instructions and quantified by qPCR. ChIP-specific primers were listed in Table 7. Results were calculated using the Percent Input method.

The ChIP enrichment was measured using the following formula:

$$\text{normalized ChIP} = Ct_{ChIP} - (Ct_{Input} - \log_2 100)$$

$$\text{ChIP enrichment} = 2^{-\text{normalized ChIP}} * 100$$

3.2.4 Protein chemical methods

3.2.4.1 Protein extraction

Protein lysis buffer	50 mM	Tris-HCl (pH 8)
	2%	SDS (w/v)

For protein extraction, cells were seeded in a 10 cm² dish and grown to 70%-80% confluence. Cells were washed once with 10 ml chilled 1X PBS. After removing the PBS, cells were lysed in 400 µl protein lysis buffer containing 1X protease inhibitor and 1X phosphatase inhibitor on ice. The cells were scraped from the dish and collected in a 1.5 ml reaction tube. The cell suspension was sonicated for three on-off cycles, 10 seconds each at 10% amplitude, followed by centrifugation at full speed for 20 minutes at 4°C.

The supernatant containing proteins was transferred to a new 1.5 ml reaction tube and stored at -80°C for further experiments.

3.2.4.2 Cytoplasmic and nuclear protein extraction

PDAC cell lines PaTu-S, Capan-1, Capan-2, PaTu-T, PANC-1, and MIAPaCa-2 were used for cytoplasmic and nuclear protein extraction with the NE-PER™ Nuclear and Cytoplasmic Extraction Reagents Kit. The cells were harvested using trypsin-EDTA and then subjected to centrifugation at 500 xg for 5 minutes. The cells were resuspended in 1 ml of 1X PBS, and transferred to a 1.5 ml reaction tube, and centrifuged again at 500 xg for 5 minutes. Subsequently, the supernatant was carefully discarded. Cell pellets were resuspended in 200 µl CERI buffer from the kit containing 1X protease inhibitor. Afterwards, the tube was vortexed at the highest speed for 15 seconds to completely mix the cell pellet, and then incubated on ice for 10 minutes. After this incubation, 11 µl of pre-chilled reagent CER II was added, and the reaction tube was vortexed for 5 seconds at highest speed and then incubated on ice for 1 minute. Then the tube was vortexed again for 5 seconds at highest speed and then centrifuged for 5 minutes at 12,000 xg. The supernatant (cytoplasmic extract) was immediately transferred to a pre-chilled 1.5 ml reaction tube and placed on ice. The pellet containing nuclei was then suspended in 100 µl pre-chilled NER buffer. The nuclei suspension was sonicated for three on-off cycles, 10 seconds each at 10% amplitude. This was followed by centrifugation at 12,000 xg for 10 minutes, and the supernatant (nuclear extract) was immediately transferred to a pre-chilled 1.5 ml reaction tube and placed on ice. The cytoplasmic and nuclear extracts were stored at -80°C for further experiments.

3.2.4.3 Determination of protein concentration

The Pierce™ BCA Protein Assay Kit was used to measure the protein concentration. 10 µl of the protein lysate was pipetted into the wells of a 96-well plate after adding 200 µl of a working reagent mixture, consisting of reagents A and B mixed in a 1:50 ratio to each well. Subsequently, the plate was gently shaken to guarantee complete mixing of the lysate and reagent. The plate was placed in an incubator at 37°C for 30 minutes. After the incubation, the absorbance of each well was measured using the SpectraMax Plus 384 Microplate Reader set to 570 nm. The protein concentration was determined using a standard curve generated from a range of BSA (bovine serum albumin) concentrations: 25 ng/µl, 125 ng/µl, 250 ng/µl, 500 ng/µl, 750 ng/µl, 1000 ng/µl, 1500 ng/µl, and 2000 ng/µl. By plotting the absorbance values of these standards against their respective concentrations, a standard curve was created.

The protein concentration of the unknown samples was determined using the formula derived from this standard curve:

y (protein concentration [µg/µl]) = k (slope) * x (absorbance [nm]) + b (y-intercept).

A coefficient of determination (R^2) greater than 0.99 indicates that the linear model fits the data exceptionally well, and the standard curve can be used for protein concentration measurement.

3.2.4.4 SDS polyacrylamide gel electrophoresis

1X TBS-T (pH 7.4)	20 mM	Tris-base
	150 mM	NaCl
	0.1%	Tween-20 (v/v)
1X Running buffer	192 mM	Glycine
	25 mM	Tris-base
	0.1%	SDS (w/v)
1X Blotting buffer	192 mM	Glycine
	25 mM	Tris-base
	20%	Methanol (v/v)

SDS-polyacrylamide gel electrophoresis (SDS-PAGE) was performed to separate proteins based on their molecular weight, using a gel composed of a 12.5% separating gel and a 4% upper stacking gel (see Table 15). Samples containing nuclear, cytoplasmic, or total protein lysates were mixed with 5X SDS loading dye and denatured by heating at 95°C for 5 minutes and cooling down on ice. Subsequently, 20 µg of denatured samples, along with 5 µl of protein ladder (PageRegular Plus Prestained Protein Ladder), were loaded into the upper stacking SDS-PAGE gel. The electrophoresis chamber was filled with 1X Running Buffer and proteins were run in the upper stacking SDS-PAGE gel at 70V for 30 minutes to align the proteins. Subsequently, electrophoresis was performed at 125V until the loading front exited the SDS-PAGE gel. Following SDS-PAGE, a semi-dry protein transfer was performed. The blotting sandwich was assembled as follows: two pre-wet filter papers were placed at the bottom, followed by a pre-wet 0.45 µm nitrocellulose membrane and the SDS gel. Two more pre-wet filter papers were placed on top. All components were soaked in 1X Blotting Buffer before assembly. The transfer was executed at a constant 25V for 30 minutes using the Trans-Blot Turbo Transfer System. The membrane was incubated in either 5% milk/1X TBS-T (w/v) or 5% BSA/1X TBS-T (w/v) at RT for two hours with gentle shaking to block nonspecific binding. The membrane was then rolled with the primary antibody, diluted as indicated, in 2 ml of 0.1% BSA/1X TBS-T (w/v) overnight at 4°C (see Table 4). The

following day, the membrane was washed three times with 1X TBS-T buffer for 20 minutes each at RT. Subsequently, the membrane was rolled with a horseradish peroxidase (HRP)-linked secondary antibody, targeting the host species of the primary antibody, diluted as indicated, in 2 ml of in 5% milk/1X TBS-T (w/v) for one hour at RT (see Table 5). After three additional washes with 1X TBS-T buffer for 20 minutes each at RT, the bands were visualized in a Fusion Fx device using Clarity or Clarity Max Western ECL Substrate.

Table 15 Two SDS-PAGE gel preparation

Reagent	Separating gel	Stacking gel
Percentage	**12.5%**	**4%**
ddH_2O	3.2 ml	3 ml
30% Acrylamide	4.2 ml	750 µl
Trizma (Tris-base) 1.5M pH 8.8 (HCl)	2.6 ml	-
Trizma (Tris-base) 0.5M pH 6.8 (HCl)	-	1.3 ml
10% SDS	100 µl	50 µl
10% APS	50 µl	25 µl
TEMED	15 µl	10 µl
Total volume	**10 ml**	**5 ml**

3.2.4.5 Immunofluorescence (IF) staining

1X PBS-T	1X	PBS
	0.05%	Tween-20 (v/v)
IF Blocking buffer	1X	PBS
	5%	Donkey serum (v/v)
	1%	10% BSA (v/v)
	0.1%	Triton X-100 (v/v)

15,000 cells per well were seeded on an 8-well chamber slide and cultured overnight to ensure proper attachment. The following day, the cells were fixed with 4% PFA for 5 minutes at RT and then washed three times with 1X PBS-T for 5 minutes each. After washing, the cells were blocked by adding 200 µl of IF Blocking buffer at RT for one hour. Primary antibodies were applied at the indicated dilutions in 100 µl of IF Blocking buffer and incubated overnight at 4°C (see Table 4). The next day, the cells were washed three times with 200 µl of 1X PBS-T for 5 minutes each at RT. This was followed by incubation with the secondary fluorescence-conjugated antibody, diluted as indicated, in 100 µl of IF Blocking buffer for one hour at RT in dark (see Table 5). The cells were then washed three more times with 200 µl of 1X PBS-T for 5 minutes each at RT in dark.

Finally, the cells were mounted in one drop of Fluoroshield Mounting Medium with DAPI (Abcam, Cambridge, GB) and covered with cover slips, staining the nuclei blue. Images of the cell lines were captured using a Zeiss Axio Imager M2 fluorescent microscope at 64x magnification.

3.2.4.6 F-Actin staining with phalloidin conjugates

CytoPainter Phalloidin – iFluor 488 reagent was used for visualization of actin filaments. To measure the formation of actin filament subcompartments such as lamellipodia, filopodia, and stress fibers. 15,000 cells per well were seeded on 8-wells chamber slide and cultured at 37°C with 5% CO2 overnight. The cell culture medium was aspirated and the cells were washed once with 200 µl of 1X PBS for 3 minutes at RT. Subsequently, the cells were incubated in 200 µl of 4% PFA at RT for 10 minutes. Then the cells were washed three times with 200 µl of 1X PBS for 3 minutes each at RT. 100 µL of 1X Phalloidin conjugate working solution was added to each well. The cells were incubated at RT for 1 hour in the dark. Then the cells were washed three times with 200 µl of 1X PBS for 3 minutes each at RT. Finally, the cells were mounted in one drop of Fluoroshield Mounting Medium with DAPI (Abcam, Cambridge, GB) staining the nuclei in blue and covered with cover slips. Images of the cells were captured using a Zeiss Axio Imager M2 fluorescent microscope at 64x magnification.

3.2.5 Statistical and data analysis

The graphical representations of the results and the statistical analysis, including the non-parametric Mann-Whitney test, Kruskal-Wallis test, one-way ANOVA with Fisher's LSD post hoc test, and two-tailed unpaired Student’s t-test, was performed using GraphPad Prism (10.2.1 (339)). A linear relationship between two groups was measured using Pearson correlation. A p-value less than 0.05 was considered statistically significant.

4. Results

4.1 Characteristics of classical and basal-like pancreatic ductal adenocarcinoma cell lines

4.1.1 Pancreatic ductal adenocarcinoma cell lines were categorized into classical and basal-like subtypes based on the expression of specific marker genes

Various studies have categorized PDAC tissue and established PDAC cell lines into classical and basal-like subtypes mostly based on transcriptome profiles [25-31]. As a first step in the present study, the classification of seven human PDAC cell lines PaTu-S, Capan-1, Capan-2, Colo357, PaTu-T, PANC-1, and MIAPaCa-2 into classical and basal-like subtypes was validated. Thus, RNA-seq was employed for whole-transcriptome analysis of all seven PDAC cell lines, and principal component analysis (PCA) was then used to visualize cell clusters. The first principal component (PC1) successfully grouped the cell lines into two distinct clusters. The first cluster consisted of cell lines PaTu-S, Capan-1, Capan-2, and Colo357, while the second cluster included cell lines PaTu-T, PANC-1, and MIAPaCa-2 (Figure 4.1A). Differentially expressed gene (DEG) analysis exhibited that epithelial marker genes, such as *EPCAM*, *ELF3* (E74 like ETS transcription factor 3), and *KLF5*, were expressed in PaTu-S, Capan-1, Capan-2, and Colo357, whereas mesenchymal marker genes like *VIM*, *ZEB1*, and *JUN* (Jun proto-oncogene, AP-1 transcription factor subunit) were highly expressed in PaTu-T, PANC-1, and MIAPaCa-2 cells (Figure 4.1B). Gene set enrichment analysis (GSEA) further supported above findings by showing that genes highly expressed in basal-like cell lines were enriched in the EMT pathway (Figure 4.1C). Based on these data, the human PDAC cell lines PaTu-S, Capan-1, Capan-2 and Colo357 were classified into a classical and PaTu-T, PANC-1 and MIAPaCa-2 into a basal-like subtype. This cell classification is in line with the classical and basal-like molecular characteristics reported previously and confirmed the presence of EMT features in basal-like cell lines [25-31].

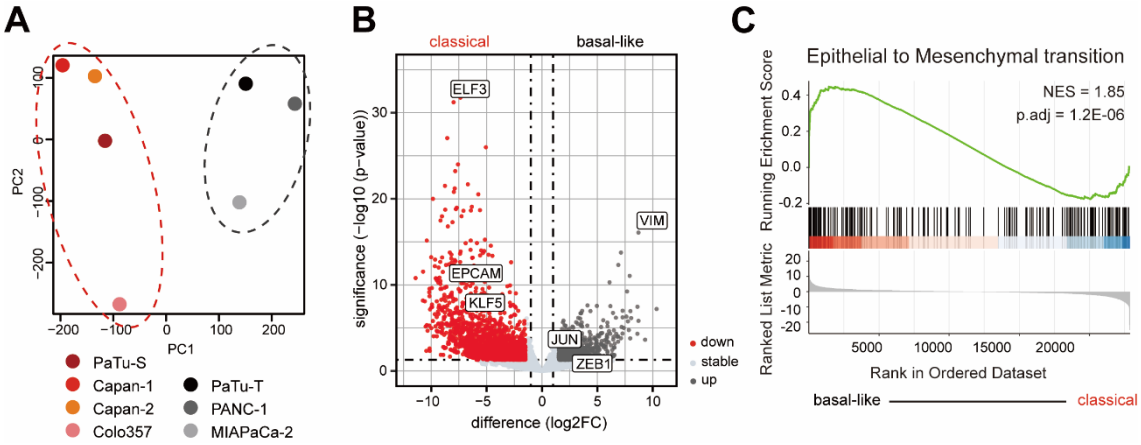

Figure 4.1: Pancreatic ductal adenocarcinoma cell lines were categorized into classical and basal-like subtypes based on the expression of specific marker genes. (A) Principal component analysis (PCA) was performed on RNA-seq data from seven PDAC cell lines and separated cell lines into two clusters (red and grey circle). **(B)** Volcano plot of differentially expressed genes (log2 fold change (FC)) of classical cell lines PaTu-S, Capan-1, Capan-2 and Colo357, as well as basal-like cell lines PaTu-T, PANC-1 and MIAPaCa-2. Highlighted are classical (*ELF3*, *EPCAM*, *KLF5*) and basal-like (*VIM*, *JUN*, *ZEB1*) subtype marker genes. **(C)** Gene set enrichment analysis (GSEA) was performed on RNA-seq data from classical cell lines PaTu-S, Capan-1 and Capan-2 and basal-like cell lines PaTu-T, PANC-1 and MIAPaCa-2; significant enrichment of the epithelial-to-mesenchymal transition (EMT) gene set in basal-like samples (NES = 1.85, p.adj = 1.2E-06). Figure panels reprinted and adapted from publication [127] with permission of the publisher.

4.1.2 Classical and basal-like marker gene expression is regulated by histone acetylation levels

In the next step, it was examined if the expression of specific classical and basal-like marker genes is regulated by the activating histone modification H3K27ac in seven PDAC cell lines. Gene expression of classical marker *ELF3* and basal-like marker *VIM* was detected by qPCR and the results showed high expression of *ELF3* in classical and of *VIM* in basal-like cell lines (Figure 4.2A). Chromatin Immunoprecipitation followed by qPCR (ChIP-qPCR) analyses revealed elevated H3K27ac levels at the promoter of classical marker gene *ELF3* in classical cell lines and very low levels in basal-like cell lines. On the other hand, basal-like cell lines exhibited high levels of H3K27ac enrichment at the basal-like marker gene *VIM* in basal-like cell lines (Figure 4.2B). Plotting the gene expression and levels of H3K27ac enrichment for *ELF3* and *VIM* for all seven PDAC cell lines, a strong epigenetic regulation of these marker genes could be shown in classical and basal-like cell lines (Figure 4.2C). These data confirm that classical cell lines exhibit gene expression of epithelial markers, while basal-like cell lines exhibit gene expression of mesenchymal markers, with significant epigenetic regulation observed in both classical and basal-like cell lines.

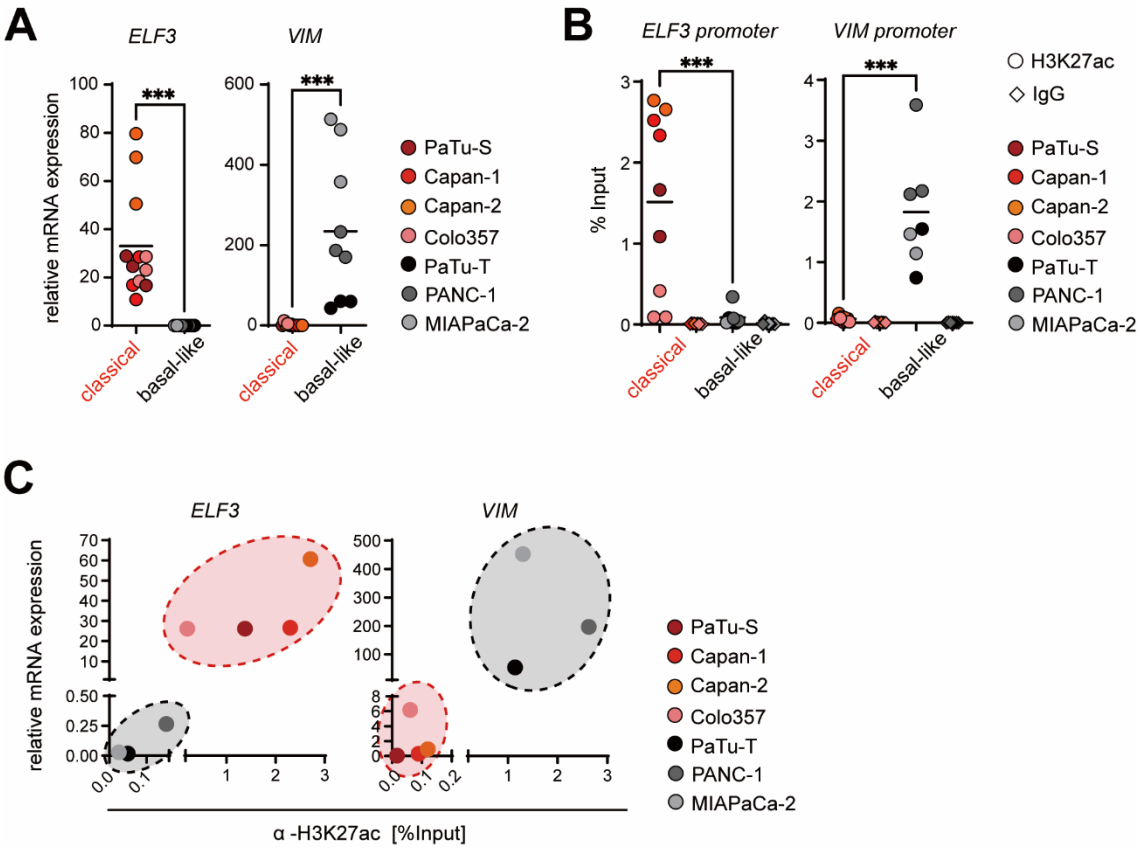

Figure 4.2: Classical and basal-like maker gene expression is regulated by histone acetylation levels. (A) Relative mRNA expression of *ELF3* and *VIM* was measured in all seven PDAC cell lines by qPCR. mRNA expression was normalized to the housekeeper gene *TBP* (n=3). **(B)** H3K27ac levels at *ELF3* and *VIM* gene promoter regions were measured in all seven PDAC cell lines by ChIP-qPCR. ChIP DNA was normalized as percent of input (n=2-3). **(C)** Association between gene expression of *ELF3* and *VIM* and H3K27ac levels at gene promoter regions. Data are reported as mean values. p-values were determined using a two-tailed, unpaired Student's t-test or non-parametric Mann-Whitney test; *** $p < 0.001$. Figure panels reprinted and adapted from publication [127] with permission of the publisher.

4.2 Rho-GTPase pathway and cellular actin organization in classical and basal-like pancreatic ductal adenocarcinoma cell lines

4.2.1 Classical and basal-like pancreatic ductal adenocarcinoma cell lines exhibit differential characteristics in Rho-GTPase pathway components and cellular organization structures

The transcriptome classification of the PDAC cell lines revealed an enrichment of EMT pathways in the basal-like subtype (Figure 4.1C). Notably, actin cytoskeleton rearrangements play a crucial role in the EMT process, and GO term analysis was performed on DEGs of classical PaTu-S, Capan-1, and Capan-2 and basal-like cell lines PaTu-T, PANC-1, and MIAPaCa-2, revealing significant enrichment of processes related to actin cytoskeleton organization. Specifically, the terms 'actin binding' and 'actin

filament network formation' exhibit the highest statistical significance (Figure 4.3A). These findings highlight the importance of actin filament reorganization in classical and basal-like subtype. To prove the changes in the structure of actin filaments in classical and basal-like PDAC cell lines, immunofluorescence staining of Phalloidin conjugates was performed to visualize filamentous actin (F-actin) and cellular organization structures. The results show that F-actin was mostly located at the cell membrane in classical cell lines, whereas F-actin was scattered throughout the cytoplasm in basal-like cell lines (Figure 4.3B). Since Rho-GTPase signaling is a key regulator of the actin cytoskeleton, DEGs of Rho-GTPase signaling components in classical and basal-like cell lines were analyzed by supervised clustering based on the molecular subtype and plotted in heatmaps (Figure 4.3C, all genes of the Rho-GTPase pathway are presented in Suppl. Figure 1A, B, C). The data indicate that components of the Rho-GTPase pathway are generally lower expressed in basal-like cell lines compared with classical cell lines (Figure 4.3C). Although no differential gene expression was observed for the typical Rho-GTPase members *RAC1*, *RHOA*, and *CDC42* between classical and basal-like cell lines, a differential expression of the regulatory Rho-GTPase factors Rho-GEFs, Rho-GAPs, and Rho-GDIs could be seen. Specifically, a decrease in the gene expression of the Rho-GTPase pathway inhibitors *ARHGAP18* and *ARHGDIB* was detected in basal-like cell lines (Figure 4.3C). qPCR and ChIP-qPCR were conducted to confirm a reduced expression of *ARHGAP18* and *ARHGDIB* in basal-like cell lines and to check if the genes are epigenetically regulated by histone acetylation levels, similar to the classical and basal-like markers *ELF3* and *VIM*. The results confirmed a low expression of *ARHGAP18* in basal-like cell lines and a high expression in classical cell lines (Figure 4.3D). Moreover, low levels of H3K27ac were detected at the promoter of *ARHGAP18* in basal-like cell lines, whereas classical cell lines showed an enrichment of H3K27ac at the gene promoter (Figure 4.3E). Plotting the gene expression and levels of H3K27ac enrichment for *ARHGAP18* for six PDAC cell lines, a strong subtype-specific epigenetic regulation of *ARHGAP18* could be shown (Figure 4.3F). However, the gene expression of *ARHGDIB* was not regulated subtype-specific by H3K27ac (Figure 4.3F). Overall, these results demonstrated that classical and basal-like PDAC cell lines exhibit distinct patterns of actin cytoskeleton reorganization, with F-actin primarily located at the cell membrane in classical cell lines and dispersed throughout the cytoplasm in basal-like cell lines. Additionally, the gene expression of the Rho-GTPase inhibitor *ARHGAP18* is regulated subtype-specific by histone acetylation.

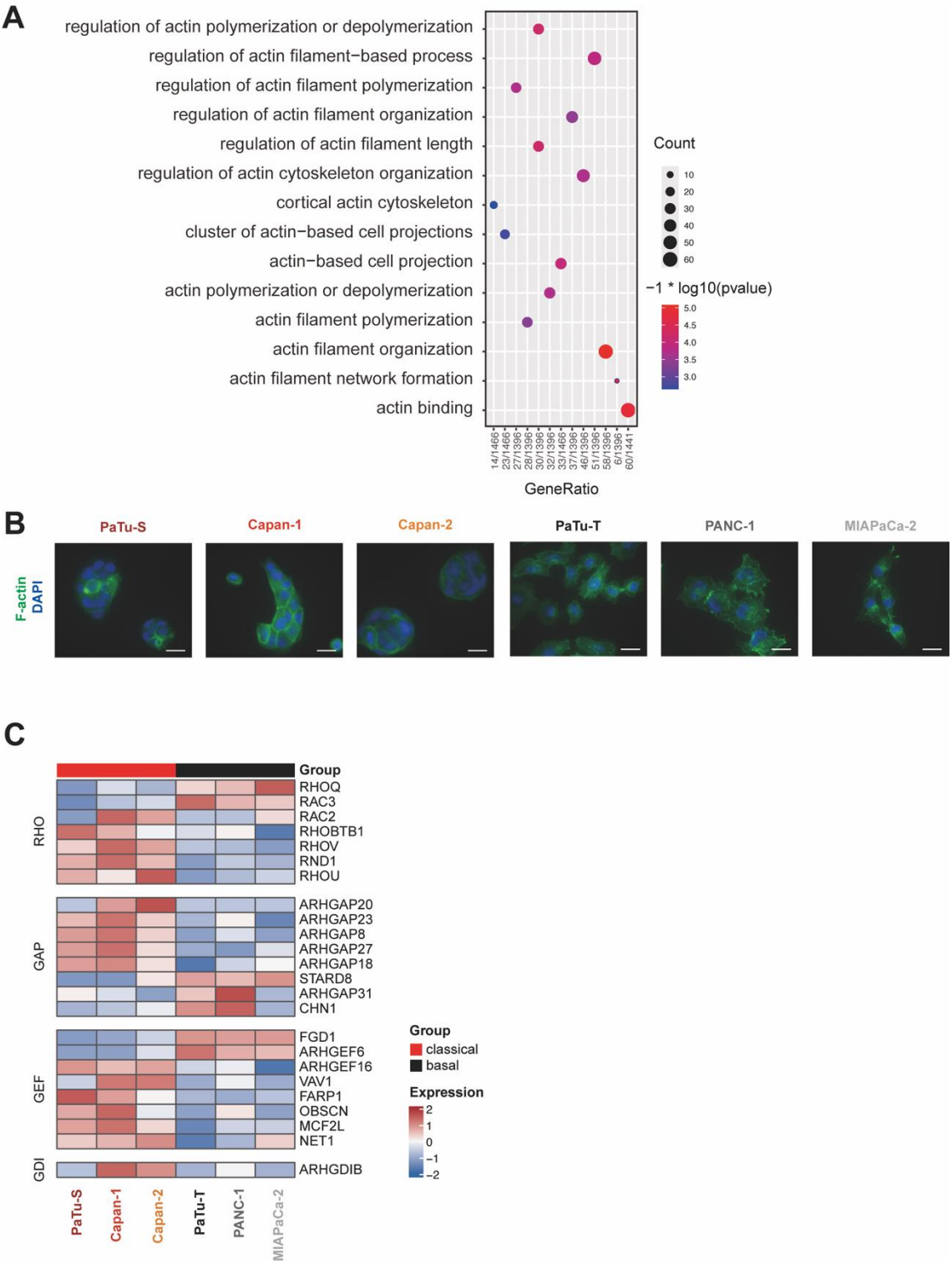
A
regulation of actin polymerization or depolymerization
regulation of actin filament−based process
regulation of actin filament polymerization
regulation of actin filament organization
regulation of actin filament length
regulation of actin cytoskeleton organization
cortical actin cytoskeleton
cluster of actin−based cell projections
actin−based cell projection
actin polymerization or depolymerization
actin filament polymerization
actin filament organization
actin filament network formation
actin binding
14/1466
27/1396
27/1466
28/1396
30/1396
32/1396
33/1466
37/1396
46/1396
51/1396
58/1396
6/1396
60/1441
GeneRatio
Count
10
20
30
40
50
60
−1 * log10(pvalue)
5.0
4.5
4.0
3.5
3.0
B
PaTu-S
Capan-1
Capan-2
PaTu-T
PANC-1
MIAPaCa-2
F-actin
DAPI
C
Group
RHO
RHOQ
RAC3
RAC2
RHOBTB1
RHOV
RND1
RHOU
GAP
ARHGAP20
ARHGAP23
ARHGAP8
ARHGAP27
ARHGAP18
STARD8
ARHGAP31
CHN1
GEF
FGD1
ARHGEF6
ARHGEF16
VAV1
FARP1
OBSCN
MCF2L
NET1
GDI
ARHGDIB
PaTu-S
Capan-1
Capan-2
PaTu-T
PANC-1
MIAPaCa-2
Group
classical
basal
Expression
2
1
0
−1
−2

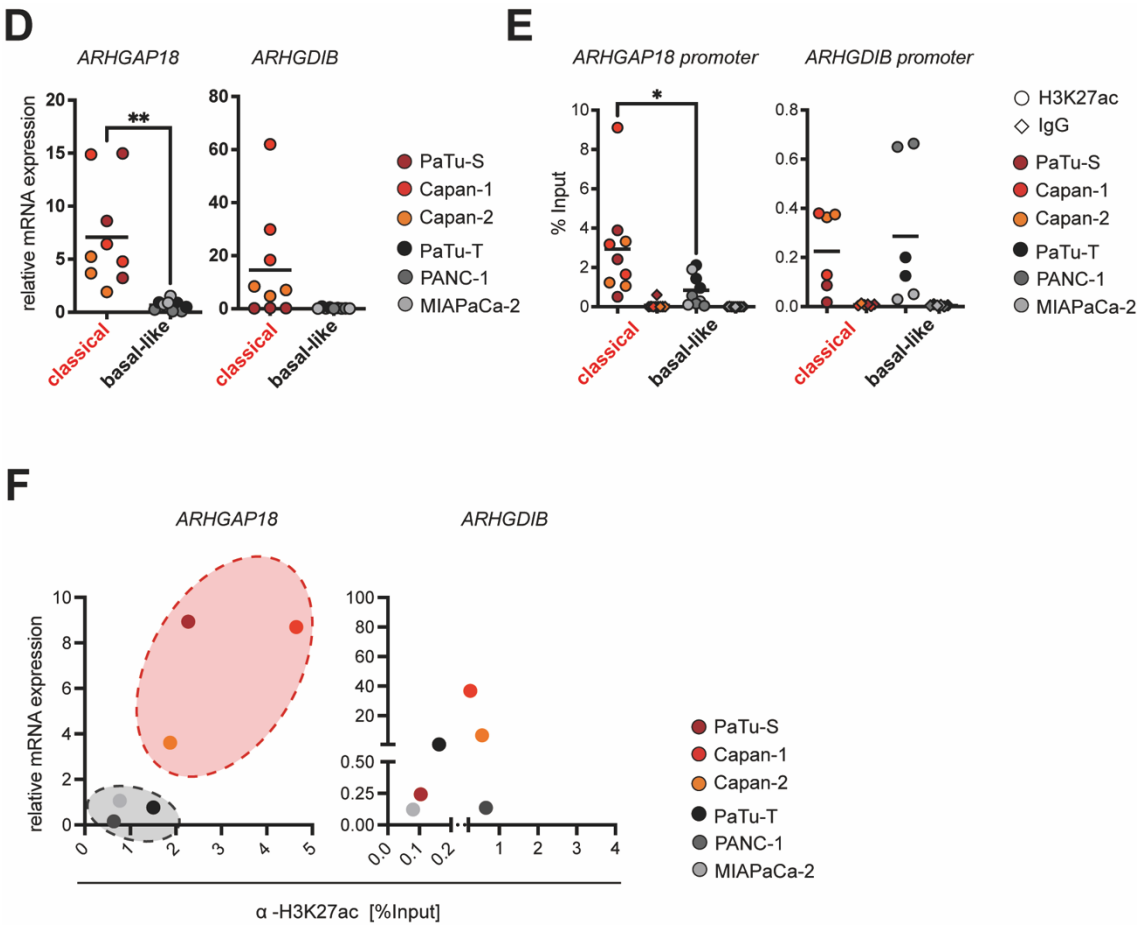

Figure 4.3: Classical and basal-like cell lines exhibit distinct expression of Rho-GTPase pathway components and cellular organization structures. (A) Gene Ontology (GO) analysis for the Biological Process (BP) category was performed on differentially expressed genes (DEGs) identified from RNA-seq data between classical cell lines PaTu-S, Capan-1, and Capan-2 and basal-like cell lines PaTu-T, PANC-1, and MIAPaCa-2, with DEGs selected based on logFC > 1 and $p < 0.05$. Significant enrichment was observed in processes related to actin cytoskeleton organization. **(B)** Phalloidin conjugates were used for F-Actin fluorescence staining (green) and DAPI was used for nuclei staining (blue) in PDAC cell lines PaTu-S, Capan-1, Capan-2, PaTu-T, PANC-1 and MIAPaCa-2 at 64x magnification. Scale bars 20 µm. **(C)** Heatmap of RNA-seq data displays DEGs of Rho-GTPase cycle components in classical cell lines PaTu-S, Capan-1, Capan-2 and basal-like cell lines PaTu-T, PANC-1 and MIAPaCa-2. DEGs were selected based on logFC > 1 and $p < 0.05$. **(D)** Relative mRNA expression of *ARHGAP18* and *ARHGDIB* was measured in PDAC cells PaTu-S, Capan-1, Capan-2, PaTu-T, PANC-1 and MIAPaCa-2 by qPCR. mRNA expression was normalized to the housekeeper gene *TBP* (n=3). **(E)** H3K27ac levels at *ARHGAP18* and *ARHGDIB* gene promoter regions were measured in PDAC cells PaTu-S, Capan-1, Capan-2, PaTu-T, PANC-1 and MIAPaCa-2 by ChIP-qPCR. ChIP DNA was normalized as percent of input (n=3). **(F)** Association between gene expression of *ARHGAP18* and *ARHGDIB* and H3K27ac levels at gene promoter regions. Data are reported as mean values. p-values were determined using two-tailed, unpaired Student's t-test; * $p < 0.1$, ** $p < 0.01$.

4.2.2 Cleaved-ROCK2 displays increased nuclear localization in basal-like PDAC cell lines

Subsequently, RhoA and its downstream effector ROCK2 were given special focus, as they are major components of the typical Rho-GTPase pathway, promoting the formation of linear filaments. Firstly, immunoblot analysis was conducted to measure the protein expression levels of ROCK2 and RhoA in classical and basal-like cell lines. However, no difference in the protein expression levels of ROCK2 and RhoA was observed between the two subtypes. Interestingly, cleaved-ROCK2, an active form of the ROCK2 protein, tended to have increased expression in basal-like cell lines, but this result was not statistically significant (Figure 4.4A). Importantly, the function of the ROCK2 protein is partially determined by its subcellular localization. To investigate this, extracted proteins from the cytoplasm and nucleus were used for immunoblot analysis to detect the subcellular localization of RhoA and ROCK2. The results demonstrated that intact ROCK2 is located in the cytoplasm, while cleaved-ROCK2 is located in the nucleus in both classical and basal-like cell lines. Notably, the basal-like cell lines showed a significant increase in the nuclear levels of cleaved-ROCK2 compared to the classical cell lines. However, RhoA was only detected in the cytoplasm in both classical and basal-like cells (Figure 4.4B). Next, immunofluorescence was performed to confirm the cellular localization of RhoA and ROCK2. Consistent with the immunoblot findings, ROCK2 was found in the nucleus and cytoplasm of all cell lines. Additionally, the basal-like subtype exhibited more numerous and larger ROCK2-positive nucleoli compared to the classical cell lines. In contrast to the immunoblot results, RhoA was observed in both the cytoplasm and the nucleus (Figure 4.4C). Overall, the protein levels of ROCK2 and RhoA do not differ significantly between classical and basal-like PDAC cell lines, but the PDAC cell lines with a basal-like subtype show an increased nuclear presence of the active form of ROCK2 (cleaved-ROCK2).

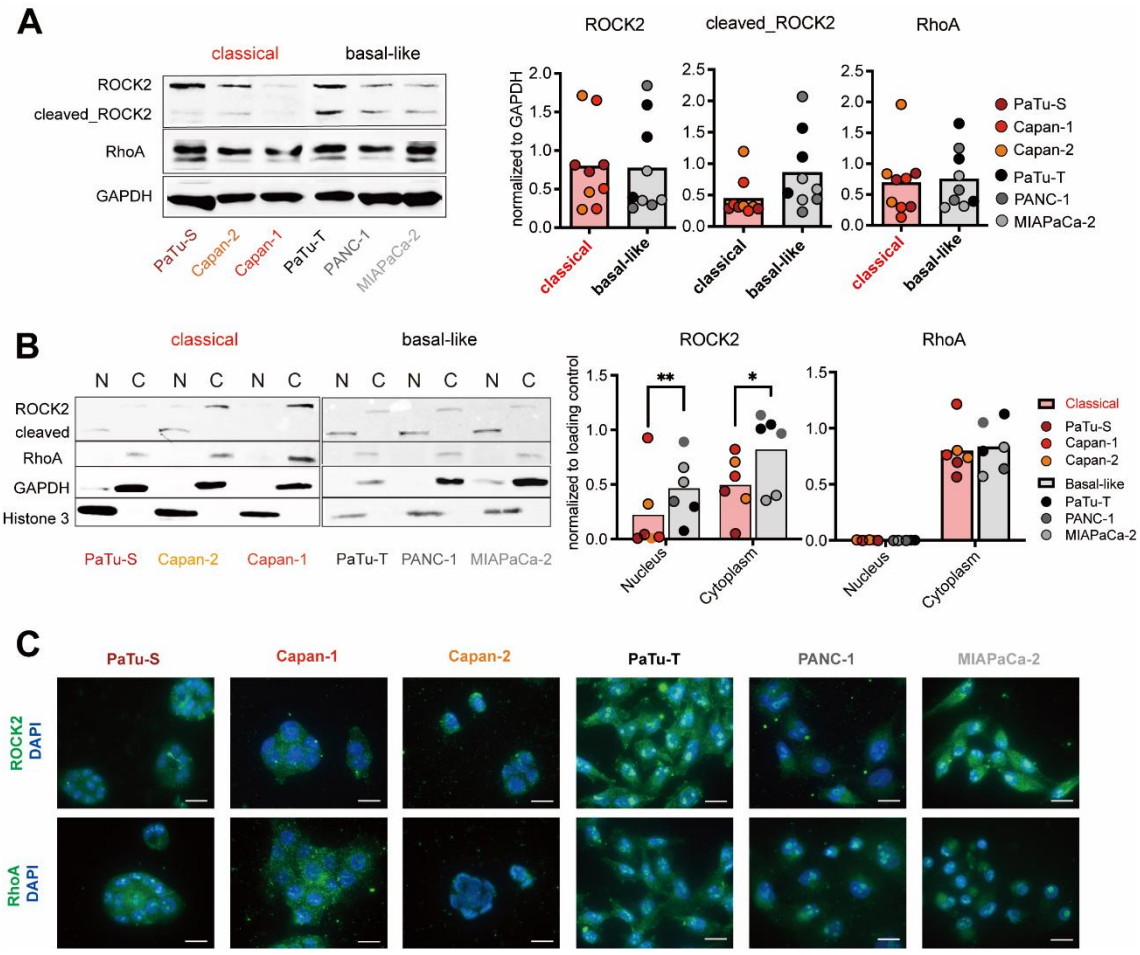

Figure 4.4: Cleaved-ROCK2 displays increased nuclear localization in basal-like PDAC cell lines. (A) Representative immunoblot analysis of ROCK2 and RhoA in PDAC cells PaTu-S, Capan-1, Capan-2, PaTu-T, PANC-1 and MIAPaCa-2. GAPDH served as loading control (n=3). Intensity of bands were quantified and normalized to GAPDH levels. **(B)** Cytoplasmic and nuclear extracted proteins from PDAC cells PaTu-S, Capan-1, Capan-2, PaTu-T, PANC-1 and MIAPaCa-2 were used for immunoblot analysis of ROCK2 and RhoA. GAPDH and histone H3 were used as loading controls for the cytoplasmic and nuclear fractions, respectively (n=2). Intensity of bands were quantified and normalized to GAPDH or histone H3 levels. **(C)** Upper panel: immunofluorescence staining of ROCK2 (green) and nuclei (DAPI, blue); lower panel: immunofluorescence staining of RhoA (green) and nuclei (DAPI, blue) of PDAC cells PaTu-S, Capan-1, Capan-2, PaTu-T, PANC-1 and MIAPaCa-2 at 64x magnification. Scale bars 20 µm. Data are reported as mean values. p-values were determined using two-tailed, unpaired Student's t-test; * $p < 0.1$, ** $p < 0.01$.

4.2.3 ROCK inhibitor Y-27632 do not influence HDAC2 phosphorylation and actin cytoskeleton reorganization in PDAC cell lines

As described above, the basal-like subtype is considered to be more aggressive and more difficult to treat. Thus, it was tested, if ROCK inhibition results in changes in the phenotype of the basal-like PDAC cells, particularly in actin cytoskeleton reorganization, compared to classical cell lines. Moreover, because active ROCK2 was detected in the nucleus (Figure 4.4C), it was assumed that ROCK2 may phosphorylate HDAC2 in the nucleus to activate it. Consequently, this would result in a loss of H3K27ac and an epigenetic silencing of classical marker genes such as *ELF3*, or the Rho-GTPase

inhibitor *ARHGAP18* (Figure 4.2C and Figure 4.3D). To verify this hypothesis, classical and basal-like cell lines were treated with Y-27632, a ROCK inhibitor, at concentrations of 5 µM and 10 µM for 24 hours. Immunoblotting was then performed to assess the effect of ROCK inhibitor on the phosphorylation of HDAC2. However, the treatment of classical and basal-like cell lines with the ROCK inhibitor Y-27632 did not induce any differences in the protein expression of ROCK2 and RhoA, and no alterations were found in the phosphorylation of HDAC2 (Figure 4.5A). Because after ROCK inhibition no effect was observed at protein level, immunofluorescence staining using phalloidin conjugates was performed to determine whether the ROCK inhibitor changed the cellular actin organization in the selected classical cell line Capan-1 and the basal-like cell line PANC-1. However, the cytoskeleton of both Capan-1 and PANC-1 cells remained unaffected (Figure 4.5B), indicating that PDAC tumor cells are non-responsive to the ROCK inhibitor Y-27632 at the chosen conditions.

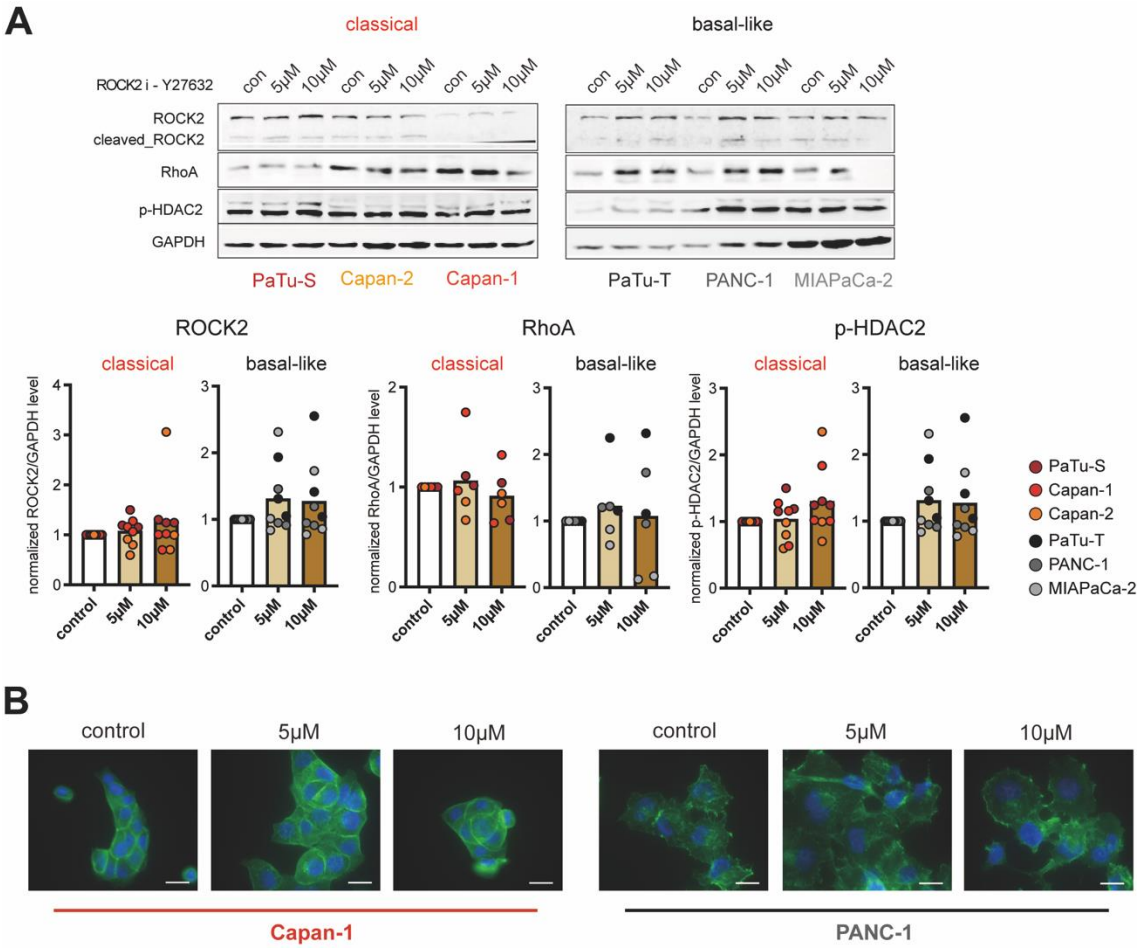

Figure 4.5: ROCK inhibitor Y-27632 do not influence HDAC2 phosphorylation and actin cytoskeleton reorganization in PDAC cell lines. (A) Representative immunoblot analysis of ROCK2, RhoA and P-HDAC2 in control-, 5 µM and 10 µM ROCK inhibitor Y-27632 treated cell lines for 24 hours. Intensity of bands were quantified and normalized to GAPDH levels. GAPDH served as loading control (n=3). **(B)** Phalloidin conjugates were used for F-actin fluorescence staining (green), and DAPI was used for nuclei staining (blue) in control, 5 µM, and 10 µM ROCK inhibitor Y-27632-treated classical Capan-1 and basal-like PANC-1 cells for one hour. Images

were taken at 64x magnification. Scale bars represent 20 µm. Data are reported as mean values. p-values were determined using non-parametric Kruskal-Wallis followed by Dunn's test.

4.3 Epigenetic drug response in classical and basal-like PDAC cell lines

4.3.1 Distinct histone acetylation patterns and differential responses to epigenetic drugs in classical and basal-like cell lines

The results above have shown that the gene expression of the classical marker *ELF3*, the basal-like marker *VIM*, and the Rho-GTPase inhibitor *ARHGAP18* are regulated by histone acetylation. Thus, it was investigated if the overall histone acetylation status and the expression of histone-modifying enzymes is changed in general in classical and basal-like cells. To address this, variations in global H3K27ac levels and the expression of related histone-modifying enzymes were assessed in classical and basal-like PDAC cell lines using immunoblot and qPCR analyses. The results revealed significantly increased protein expression of HDAC2 and a lower abundance of H3K27ac in basal-like cell lines compared to classical cell lines (Figure 4.6A). This finding is consistent with the observation that significantly lower levels of the histone acetyltransferase (HAT) genes *EP300* and *CREBBP* are expressed in basal-like cells than in classical cell lines (Figure 4.6B). To further investigate whether more activated HDAC2 is present in basal-like cell lines, immunoblotting was performed to detect phospho-HDAC2 in both classical and basal-like cell lines (Figure 4.6C). It was found that basal-like cell lines exhibited significantly increased protein expression of phospho-HDAC2 compared to classical cell lines. These findings suggest that differences in histone acetylation and deacetylation dynamics may contribute to the regulation of gene expression in classical and basal-like subtypes.

A comprehensive understanding of the impact of histone acetylation levels regulating transcriptome profiles in classical and basal-like cell lines is necessary to determine whether epigenetic remodeling can affect the switch between tumor subtypes. To investigate this, all seven PDAC cell lines were treated with the histone acetyltransferase inhibitor (HATi) A485 and the histone deacetylase inhibitor (HDACi) SAHA at concentrations of 1 µM A485 or 0.5 µM SAHA for 24 hours. RNA-seq analysis was performed to determine changes in gene expression profiles. Overall, more downregulated genes than upregulated genes were observed in A485-treated PDAC cell lines (Figure 4.6D). The number of differentially expressed genes (DEGs) after SAHA treatment was found to be very low (Figure 4.6D). To determine the biological effects of HATi and HDACi treatment on tumor subtypes, GO term and KEGG pathway analysis

based on DEGs was performed. A Gene Ontology (GO) analysis of the top 100 terms, focusing on genes downregulated by A485 treatment in both classical and basal-like cell lines, identified 54 subtype-specific GO terms (Figure 4.6E). Among them, the expression of genes related to mesenchymal cell differentiation and extracellular matrix organization was reduced in basal-like cell lines. In addition, the analysis of the top 100 GO terms of genes upregulated following SAHA treatment showed significant enrichment in GO terms related to cytoskeletal organization, leukocyte-mediated immunity, and cell secretion in classical cell lines (Figure 4.6E). This finding further demonstrates that cytoskeletal reorganization in classical and basal-like cells is epigenetically regulated.

Further analysis was performed to determine the subtype-specific effects of HATi A485 and HDACi SAHA treatment on EMT in classical and basal-like cell lines by examining an EMT signature identified by Groger et al. [112]. The EMT signature is defined by genes associated with mesenchymal cell differentiation and cytoskeletal organization [112]. It was observed that the EMT score of basal-like cell lines was generally higher than of classical cell lines, which is consistent with the results of GSEA in Figure 4.1C. The EMT score did not change after epigenetic drug treatment in basal-like cell lines. Interestingly, in classical cell lines, treatment with HATi A485 led to an increase in EMT scores, indicating that the EMT phenotype is enriched (Figure 4.6F).

In summary, compared to classical cell lines, basal-like cell lines exhibit elevated HDAC2 expression and activation, accompanied by decreased HAT (*EP300* and *CREBBP*) expression. Classical cell lines respond better to histone-modifying enzyme inhibitors, particularly HATi A485, while both subtypes cell lines show limited sensitivity to HDACi SAHA. In basal-like cell lines, HATi treatment inhibits mesenchymal differentiation, whereas HDACi treatment induces cytoskeletal reorganization. However, in classical cell lines, HATi A485 treatment leads to an enrichment of an EMT program.

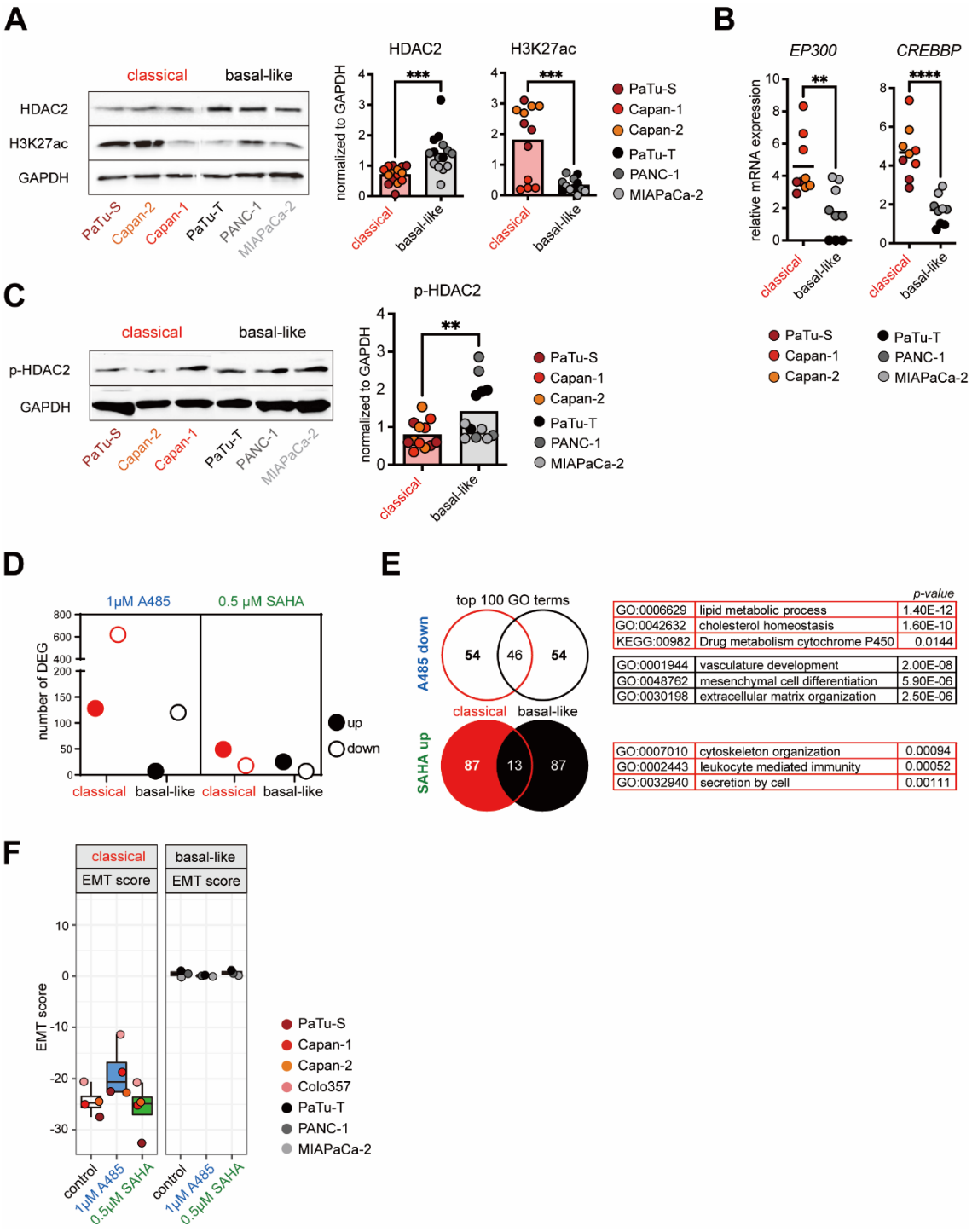

Figure 4.6: Distinct histone acetylation patterns and differential responses to epigenetic drugs in classical and basal-like cell lines. (A) Representative immunoblot analysis of HDAC2 and H3K27ac in PDAC cell lines PaTu-S, Capan-2, Capan-1, PaTu-T, PANC-1 and MIAPaCa-2. GAPDH served as loading control (n=4-5). Intensity of bands were quantified and normalized to GAPDH levels. **(B)** Relative mRNA expression of *EP300* and *CREBBP* in PDAC cells (PaTu-S, Capan-1, Capan-2, PaTu-T, PANC-1, MIAPaCa-2) was assessed using qPCR. Expression levels were normalized to the housekeeping gene TBP (n=3). **(C)** Representative immunoblot analysis of phospho-HDAC2 in PDAC cell lines PaTu-S, Capan-2, Capan-1, PaTu-T, PANC-1 and MIAPaCa-2. GAPDH served as loading control (n=3). Intensity of bands were quantified and normalized to GAPDH levels. **(D)** The count of differentially expressed genes (DEGs), shown as filled circles for upregulated and empty circles for downregulated, was determined via RNA-seq for control, A485- (1 µM, 24 hours), and SAHA- (0.5 µM, 24 hours) treated cell lines. **(E)** Venn diagram illustrates the overlap and distinctiveness of the Top 100 GO terms derived from A485-downregulated and SAHA-upregulated genes. The accompanying tables highlight significant

pathways for genes downregulated by A485 and those upregulated by SAHA, distinguished in classical (red) and basal-like cell lines (black). Basal-like cell lines showed no significant pathway enrichment post-SAHA treatment. **(F)** Changes in EMT signatures, based on published gene signatures [126], were visualized for control, A485- (1 µM, 24 hours), and SAHA- (0.5 µM, 24 hours) treated cell lines using RNA-seq data. Data are reported as mean values. p-values were determined using two-tailed, unpaired Student's t-test; ** $p < 0.01$, *** $p < 0.001$, ****$p < 0.0001$. Figure panels reprinted and adapted from publication [127] with permission of the publisher.

4.3.2 Long-term epigenetic drug treatment differentially affects marker gene expression and epigenetic acetylation in classical and basal-like PDAC cell lines

The effects of short-term epigenetic treatment on cell lines were not as strong as expected, particularly the classical and basal-like cell lines did not respond well to HDACi treatment, and the basal-like cell lines responded only weakly to both HATi and HDACi. Therefore, a long-term treatment analysis was performed to determine whether longer epigenetic treatment would have a more substantial impact on the transcriptional reprogramming of tumor cells. The cell lines were cultured with A485 and SAHA for several weeks. Prolonged treatment with 1 µM A485 significantly reduced H3K27ac levels in both classical and basal-like cell lines, whereas exposure to 0.5 µM SAHA (or 0.05 µM for MIAPaCa-2) did not cause a significant H3K27ac enrichment, though an increasing trend was observed (Figure 4.7A, B). The effects of long-term HATi or HDACi treatment on epithelial and mesenchymal characteristics of classical and basal-like cell lines were examined in the following. After long-term exposure to A485, a significant decrease in *ELF3* expression and an increase in *VIM* expression were observed in classical cell lines, indicating a transition from an epithelial to a mesenchymal phenotype (Figure 4.7C). This is consistent with the results observed following short-term A485 treatment, where an increase in the EMT score was noted in classical cell lines (Figure 4.6F). In line with gene expression, a notable reduction of H3K27ac at the *ELF3* promoter and an increase of H3K27ac at the *VIM* promoter were observed in classical cell lines after long-term A485 treatment, while similar changes were not shown in basal-like cell lines (Figure 4.7D). Additionally, the effect of long-term HDACi treatment on the expression of the Rho-GTPase inhibitor *ARHGAP18* in classical and basal-like cell lines was also assessed. However, basal-like cell lines responded only weakly to SAHA treatment, showing a trend of increased gene expression of *ARHGAP18* and increased H3K27ac levels at the *ARHGAP18* promoter (Figure 4.7E, F). In summary, long-term HATi treatment led to changes in the overall H3K27ac levels in classical and basal-like cells. Specifically, classical cell lines showed decreased expression of epithelial marker genes and increased expression of mesenchymal marker genes after HATi treatment. The basal-like cell line showed a mild increase of the Rho-GTPase inhibitor *ARHGAP18* after HDACi treatment.

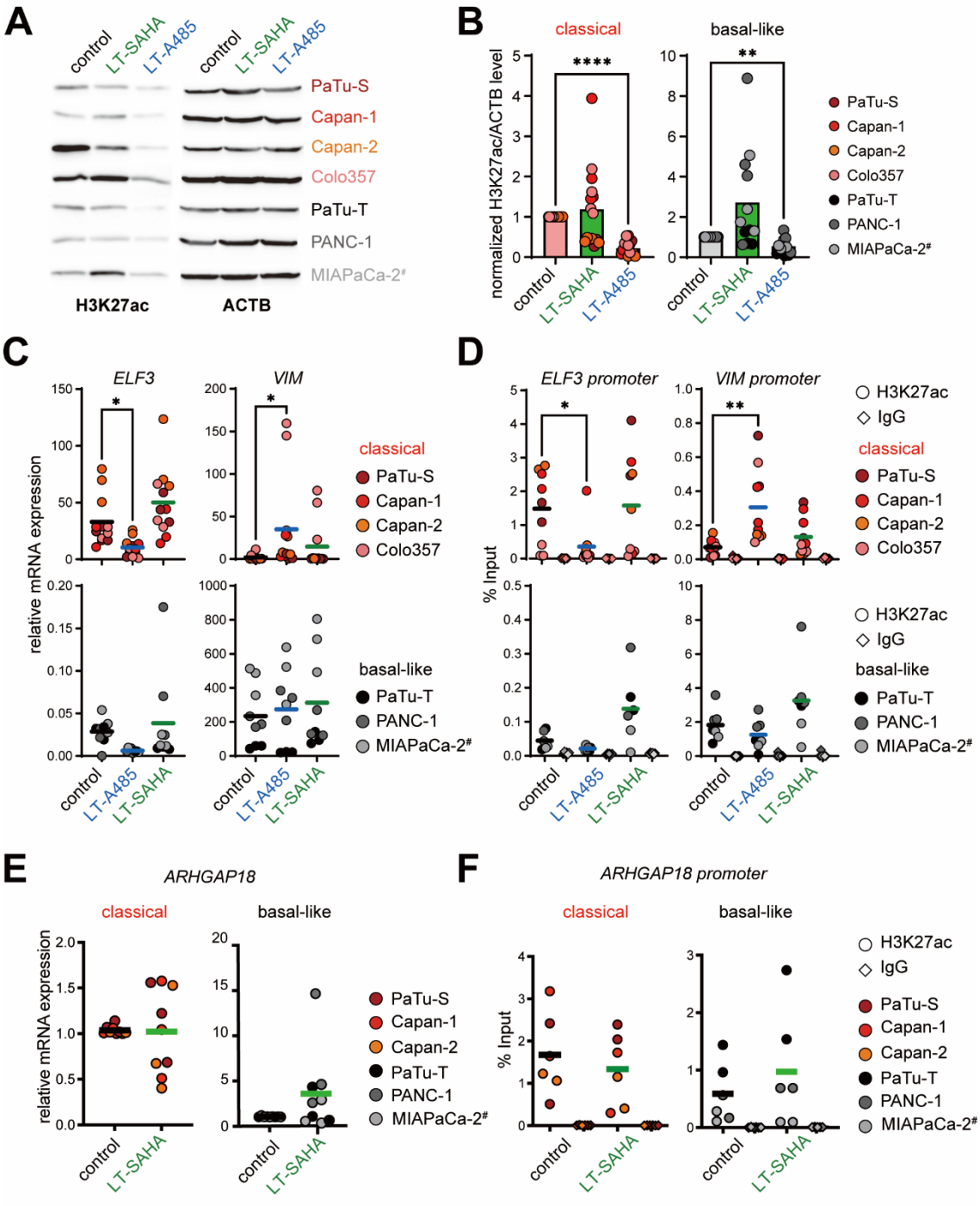

Figure 4.7: Long-term treatment with epigenetic drugs influences epithelial and mesenchymal gene expression differently in classical and basal-like PDAC cell lines. (A) Representative immunoblot analysis of H3K27ac in control-, 1 µM A485- and 0.5 µM (#0.05 µM) SAHA-long-term (5-19 weeks) -treated cell lines. **(B)** Intensity of bands were quantified and normalized to ACTB levels. ACTB served as loading control (n=3-4). **(C)** mRNA expression levels of *ELF3* and *VIM* were evaluated in cell lines subjected to long-term (4-16 weeks) treatment with 1 µM A485 or 0.5 µM (#0.05 µM) SAHA, using qPCR. Expression was normalized to the *TBP* housekeeping gene (n=3). **(D)** ChIP analysis of H3K27ac and control antibody IgG for the promoters of *ELF3* and *VIM* was performed on cell lines treated long-term (18-28 weeks) with 1 µM A485 or 0.5 µM (#0.05 µM) SAHA. ChIP-qPCR results are expressed as a percentage of input (n=2-3). **(E)** mRNA expression of *ARHGAP18* in control- and 0.5 µM (#0.05 µM) SAHA-long-term (4-16 weeks)-treated cell lines were assessed by qPCR and normalized to the housekeeper gene *TBP* (n=3). **(F)** ChIP analysis of H3K27ac and control anti was assessed by qPCR and normalized to the housekeeper gene body IgG for *ARHGAP18* promoter in control- and 0.5 µM (#0.05 µM) SAHA-long-term (18-28 weeks) treated cell lines. ChIP-qPCR data are normalized as percent of

input (n=2-3). Data are reported as mean values. p-values were determined using non-parametric Kruskal-Wallis followed by Dunn's test or one-way ANOVA with Fisher's LSD post hoc test; * $p < 0.1$, ** $p < 0.01$, **** $p < 0.0001$. Figure panels reprinted and adapted from publication [127] with permission of the publisher.

4.3.3 Impact of long-term epigenetic drug treatment on phenotypes of classical and basal-like PDAC cell lines

As shown in Figure 4.4C, basal-like cell lines have larger and more numerous nucleoli, which are generally indicative of a stronger proliferation capacity. Therefore, the impact of long-term HATi or HDACi treatment on proliferation and colony formation of classical and basal-like cell lines was evaluated by MTT assay and colony formation assay, respectively. After 4-30 weeks of treating all seven PDAC cell lines with 1 µM A485 or 0.5 µM (or 0.05 µM for MIAPaCa-2) SAHA, the MTT assay was determined over 24-96 hours, and the colony formation assay was determined over 7-14 days. Combining the results of the MTT assay and the colony formation assay, several patterns emerged following long-term treatment with A485 and SAHA. After long-term A485 treatment, classical cell lines exhibited a consistent response across both assays. Specifically, Capan-1 cells showed increased proliferation, whereas the proliferation of the other classical cell lines was reduced. In contrast, basal-like cell lines did not respond to A485 treatment in the MTT assay but showed reduced colony forming abilities in the colony formation assay. Interestingly, after long-term treatment with SAHA, basal-like cell lines demonstrated a consistent response in both assays. PANC-1 cells showed reduced proliferation, while the proliferation of other basal-like cell lines remained unchanged. In the classical cell lines, all showed reduced proliferation in the MTT assay. However, in the colony formation assay, Capan-2 was the only classical cell lines with reduced colony forming abilities, while the others were unaffected (Figures 4.8A, B).

During EMT, epithelial cells undergo a loss of polarity and intercellular adhesion, properties, but gain the ability to migrate. Therefore, the impact of long-term HATi or HDACi treatment on the migration of classical and basal-like cell lines was evaluated. Cell migration was assessed using a wound healing assay in PDAC cell lines PaTu-S, Capan-2, Colo357, PaTu-T, PANC-1 and MIAPaCa-2 following long-term epigenetic drug treatment. After 17-32 weeks of treatment with 1 µM A485 or 0.5 µM (or 0.05 µM for MIAPaCa-2) SAHA, wound healing was measured over 6-24 hours. Classical cell lines exhibited a notable enhancement in migratory capacity after long-term treatment with A485. However, basal-like cell lines showed only weak responses to both A485 and SAHA treatments, with no significant changes in migration capacity (Figures 4.8E, F).

This phenomenon is consistent with changes observed in the transcriptome, including an increased EMT score in classical cell lines after short-term A485 treatment, a decrease in the expression of the epithelial marker *ELF3*, and an increase in the expression of the mesenchymal marker *VIM* after long-term A485 treatment.

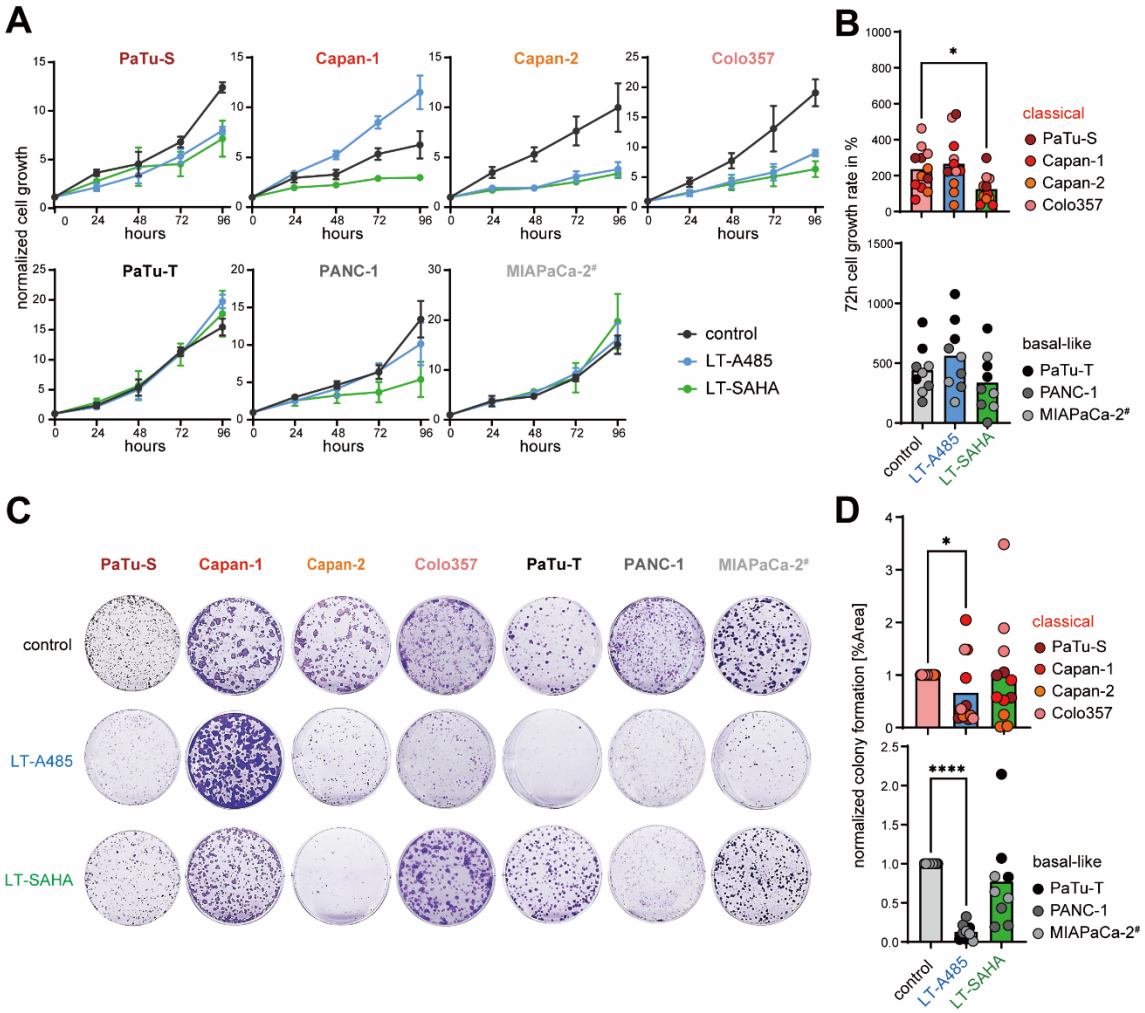

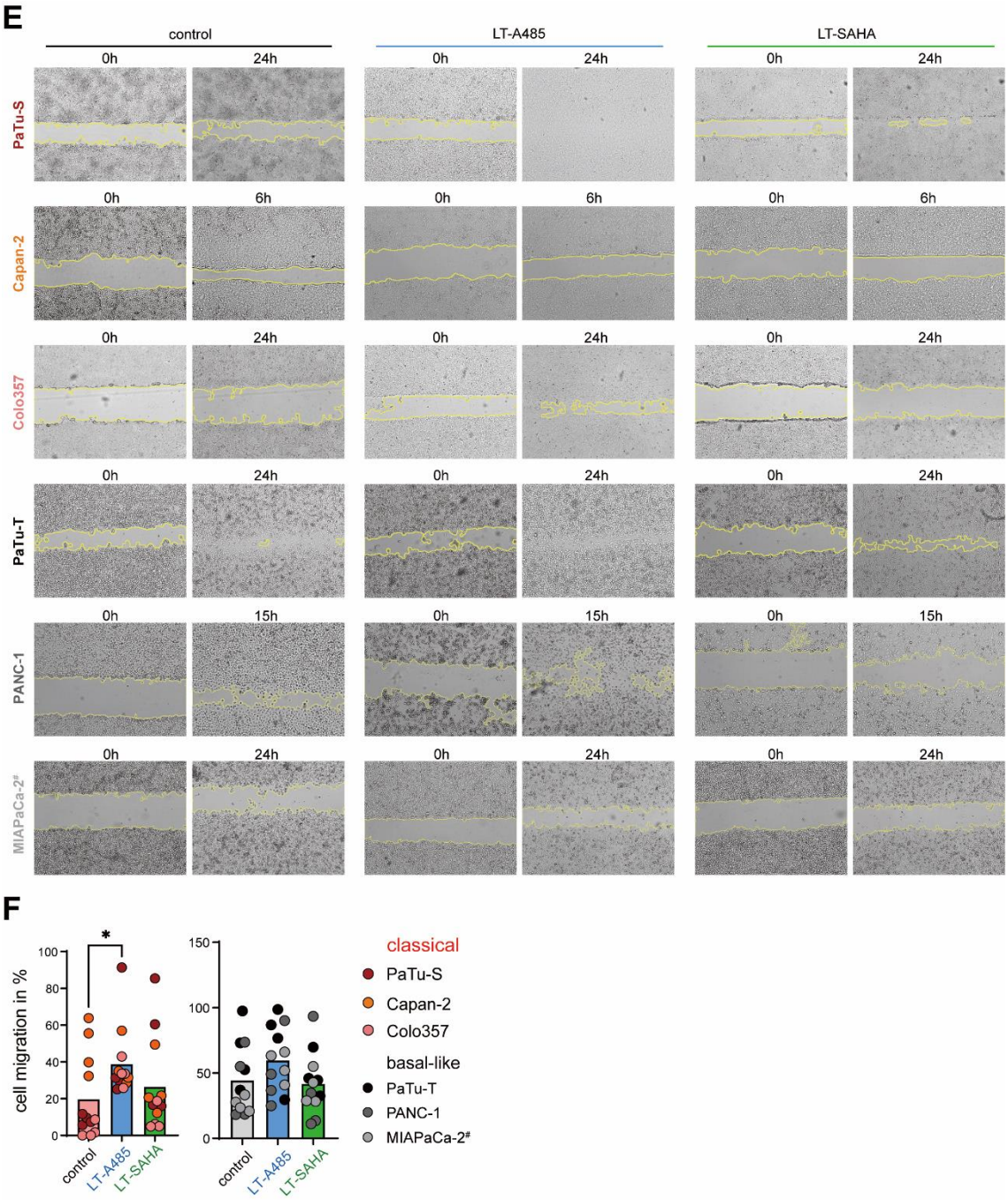

Figure 4.8: Impact of long-term epigenetic drug treatment on phenotypes of classical and basal-like PDAC cell lines. (A) Cell proliferation over 24-96 hours of cell lines treated long-term (4-30 weeks) with 1µM A485 or 0.5 µM (# 0.05µM) SAHA, and controls, was assessed using MTT assay (n=3). **(B)** The cell proliferation rate over 72 hours was evaluated using MTT assay (n=3). **(C)** The ability of cell lines to form colonies after long-term (18-29 weeks) treatment with 1µM A485 or 0.5 µM (#0.05 µM) SAHA was evaluated (n=3). **(D)** Colony formation is expressed as the percentage of colonies per unit area, normalized to control cells. **(E)** Migration capabilities of cell lines treated long-term (17-32 weeks) with 1 µM A485 or 0.5 µM (#0.05 µM) SAHA were assessed (n=4). **(F)** Cell migration was quantified as a percentage of the reduction in the scratch area from the 0 hour to the area at the end of the time point. Data are reported as mean values. p-values were determined using non-parametric Kruskal-Wallis test; * $p < 0.05$, **** $p < 0.0001$. Figure panels reprinted and adapted from publication [127] with permission of the publisher.

5. Discussion

To date, the prognosis for patients with pancreatic ductal adenocarcinoma (PDAC) remains very poor, reflected in a five-year survival rate of only 13% in the United States [3]. The absence of early diagnostic markers, the refractory chemotherapy resistance observed in advanced-stage patients, and the limitations of targeted therapies do all contribute to this dismal outcome. In addition, tumor heterogeneity is a significant factor contributing to the aggressive nature of the cancer in advanced PDAC patients. As demonstrated by multiple publications based on transcriptional profiling, PDAC tumor cells can be classified into two major subtypes: classical, characterized by epithelial marker gene expression, and basal-like, characterized by mesenchymal marker gene expression [25-31]. However, the inherent complexity of tumor tissue composition in PDAC, with few tumor cells and the presence of diverse cellular components in whole tumor samples used for transcriptional profiling analysis, often leads to imprecise classifications [25]. Quite unexpected, the study by Juiz et al. clearly identified heterogeneity within classical subtype PDOs. These PDOs that were originally defined as pure classical exhibited both classical and basal-like transcriptional signatures, highlighting the variability within supposed homogeneous subtypes [32]. It underscores the necessity for a more refined and straightforward model to precisely differentiate distinct tumor cell subtypes and to observe their responses to chemotherapy. To address subtype specific effects and treatment options, seven PDAC cell lines were used for RNA-seq analysis, followed by PCA to categorize these cell lines into two distinct groups. DEGs between the two groups were displayed by a volcano plot, showing one group with epithelial and the other with mesenchymal transcriptional profiling, consistent with previously defined classical and basal-like subtypes [25-31]. Additionally, GSEA results revealed an enrichment of the epithelial-to-mesenchymal transition (EMT) pathway in basal-like cell lines, consistent with the findings of Chan-Seng-Yue et al. from single-cell RNA-seq analysis, which show a strong association between purely basal-like transcriptional signatures and the EMT process [30]. Similarly, the study by Lomberk et al. found that in basal-like patient-derived tumor xenografts (PDTXs), genes with active epigenetic modifications (H3K27ac) are closely linked to oncogenic EMT-associated TGF-β signaling pathways [128]. The findings corroborate that distinct molecular pathways are active in classical and basal-like cell lines, which emphasize potential implications for targeted therapeutic strategies.

It was further verified that the epithelial marker gene *ELF3* and the mesenchymal marker gene *VIM* exhibited elevated expression in the classical and basal-like cell lines, respectively. Their transcriptional activation was correlated with H3K27ac enrichment at their promoter regions. This result is consistent with the findings of Diaferia et al., who

established that low-grade PDAC cell lines CFPAC-1, Capan-2, HPAF-II, and Capan-1 exhibited classical signature, while high-grade PDAC cell lines PANC-1, MiaPaCa-2 and PT45P1 exhibited mesenchymal signature [33]. Moreover, in their study the classification based on the enrichment of H3K27ac at promoters and enhancers was largely overlapping with the low-grade and high-grade classification that was defined by transcriptional profiles. For example, the epithelial marker *KLF5* was highly expressed in low-grade PDAC cell lines and also showed high enrichment of H3K27ac at its enhancers [33]. Lomberk et al. also identified a unique epigenetic landscape in classical subtype tumors utilizing PDAC patient-derived xenograft models, that was characterized by super enhancers of epithelial-related genes such as *GATA6*, *FOS* (Fos proto-oncogene, AP-1 transcription factor subunit), *FOXP1* (forkhead box P1), *FOXP4* (forkhead box P4), *KLF4* (KLF transcription factor 4), and *ELF3* [128]. Own and published results demonstrate a strong molecular difference between classical and basal-like cell lines, and highlight that these differences are epigenetically regulated. This suggests a potential application of epigenetic drug treatment strategies, particularly in the context of personalized treatment for different molecular PDAC subtypes.

EMT is a unique characteristic of aggressive tumor cells that enables them to acquire migratory and invasive capabilities, which are processes that rely on cytoskeletal reorganization. The cytoskeleton is composed of three key components: microtubules, intermediate filaments, and actin filaments [129]. In this project, GO term analysis was performed on the DEGs of classical and basal-like cell lines, revealing significant enrichment in processes related to actin cytoskeleton organization, underscoring the crucial role of actin filament reorganization in these two subtypes. This finding was further investigated by F-actin staining using phalloidin conjugates and it could be demonstrated that F-actin was predominantly located at the cell membrane in classical cell lines, while in basal-like cell lines, F-actin was dispersed throughout the cytoplasm. These observations align with findings that epithelial cells typically possess cortical actin rings [130, 131], while metastatic mesenchymal cells exhibit an increase in actin stress fibers [132]. Thus, in mouse mammary epithelial NMuMG cells, TGF-β has been shown to transform thin cortical bundles into thick stress fibers, an effect that can be inhibited by the ROCK inhibitor Y-27632 [133]. The TGF-β-driven remodeling of the actin cytoskeleton in mouse mammary epithelial NMuMG cells and the acquisition of mesenchymal characteristics was regulated by RhoA/ROCK signaling [134]. Such changes are crucial for morphological and functional transitions of EMT characteristics. Specifically, the activation of the RhoA/ROCK signaling plays a key role in promoting the formation of stress fibers, which contribute to the acquisition of mesenchymal traits.

These alterations support the aggressive phenotype of the tumor cells that is commonly associated with a basal-like subtype.

TGF-β signaling is a key regulator of the EMT process and often cross-talks with the Rho-GTPase signaling, which in turn is a critical regulator of the actin cytoskeleton [135, 136]. Therefore, DEGs of Rho-GTPase signaling components in classical and basal-like cell lines were analyzed. Contrary to expectations, no differential expression was observed for the typical Rho-GTPase members *RAC1*, *RHOA*, and *CDC42* between classical and basal-like cell lines. However, this can be explained by the fact that *RAC1*, *RHOA,* and *CDC42* are crucial regulators of the cytoskeleton organization and maintain cell morphology in general. Therefore, their baseline expression and function are necessary in both classical and basal-like cells. While their presence is essential, the activity of Rho-GTPases deserves further investigation in classical and basal-like cell lines [137]. In the present study, it was identified that components of the Rho-GTPase signaling are generally lower expressed in basal-like cell lines compared to classical cell lines and basal-like cell lines exhibited a more pronounced downregulation of Rho-GTPase inhibitors, such as GAPs, GDIs, and of members of the atypical Rho-GTPases subfamily. This result further explains that the regulation of Rho-GTPase pathway components plays an important role in classical and basal-like cell lines. In particular, the extensive downregulation of Rho-GAPs, Rho-GDIs and atypical Rho-GTPases in basal-like cell lines may contribute to an activation of the canonical Rho-GTPase pathway. Studies by Yeung et al. showed that the expression of recombinant Arhgap28-V5, a Rho-GAP, in human osteosarcoma SaOS-2 cells resulted in decreased levels of RhoA activation and a disruption of actin stress fibers [138]. Rnd is an atypical Rho-GTPase that can compete with RhoA for binding to the Rho-binding domain (RBD) of ROCK, thereby inhibiting ROCK-induced stress fiber formation [139, 140]. Moreover, the findings from Qin et al. showed that SAHA-mediated inhibition of HDAC enhanced the expression of *RND1* (Rho family GTPase 1), which leads to the suppression of the RhoA/Raf/MEK/ERK signaling pathway, thereby inhibiting EMT-mediated metastasis in hepatocellular carcinoma [141]. In the present study, a decrease in the gene expression of the Rho-GTPase pathway inhibitors *ARHGAP18* and *ARHGDIB* was detected in basal-like PDAC cell lines compared to the classical subtype. In addition, low levels of H3K27ac were detected at the promoter of *ARHGAP18* in basal-like cell lines, whereas classical cell lines showed an enrichment of H3K27ac at the gene promoter. This project is the first to report that *ARHGAP18* is differentially expressed in classical and basal-like cell lines under epigenetic regulation. According to a study conducted by Maeda et al., overexpression of *ARHGAP18* inhibits RhoA activity, disrupts the formation of stress fibers in HeLa cells, and suppresses cell migration [142]. This suggests that alterations

in *ARHGAP18* gene expression could significantly influence cytoskeletal dynamics through the RhoA/ROCK signaling and contribute to the mesenchymal characteristics observed in basal-like cell lines. These findings suggest that the Rho-GTPase signaling pathway, along with its regulators and effectors, may serve as potential therapeutic target for EMT-related malignancies, particularly in the treatment of basal-like cell lines.

RhoA/ROCK signaling is a proven key regulator of stress fiber and crosstalk with TGF-β signaling to induce EMT process in tumor cells [133, 134]. The protein expression of RhoA and ROCK2 was further examined in both classical and basal-like PDAC cell lines, and no differences were observed in their overall expression. This result aligns with the assessed transcriptome profiles, which showed a similar *RhoA* expression in classical and basal-like cell lines. Since ROCK2 typically binds to activated RhoA to exert its function [106-108], it is probable that their activity, rather than their expression levels, plays a crucial role in their involvement in cytoskeletal organization in classical and basal-like cell lines. Interestingly, an increased trend in the presence of cleaved-ROCK2 was noted in basal-like PDAC cell lines. While many studies have observed the existence of cleaved-ROCK2, the specific differences in function between the RhoA-bound ROCK2 and cleaved-ROCK2 are still not well understood. It has been shown by Leung et al. that ROCK2, when lacking the C-terminal RBD-PH domain, significantly influences the formation of stress fibers and focal adhesion complexes [107]. Furthermore, the findings from Amano et al. indicate that this truncated version of ROCK2 acts as a constitutively active form, enhancing cell contraction in neurons like that of the full-length activated ROCK2 [143]. These insights suggest that cleaved-ROCK2 could play a crucial role in cytoskeleton rearrangements and adhesion properties, particularly in basal-like PDAC cell lines. Given the potential importance of subcellular localization in determining protein function, the localization of RhoA and ROCK2 in PDAC cell lines was investigated using different experimental approaches. Through immunoblot analysis of cytoplasmic and nuclear-extracted proteins, RhoA was found to be exclusively localized in the cytoplasm, whereas ROCK2 was detected in both the nucleus and cytoplasm. Notably, cleaved-ROCK2 was specifically observed in the nucleus. In contrast, immunofluorescence staining demonstrated the presence of both RhoA and ROCK2 in the cytoplasm and nucleus across six PDAC cell lines, suggesting strong consistency of RhoA and ROCK2 in subcellular distribution. This variation may be attributed to the differing sensitivities and specificities of the experimental methods used.

According to immunofluorescence staining results that are offered by The Human Protein Atlas website, RhoA has been predominantly found in the cytoplasm in different cell lines such as A-431, U-251MG, and U2OS [144]. Similarly, ROCK2 has also been observed

in the cytoplasm in HeLa and Hep-G2 cell lines [145]. However, work from Dubash et al. and Tanaka et al., which used cytoplasmic and nuclear-extracted proteins followed by immunoblot analysis, revealed that both RhoA and ROCK2 were found in the cytoplasm and nucleus of HEK293, HeLa, and several other cell lines [146, 147]. Interestingly, some studies have identified less common locations for RhoA, such as its presence in the nucleolus of gastric cancer AGS cell lines and epithelial tumor-derived HEp-2 cell lines. For instance, RhoA has been found to co-localize with NF-κB in AGS cell lines and to participate in processes such as RNA synthesis in HEp-2 cells [148, 149]. Consistent with these findings, the present study exhibited that basal-like PDAC cell lines possess larger and more numerous nucleoli, along with increased localization of RhoA and ROCK2 in the nucleoli, compared to classical cell lines. These observations underscore the potential significance of the nuclear localization of RhoA and ROCK2, suggesting that their roles in the nucleus may be more critical than previously understood, particularly in the context of tumor development.

The nuclear localization of RhoA and ROCK2 suggests its role in regulating gene expression, particularly with ROCK2 as a kinase that plays a role in phosphorylation. Therefore, it was hypothesized that ROCK2 may phosphorylate HDAC2 in the nucleus to activate it, leading to a loss of H3K27ac and epigenetic silencing of classical marker genes such as *ELF3* or the Rho-GTPase inhibitor *ARHGAP18*. To test this hypothesis, classical and basal-like cells were treated with the ROCK inhibitor Y-27632. However, no differences in ROCK2 and RhoA protein expression were observed following treatment with Y-27632, and no changes in HDAC2 phosphorylation were detected. Additionally, immunofluorescence staining of phalloidin conjugates revealed that the cytoskeleton of both the classical cell line Capan-1 and the basal-like cell line PANC-1 was not affected by Y-27632 treatment. This lack of effect could be due to an inappropriate duration or concentration of ROCK inhibitor treatment, as well as varying responses to the inhibitor across different cell lines. In the study of Stricker et al., human osteosarcoma U2OS cells were incubated with different concentrations (1-10 µM) of the ROCK inhibitor Y-27632 for 1 hour, followed by F-actin staining. At low concentrations (2 µM) of the Y-27632, transverse arcs and radial stress fibers were still observed. As the concentration increased to 5 µM, a significant reduction in radial stress fibers was significantly reduced. At the highest concentration (10 µM), transverse arcs, radial stress fibers and lamellar actin bundles completely disappeared [150]. However, osteosarcoma cells, with strong mesenchymal signature, have a more abundant presence of actin filaments compared to epithelial cells and may therefore be more sensitive to treatment with the ROCK inhibitor Y-27632. In PC-12 pheochromocytoma cell line, treatment with

25 µM ROCK inhibitor Y-27632 for 5 minutes, 30 minutes, 2 hours, 6 hours, 12 hours, and 24 hours was followed by measurement of the phosphorylation level of the ROCK effector cofilin. The results showed a downward trend in cofilin phosphorylation from 5 minutes to 2 hours, with levels returning to the untreated state after 2 hours [151]. Therefore, determining the appropriate duration and concentration of ROCK inhibitor Y-27632 treatment is crucial.

As discussed above, the gene expression of the classical marker *ELF3*, the basal-like marker *VIM*, and the Rho-GTPase inhibitor *ARHGAP18* are all regulated by histone acetylation. However, whether changes in epigenetic regulation is dependent on the molecular subtype of the cancer has not been fully elucidated. To address this, it was investigated whether the overall histone acetylation status and the expression of histone-modifying enzymes differ between classical and basal-like PDAC cells. Here, a significant increase in the expression of HDAC2 and phosphorylated HDAC2 (p-HDAC2) was observed in basal-like cell lines, alongside a decrease in overall H3K27ac abundance and lower expression levels of the histone acetyltransferase (HAT) genes *EP300* and *CREBBP*. These findings suggest that HDAC2 may serve as a key epigenetic regulator in basal-like cell lines, with p-HDAC2 potentially repressing genes related to the Rho-GTPase pathway through epigenetic mechanisms. This conclusion aligns with results from other studies. For instance, interactions between HDAC1 and HDAC2 with EMT transcription factors such as *SNAIL* and *ZEB1* have been reported, leading to the silencing of the epithelial marker E-cadherin (*CDH1*) and the promotion of tumor progression toward an invasive EMT phenotype [152, 153]. Furthermore, a study by Krauss et al. demonstrated that increased *HDAC2* expression in basal-like PDAC cell lines is associated with an invasive and metastatic gene expression profile [66]. Additionally, the critical role of HDAC2 phosphorylation at the S394 site in regulating its activity was highlighted by Tsai et al. [154], while Sun et al. further demonstrated that HDAC2 phosphorylation is essential for the formation of the Sin3 and NuRD complexes and their enrichment at gene promoters [155]. Notably, the significant nuclear localization of RhoA and ROCK2 in basal-like cell lines, particularly their localization in the nucleolus, suggests that these molecules may have specific nuclear functions. Tanaka et al.'s study demonstrated that nuclear ROCK2 can phosphorylate the HAT p300 [147]. Additionally, Pietrzak et al. provided key insights into the differential roles of p300 and HDAC1 in monocytes and macrophages, showing that p300 and HDAC1 interact with the SWI/SNF complex but with distinct effects: in monocytes, HDAC1 represses gene expression through deacetylation, while in macrophages, p300 enhances gene expression through acetylation [156]. This suggests that the functions of p300 and HDAC2 may be highly

dynamic and context-dependent across different cell types. However, in the present study it was not delineated whether the high levels of HDAC2 phosphorylation are because of overall high expression levels of HDAC2 in basal-like cell lines.

A comprehensive understanding of the impact of epigenetic acetylation on the transcriptome profiles of classical and basal-like cell lines is crucial for determining whether epigenetic acetylation influences the transition between tumor subtypes. To explore this, all seven PDAC cell lines were treated with the histone acetyltransferase inhibitor (HATi) A485 and the histone deacetylase inhibitor (HDACi) SAHA, both in short-term (24 hours) and long-term treatments. Overall, classical and basal-like cells exhibited high concordance in their response to both short-term and long-term epigenetic drug treatments, with both subtypes responding poorly to HDACi treatment. Basal-like cell lines, in particular, showed weak responses to both HATi and HDACi. At least, A485-treated PDAC cell lines displayed a decent amount of downregulated genes after short-term treatment, while the number of differentially expressed genes following SAHA treatment was very low. Long-term A485 treatment significantly reduced H3K27ac levels in both classical and basal-like cell lines, whereas long-term SAHA treatment did not result in significant H3K27ac enrichment. Notably, after extended exposure to A485, a significant decrease in H3K27ac at the *ELF3* promoter and an increase at the *VIM* promoter were observed in classical cell lines, accompanied by a corresponding decrease in *ELF3* expression and an increase in *VIM* expression. In contrast, no similar changes were observed in basal-like cell lines. The insensitivity of basal-like cell lines to epigenetic drug treatment may be attributed to the fact that the number of enhancers affected by epigenetic acetylation in basal-like cells is far fewer than in classical cell lines, as previous studies described. For instance, Lomberk et al. identified 250 histone acetylation positive super enhancers (SEs) in classical PDAC cell lines, whereas only 30 SEs were found in basal-like cell lines [128]. Similarly, Diaferia et al. reported that low-grade cell lines with epithelial characteristics, which are classical cell lines, contained 50 SEs, while high-grade cell lines with mesenchymal characteristics had only 12 SEs [33]. This might also explain why basal-like cell lines showed only a slight increase in H3K27ac at the promoter and a modest increase in the expression of the Rho-GTPase inhibitor *ARHGAP18* after HDACi treatment.

Both short-term and long-term treatments with the HAT inhibitor A485 had adverse effects on classical PDAC cell lines, promoting extensive EMT characteristics. Short-term treatment led to an increase in the EMT score, while long-term A485 treatment resulted in the downregulation of the epithelial marker gene *ELF3* and upregulation of the mesenchymal marker gene *VIM*. These changes were associated with alterations in H3K27ac levels at their promoter regions, along with enhanced clonogenicity and

migratory properties. High doses of HAT inhibitors combined with gemcitabine have been shown to completely suppress histone acetylation, leading to cell cycle arrest and apoptosis in pancreatic tumor cells [50, 157]. However, these effects are largely due to drug synergy or additive effects, highlighting the importance of carefully assessing HAT inhibitor dosage in chemotherapy, particularly for PDAC patients with a classical tumor subtype. Despite reports of HDAC-driven tumor progression predominantly in basal-like PDAC, treatment of both subtypes with HDAC inhibitors revealed minimal effects. Increases in H3K27ac were observed in basal-like cell lines, but changes in gene expression were minor, and long-term treatment with the HDAC inhibitor SAHA did not significantly alter *ELF3* or *VIM* expression. While there was a slight increase in the expression of the RhoA inhibition factor *ARHGAP18* and H3K27ac enrichment at its promoter in basal-like cells, these changes were not statistically significant. Only classical cell lines exhibited a reduction in cell proliferation after prolonged HDACi treatment. Although low-dose SAHA treatment produced varied responses across different PDAC subtypes [158-160], the overall impact of HDAC inhibitors on EMT remains controversial. Some studies suggest that HDAC inhibitors like Trichostatin A (TSA) can inhibit metastasis [161], while others report that pan-HDAC inhibitors like SAHA may induce a mesenchymal phenotype in various cancers, including lung, colorectal cancer and prostate cancers [162-164]. Given the increase in HDAC expression in many cancer types, HDAC inhibitors show potential as chemotherapy agents. However, their effectiveness and therapeutic outcomes are highly dependent on factors such as cellular subtype, dosage, and targeted HDAC categories. Although HDAC inhibitors have been explored as potential therapies for PDAC, either as monotherapy or in combination with other treatments [165, 166], further comprehensive investigations are necessary. Future research should focus on preselecting patients who are most likely to respond to epigenetic therapy, ensuring that targeted epigenetic modifications are applied to those who will benefit the most.

This study has several limitations. One of the most important unanswered questions is whether there are differences in RhoA activation between classical and basal-like cell lines, which is essential for future research. Additionally, the exact effect of ROCK2 on HDAC2 phosphorylation remains unclear. To address this, future studies should use ROCK2-specific inhibitors, such as Belumosudil (KD025), and optimize the treatment duration. The effectiveness of ROCK2-specific inhibitors should also be assessed by measuring phosphorylated MLC and phosphorylated Cofilin, which are involved in ROCK2 activation. After determining the optimal treatment time and concentration of ROCK2 inhibitors, it will be crucial to measure histone acetylation and expression of the classical marker *ELF3*, the basal-like marker *VIM*, and the Rho-GTPase inhibitor

ARHGAP18. Furthermore, the current results do not clearly clarify the form of ROCK2 present in the nucleus (whether it is RhoA-bound ROCK2 or cleaved-ROCK2) or how it functions there. In addition, there were significant disparities observed in the arrangement of the actin cytoskeleton between classical and basal-like cell lines. This difference is not only attributed to RhoA/ROCK signaling regulation of stress fibers, but is also potentially influenced by the interaction between lamellipodia, regulated by RAC1, and filopodia, regulated by CDC42. Therefore, a comprehensive study of typical Rho-GTPases in classical and basal-like cell lines will be essential for better understanding the switch between PDAC subtypes. Since SAHA is a pan-HDAC inhibitor, its broad application limits the ability to draw specific conclusions. Utilizing more precise HDAC2 inhibitors, such as Santacruzamate A, may provide insights into the role of HDAC2 in classical and basal-like PDAC and its potential impact on the acetylation and expression of *ARHGAP18*.

References

[1] F. N. van Erning *et al.*, "Association of the location of pancreatic ductal adenocarcinoma (head, body, tail) with tumor stage, treatment, and survival: a population-based analysis," (in eng), *Acta Oncol,* vol. 57, no. 12, pp. 1655-1662, Dec 2018.

[2] A. McGuigan, P. Kelly, R. C. Turkington, C. Jones, H. G. Coleman, and R. S. McCain, "Pancreatic cancer: A review of clinical diagnosis, epidemiology, treatment and outcomes," (in eng), *World J Gastroenterol,* vol. 24, no. 43, pp. 4846-4861, Nov 21 2018.

[3] N. C. I. (U.S.). (Accessed June 20, 2024). *Cancer Stat Facts: Pancreatic Cancer, 2024*. Available: https://seer.cancer.gov/statfacts/html/pancreas.html

[4] G. Carioli *et al.*, "European cancer mortality predictions for the year 2021 with focus on pancreatic and female lung cancer," (in eng), *Ann Oncol,* vol. 32, no. 4, pp. 478-487, Apr 2021.

[5] J. P. Neoptolemos, J. Kleeff, P. Michl, E. Costello, W. Greenhalf, and D. H. Palmer, "Therapeutic developments in pancreatic cancer: current and future perspectives," (in eng), *Nat Rev Gastroenterol Hepatol,* vol. 15, no. 6, pp. 333-348, Jun 2018.

[6] J. Koopmann *et al.*, "Serum macrophage inhibitory cytokine 1 as a marker of pancreatic and other periampullary cancers," (in eng), *Clin Cancer Res,* vol. 10, no. 7, pp. 2386-92, Apr 1 2004.

[7] U. K. Ballehaninna and R. S. Chamberlain, "The clinical utility of serum CA 19-9 in the diagnosis, prognosis and management of pancreatic adenocarcinoma: An evidence based appraisal," (in eng), *J Gastrointest Oncol,* vol. 3, no. 2, pp. 105-19, Jun 2012.

[8] M. J. Amaral, R. C. Oliveira, P. Donato, and J. G. Tralhão, "Pancreatic Cancer Biomarkers: Oncogenic Mutations, Tissue and Liquid Biopsies, and Radiomics-A Review," (in eng), *Dig Dis Sci,* vol. 68, no. 7, pp. 2811-2823, Jul 2023.

[9] E. S. Lee and J. M. Lee, "Imaging diagnosis of pancreatic cancer: a state-of-the-art review," (in eng), *World J Gastroenterol,* vol. 20, no. 24, pp. 7864-77, Jun 28 2014.

[10] J. Kleeff *et al.*, "Pancreatic cancer," (in eng), *Nat Rev Dis Primers,* vol. 2, p. 16022, Apr 21 2016.

[11] A. Pappalardo *et al.*, "Adjuvant Treatment in Pancreatic Cancer: Shaping the Future of the Curative Setting," (in eng), *Front Oncol,* vol. 11, p. 695627, 2021.

[12] K. E. Volmar, R. T. Vollmer, P. S. Jowell, R. C. Nelson, and H. B. Xie, "Pancreatic FNA in 1000 cases: a comparison of imaging modalities," (in eng), *Gastrointest Endosc,* vol. 61, no. 7, pp. 854-61, Jun 2005.

[13] D. D. Brennan, G. A. Zamboni, V. D. Raptopoulos, and J. B. Kruskal, "Comprehensive preoperative assessment of pancreatic adenocarcinoma with 64-section volumetric CT," (in eng), *Radiographics,* vol. 27, no. 6, pp. 1653-66, Nov-Dec 2007.

[14] A. Arnone *et al.*, "Clinical Impact of (18)F-FDG PET/CT in the Diagnostic Workup of Pancreatic Ductal Adenocarcinoma: A Systematic Review," (in eng), *Diagnostics (Basel),* vol. 10, no. 12, Dec 3 2020.

[15] M. K. Kalra, M. M. Maher, P. R. Mueller, and S. Saini, "State-of-the-art imaging of pancreatic neoplasms," (in eng), *Br J Radiol,* vol. 76, no. 912, pp. 857-65, Dec 2003.

[16] S. Schorn *et al.*, "The impact of neoadjuvant therapy on the histopathological features of pancreatic ductal adenocarcinoma - A systematic review and meta-analysis," (in eng), *Cancer Treat Rev,* vol. 55, pp. 96-106, Apr 2017.

[17] D. R. Principe, P. W. Underwood, M. Korc, J. G. Trevino, H. G. Munshi, and A. Rana, "The Current Treatment Paradigm for Pancreatic Ductal Adenocarcinoma and Barriers to Therapeutic Efficacy," (in eng), *Front Oncol,* vol. 11, p. 688377, 2021.

[18] N. C. Institute. (2024, July 18, 2024). *Pancreatic Cancer Treatment (PDQ®)–Health Professional Version*. Available: https://www.cancer.gov/types/pancreatic/hp/pancreatic-treatment-pdq

[19] A. Kowalewski, Ł. Szylberg, M. Saganek, W. Napiontek, P. Antosik, and D. Grzanka, "Emerging strategies in BRCA-positive pancreatic cancer," (in eng), *J Cancer Res Clin Oncol,* vol. 144, no. 8, pp. 1503-1507, Aug 2018.

[20] M. J. Pishvaian, I. Garrido-Laguna, S. V. Liu, P. S. Multani, E. Chow-Maneval, and C. Rolfo, "Entrectinib in TRK and ROS1 Fusion-Positive Metastatic Pancreatic Cancer," (in eng), *JCO Precis Oncol,* vol. 2, pp. 1-7, Nov 2018.

[21] L. Zhao, V. Singh, A. Ricca, and P. Lee, "Survival Benefit of Pembrolizumab for Patients With Pancreatic Adenocarcinoma: A Case Series," (in eng), *J Med Cases,* vol. 13, no. 5, pp. 240-243, May 2022.

[22] D. R. Principe, "Precision Medicine for BRCA/PALB2-Mutated Pancreatic Cancer and Emerging Strategies to Improve Therapeutic Responses to PARP Inhibition," (in eng), *Cancers (Basel),* vol. 14, no. 4, Feb 11 2022.

[23] D. B. Zhen, R. A. Safyan, E. Q. Konick, R. Nguyen, C. C. Prichard, and E. G. Chiorean, "The role of molecular testing in pancreatic cancer," (in eng), *Therap Adv Gastroenterol,* vol. 16, p. 17562848231171456, 2023.

[24] J. L. Humphris *et al.*, "Hypermutation In Pancreatic Cancer," (in eng), *Gastroenterology,* vol. 152, no. 1, pp. 68-74.e2, Jan 2017.

[25] E. A. Collisson *et al.*, "Subtypes of pancreatic ductal adenocarcinoma and their differing responses to therapy," (in eng), *Nat Med,* vol. 17, no. 4, pp. 500-3, Apr 2011.

[26] R. A. Moffitt *et al.*, "Virtual microdissection identifies distinct tumor- and stroma-specific subtypes of pancreatic ductal adenocarcinoma," (in eng), *Nat Genet,* vol. 47, no. 10, pp. 1168-78, Oct 2015.

[27] P. Bailey *et al.*, "Genomic analyses identify molecular subtypes of pancreatic cancer," (in eng), *Nature,* vol. 531, no. 7592, pp. 47-52, Mar 3 2016.

[28] F. Puleo *et al.*, "Stratification of Pancreatic Ductal Adenocarcinomas Based on Tumor and Microenvironment Features," (in eng), *Gastroenterology,* vol. 155, no. 6, pp. 1999-2013.e3, Dec 2018.

[29] F. Dijk *et al.*, "Unsupervised class discovery in pancreatic ductal adenocarcinoma reveals cell-intrinsic mesenchymal features and high concordance between existing classification systems," (in eng), *Sci Rep,* vol. 10, no. 1, p. 337, Jan 15 2020.

[30] M. Chan-Seng-Yue *et al.*, "Transcription phenotypes of pancreatic cancer are driven by genomic events during tumor evolution," (in eng), *Nat Genet,* vol. 52, no. 2, pp. 231-240, Feb 2020.

[31] A. Hayashi *et al.*, "A unifying paradigm for transcriptional heterogeneity and squamous features in pancreatic ductal adenocarcinoma," (in eng), *Nat Cancer,* vol. 1, no. 1, pp. 59-74, Jan 2020.

[32] N. Juiz *et al.*, "Basal-like and classical cells coexist in pancreatic cancer revealed by single-cell analysis on biopsy-derived pancreatic cancer organoids from the classical subtype," (in eng), *Faseb j,* vol. 34, no. 9, pp. 12214-12228, Sep 2020.

[33] G. R. Diaferia *et al.*, "Dissection of transcriptional and cis-regulatory control of differentiation in human pancreatic cancer," (in eng), *Embo j,* vol. 35, no. 6, pp. 595-617, Mar 15 2016.

[34] J. A. Alberts B, Lewis J, et al., *Chromosomal DNA and Its Packaging in the Chromatin Fiber* (Molecular Biology of the Cell). New York: Garland Science, 2002.

[35] T. Kouzarides, "Chromatin modifications and their function," (in eng), *Cell,* vol. 128, no. 4, pp. 693-705, Feb 23 2007.

[36] C. L. Liu *et al.*, "Single-nucleosome mapping of histone modifications in S. cerevisiae," (in eng), *PLoS Biol,* vol. 3, no. 10, p. e328, Oct 2005.

[37] A. Barski *et al.*, "High-resolution profiling of histone methylations in the human genome," (in eng), *Cell,* vol. 129, no. 4, pp. 823-37, May 18 2007.

[38] Z. Wang *et al.*, "Combinatorial patterns of histone acetylations and methylations in the human genome," (in eng), *Nat Genet,* vol. 40, no. 7, pp. 897-903, Jul 2008.

[39] S. G. Smith and M. M. Zhou, "The Bromodomain: A New Target in Emerging Epigenetic Medicine," (in eng), *ACS Chem Biol,* vol. 11, no. 3, pp. 598-608, Mar 18 2016.

[40] C. Ghosh *et al.*, "Super-enhancers: novel target for pancreatic ductal adenocarcinoma," (in eng), *Oncotarget,* vol. 10, no. 16, pp. 1554-1571, Feb 22 2019.

[41] O. G. McDonald *et al.*, "Epigenomic reprogramming during pancreatic cancer progression links anabolic glucose metabolism to distant metastasis," (in eng), *Nat Genet,* vol. 49, no. 3, pp. 367-376, Mar 2017.

[42] D. E. Sterner and S. L. Berger, "Acetylation of histones and transcription-related factors," (in eng), *Microbiol Mol Biol Rev,* vol. 64, no. 2, pp. 435-59, Jun 2000.

[43] C. E. Berndsen and J. M. Denu, "Catalysis and substrate selection by histone/protein lysine acetyltransferases," (in eng), *Curr Opin Struct Biol,* vol. 18, no. 6, pp. 682-9, Dec 2008.

[44] Q. Jin *et al.*, "Distinct roles of GCN5/PCAF-mediated H3K9ac and CBP/p300-mediated H3K18/27ac in nuclear receptor transactivation," (in eng), *Embo j,* vol. 30, no. 2, pp. 249-62, Jan 19 2011.

[45] M. Kishimoto *et al.*, "Mutations and deletions of the CBP gene in human lung cancer," (in eng), *Clin Cancer Res,* vol. 11, no. 2 Pt 1, pp. 512-9, Jan 15 2005.

[46] G. Zhu, L. Pei, Y. Li, and X. Gou, "EP300 mutation is associated with tumor mutation burden and promotes antitumor immunity in bladder cancer patients," (in eng), *Aging (Albany NY),* vol. 12, no. 3, pp. 2132-2141, Feb 3 2020.

[47] M. Luo, Y. Zhang, Z. Xu, S. Lv, Q. Wei, and Q. Dang, "Experimental analysis of bladder cancer-associated mutations in EP300 identifies EP300-R1627W as a driver mutation," (in eng), *Mol Med,* vol. 29, no. 1, p. 7, Jan 16 2023.

[48] F. H. Tsang *et al.*, "Aberrant Super-Enhancer Landscape in Human Hepatocellular Carcinoma," (in eng), *Hepatology,* vol. 69, no. 6, pp. 2502-2517, Jun 2019.

[49] J. Welti *et al.*, "Targeting the p300/CBP Axis in Lethal Prostate Cancer," (in eng), *Cancer Discov,* vol. 11, no. 5, pp. 1118-1137, May 2021.

[50] H. Ono, M. D. Basson, and H. Ito, "P300 inhibition enhances gemcitabine-induced apoptosis of pancreatic cancer," (in eng), *Oncotarget,* vol. 7, no. 32, pp. 51301-51310, Aug 9 2016.

[51] S. T. Mees *et al.*, "EP300--a miRNA-regulated metastasis suppressor gene in ductal adenocarcinomas of the pancreas," (in eng), *Int J Cancer,* vol. 126, no. 1, pp. 114-24, Jan 1 2010.

[52] Z. Zhong, N. Harmston, K. C. Wood, B. Madan, and D. M. Virshup, "A p300/GATA6 axis determines differentiation and Wnt dependency in pancreatic cancer models," (in eng), *J Clin Invest,* vol. 132, no. 12, Jun 15 2022.

[53] D. L. Gerrard, J. R. Boyd, G. S. Stein, V. X. Jin, and S. Frietze, "Disruption of Broad Epigenetic Domains in PDAC Cells by HAT Inhibitors," (in eng), *Epigenomes,* vol. 3, no. 2, Jun 2019.

[54] A. D. Bondarev, M. M. Attwood, J. Jonsson, V. N. Chubarev, V. V. Tarasov, and H. B. Schiöth, "Recent developments of HDAC inhibitors: Emerging indications and novel molecules," (in eng), *Br J Clin Pharmacol,* vol. 87, no. 12, pp. 4577-4597, Dec 2021.

[55] A. Ko *et al.*, "Final results of a phase Ib dose-escalation study of PRI-724, a CBP/beta-catenin modulator, plus gemcitabine (GEM) in patients with advanced pancreatic adenocarcinoma (APC) as second-line therapy after FOLFIRINOX or FOLFOX," *Journal of Clinical Oncology,* vol. 34, pp. e15721-e15721, 05/20 2016.

[56] A. J. de Ruijter, A. H. van Gennip, H. N. Caron, S. Kemp, and A. B. van Kuilenburg, "Histone deacetylases (HDACs): characterization of the classical HDAC family," (in eng), *Biochem J,* vol. 370, no. Pt 3, pp. 737-49, Mar 15 2003.

[57] N. J. Porter and D. W. Christianson, "Structure, mechanism, and inhibition of the zinc-dependent histone deacetylases," (in eng), *Curr Opin Struct Biol,* vol. 59, pp. 9-18, Dec 2019.

[58] A. Vaquero, R. Sternglanz, and D. Reinberg, "NAD+-dependent deacetylation of H4 lysine 16 by class III HDACs," (in eng), *Oncogene,* vol. 26, no. 37, pp. 5505-20, Aug 13 2007.

[59] S. Y. Park and J. S. Kim, "A short guide to histone deacetylases including recent progress on class II enzymes," (in eng), *Exp Mol Med,* vol. 52, no. 2, pp. 204-212, Feb 2020.

[60] H. Yang, T. Salz, M. Zajac-Kaye, D. Liao, S. Huang, and Y. Qiu, "Overexpression of histone deacetylases in cancer cells is controlled by interplay of transcription factors and epigenetic modulators," (in eng), *Faseb j,* vol. 28, no. 10, pp. 4265-79, Oct 2014.

[61] S. Li *et al.*, "HDAC2 regulates cell proliferation, cell cycle progression and cell apoptosis in esophageal squamous cell carcinoma EC9706 cells," (in eng), *Oncol Lett,* vol. 13, no. 1, pp. 403-409, Jan 2017.

[62] J. H. Noh *et al.*, "Aberrant regulation of HDAC2 mediates proliferation of hepatocellular carcinoma cells by deregulating expression of G1/S cell cycle proteins," (in eng), *PLoS One,* vol. 6, no. 11, p. e28103, 2011.

[63] S. Jamaladdin *et al.*, "Histone deacetylase (HDAC) 1 and 2 are essential for accurate cell division and the pluripotency of embryonic stem cells," (in eng), *Proc Natl Acad Sci U S A,* vol. 111, no. 27, pp. 9840-5, Jul 8 2014.

[64] S. X. Cai, W. S. Chen, W. Zeng, X. F. Cheng, M. B. Lin, and J. S. Wang, "Roles of HDAC2, eIF5, and eIF6 in Lung Cancer Tumorigenesis," (in eng), *Curr Med Sci,* vol. 41, no. 4, pp. 764-769, Aug 2021.

[65] Y. Stypula-Cyrus *et al.*, "HDAC up-regulation in early colon field carcinogenesis is involved in cell tumorigenicity through regulation of chromatin structure," (in eng), *PLoS One,* vol. 8, no. 5, p. e64600, 2013.

[66] L. Krauß *et al.*, "HDAC2 Facilitates Pancreatic Cancer Metastasis," (in eng), *Cancer Res,* vol. 82, no. 4, pp. 695-707, Feb 15 2022.

[67] Z. P. Qi *et al.*, "HDAC2 promotes the EMT of colorectal cancer cells and via the modular scaffold function of ENSG00000274093.1," (in eng), *J Cell Mol Med,* vol. 25, no. 2, pp. 1190-1197, Jan 2021.

[68] L. Li, D. T. Mei, and Y. Zeng, "HDAC2 promotes the migration and invasion of non-small cell lung cancer cells via upregulation of fibronectin," (in eng), *Biomed Pharmacother,* vol. 84, pp. 284-290, Dec 2016.

[69] C. D. Laherty, W. M. Yang, J. M. Sun, J. R. Davie, E. Seto, and R. N. Eisenman, "Histone deacetylases associated with the mSin3 corepressor mediate mad transcriptional repression," (in eng), *Cell,* vol. 89, no. 3, pp. 349-56, May 2 1997.

[70] A. You, J. K. Tong, C. M. Grozinger, and S. L. Schreiber, "CoREST is an integral component of the CoREST- human histone deacetylase complex," (in eng), *Proc Natl Acad Sci U S A,* vol. 98, no. 4, pp. 1454-8, Feb 13 2001.

[71] Y. Zhang, H. H. Ng, H. Erdjument-Bromage, P. Tempst, A. Bird, and D. Reinberg, "Analysis of the NuRD subunits reveals a histone deacetylase core complex and a connection with DNA methylation," (in eng), *Genes Dev,* vol. 13, no. 15, pp. 1924-35, Aug 1 1999.

[72] R. E. Turnbull *et al.*, "The MiDAC histone deacetylase complex is essential for embryonic development and has a unique multivalent structure," (in eng), *Nat Commun,* vol. 11, no. 1, p. 3252, Jun 26 2020.

[73] A. Lehmann *et al.*, "High class I HDAC activity and expression are associated with RelA/p65 activation in pancreatic cancer in vitro and in vivo," *BMC Cancer,* vol. 9, p. 395, Nov 13 2009.

[74] P. Fritsche *et al.*, "HDAC2 mediates therapeutic resistance of pancreatic cancer cells via the BH3-only protein NOXA," *Gut,* vol. 58, no. 10, pp. 1399-409, Oct 2009.

[75] S. Schüler *et al.*, "HDAC2 attenuates TRAIL-induced apoptosis of pancreatic cancer cells," (in eng), *Mol Cancer,* vol. 9, p. 80, Apr 16 2010.

[76] Y. Li and E. Seto, "HDACs and HDAC Inhibitors in Cancer Development and Therapy," (in eng), *Cold Spring Harb Perspect Med,* vol. 6, no. 10, Oct 3 2016.

[77] I. Koutsounas, C. Giaginis, and S. Theocharis, "Histone deacetylase inhibitors and pancreatic cancer: are there any promising clinical trials?," (in eng), *World J Gastroenterol,* vol. 19, no. 8, pp. 1173-81, Feb 28 2013.

[78] A. Bulle and K. H. Lim, "Beyond just a tight fortress: contribution of stroma to epithelial-mesenchymal transition in pancreatic cancer," (in eng), *Signal Transduct Target Ther,* vol. 5, no. 1, p. 249, Oct 30 2020.

[79] J. P. Thiery, H. Acloque, R. Y. Huang, and M. A. Nieto, "Epithelial-mesenchymal transitions in development and disease," (in eng), *Cell,* vol. 139, no. 5, pp. 871-90, Nov 25 2009.

[80] G. Hamilton and B. Rath, "Mesenchymal-Epithelial Transition and Circulating Tumor Cells in Small Cell Lung Cancer," (in eng), *Adv Exp Med Biol,* vol. 994, pp. 229-245, 2017.

[81] R. Kalluri and R. A. Weinberg, "The basics of epithelial-mesenchymal transition," (in eng), *J Clin Invest,* vol. 119, no. 6, pp. 1420-8, Jun 2009.

[82] S. Y. Cho *et al.*, "High prevalence of TP53 mutations is associated with poor survival and an EMT signature in gliosarcoma patients," (in eng), *Exp Mol Med,* vol. 49, no. 4, p. e317, Apr 14 2017.

[83] B. Philip, K. Ito, R. Moreno-Sánchez, and S. J. Ralph, "HIF expression and the role of hypoxic microenvironments within primary tumours as protective sites driving cancer stem cell renewal and metastatic progression," (in eng), *Carcinogenesis,* vol. 34, no. 8, pp. 1699-707, Aug 2013.

[84] J. Chen *et al.*, "Snail recruits Ring1B to mediate transcriptional repression and cell migration in pancreatic cancer cells," (in eng), *Cancer Res,* vol. 74, no. 16, pp. 4353-63, Aug 15 2014.

[85] M. Mohd Faheem *et al.*, "Par-4 mediated Smad4 induction in PDAC cells restores canonical TGF-β/ Smad4 axis driving the cells towards lethal EMT," (in eng), *Eur J Cell Biol,* vol. 99, no. 4, p. 151076, May 2020.

[86] Q. Xu *et al.*, "α-Mangostin suppresses the viability and epithelial-mesenchymal transition of pancreatic cancer cells by downregulating the PI3K/Akt pathway," (in eng), *Biomed Res Int,* vol. 2014, p. 546353, 2014.

[87] S. A. Mani *et al.*, "The epithelial-mesenchymal transition generates cells with properties of stem cells," (in eng), *Cell,* vol. 133, no. 4, pp. 704-15, May 16 2008.

[88] D. Witte *et al.*, "Negative regulation of TGF-β1-induced MKK6-p38 and MEK-ERK signalling and epithelial-mesenchymal transition by Rac1b," (in eng), *Sci Rep,* vol. 7, no. 1, p. 17313, Dec 11 2017.

[89] K. Aigner *et al.*, "The transcription factor ZEB1 (deltaEF1) promotes tumour cell dedifferentiation by repressing master regulators of epithelial polarity," (in eng), *Oncogene,* vol. 26, no. 49, pp. 6979-88, Oct 25 2007.

[90] X. Zheng *et al.*, "Epithelial-to-mesenchymal transition is dispensable for metastasis but induces chemoresistance in pancreatic cancer," (in eng), *Nature,* vol. 527, no. 7579, pp. 525-530, Nov 26 2015.

[91] Y. Shichi *et al.*, "Enhanced morphological and functional differences of pancreatic cancer with epithelial or mesenchymal characteristics in 3D culture," (in eng), *Sci Rep,* vol. 9, no. 1, p. 10871, Jul 26 2019.

[92] P. Zhou *et al.*, "NMIIA promotes tumor growth and metastasis by activating the Wnt/β-catenin signaling pathway and EMT in pancreatic cancer," (in eng), *Oncogene,* vol. 38, no. 27, pp. 5500-5515, Jul 2019.

[93] S. D'Amico, V. Kirillov, O. Petrenko, and N. C. Reich, "STAT3 is a genetic modifier of TGF-beta induced EMT in KRAS mutant pancreatic cancer," (in eng), *bioRxiv,* Sep 5 2023.

[94] C. Güngör *et al.*, "Notch signaling activated by replication stress-induced expression of midkine drives epithelial-mesenchymal transition and chemoresistance in pancreatic cancer," (in eng), *Cancer Res,* vol. 71, no. 14, pp. 5009-19, Jul 15 2011.

[95] M. Fukata and K. Kaibuchi, "Rho-family GTPases in cadherin-mediated cell-cell adhesion," (in eng), *Nat Rev Mol Cell Biol,* vol. 2, no. 12, pp. 887-97, Dec 2001.

[96] J. Wojnacki, G. Quassollo, M. P. Marzolo, and A. Cáceres, "Rho GTPases at the crossroad of signaling networks in mammals: impact of Rho-GTPases on microtubule organization and dynamics," (in eng), *Small GTPases,* vol. 5, p. e28430, 2014.

[97] A. Hall, "Rho GTPases and the actin cytoskeleton," *Science,* vol. 279, no. 5350, pp. 509-514, 1998.

[98] L. Van Aelst and M. Symons, "Role of Rho family GTPases in epithelial morphogenesis," (in eng), *Genes Dev,* vol. 16, no. 9, pp. 1032-54, May 1 2002.

[99] J. V. Small, K. Rottner, I. Kaverina, and K. I. Anderson, "Assembling an actin cytoskeleton for cell attachment and movement," (in eng), *Biochim Biophys Acta,* vol. 1404, no. 3, pp. 271-81, Sep 16 1998.

[100] A. Boureux, E. Vignal, S. Faure, and P. Fort, "Evolution of the Rho family of ras-like GTPases in eukaryotes," (in eng), *Mol Biol Evol,* vol. 24, no. 1, pp. 203-16, Jan 2007.

[101] K. L. Rossman, C. J. Der, and J. Sondek, "GEF means go: turning on RHO GTPases with guanine nucleotide-exchange factors," (in eng), *Nat Rev Mol Cell Biol,* vol. 6, no. 2, pp. 167-80, Feb 2005.

[102] S. Y. Moon and Y. Zheng, "Rho GTPase-activating proteins in cell regulation," (in eng), *Trends Cell Biol,* vol. 13, no. 1, pp. 13-22, Jan 2003.

[103] B. Olofsson, "Rho guanine dissociation inhibitors: pivotal molecules in cellular signalling," (in eng), *Cell Signal,* vol. 11, no. 8, pp. 545-54, Aug 1999.

[104] T. Ishizaki *et al.*, "p160ROCK, a Rho-associated coiled-coil forming protein kinase, works downstream of Rho and induces focal adhesions," (in eng), *FEBS Lett,* vol. 404, no. 2-3, pp. 118-24, Mar 10 1997.

[105] T. Shimizu, K. Ihara, R. Maesaki, M. Amano, K. Kaibuchi, and T. Hakoshima, "Parallel coiled-coil association of the RhoA-binding domain in Rho-kinase," (in eng), *J Biol Chem,* vol. 278, no. 46, pp. 46046-51, Nov 14 2003.

[106] W. Wen, W. Liu, J. Yan, and M. Zhang, "Structure basis and unconventional lipid membrane binding properties of the PH-C1 tandem of rho kinases," (in eng), *J Biol Chem,* vol. 283, no. 38, pp. 26263-73, Sep 19 2008.

[107] T. Leung, X. Q. Chen, E. Manser, and L. Lim, "The p160 RhoA-binding kinase ROK alpha is a member of a kinase family and is involved in the reorganization of the cytoskeleton," (in eng), *Mol Cell Biol,* vol. 16, no. 10, pp. 5313-27, Oct 1996.

[108] M. Amano *et al.*, "Formation of actin stress fibers and focal adhesions enhanced by Rho-kinase," (in eng), *Science,* vol. 275, no. 5304, pp. 1308-11, Feb 28 1997.

[109] M. Sebbagh, C. Renvoizé, J. Hamelin, N. Riché, J. Bertoglio, and J. Bréard, "Caspase-3-mediated cleavage of ROCK I induces MLC phosphorylation and apoptotic membrane blebbing," (in eng), *Nat Cell Biol,* vol. 3, no. 4, pp. 346-52, Apr 2001.

[110] M. Sebbagh, J. Hamelin, J. Bertoglio, E. Solary, and J. Bréard, "Direct cleavage of ROCK II by granzyme B induces target cell membrane blebbing in a caspase-independent manner," (in eng), *J Exp Med,* vol. 201, no. 3, pp. 465-71, Feb 7 2005.

[111] H. Miki, H. Yamaguchi, S. Suetsugu, and T. Takenawa, "IRSp53 is an essential intermediate between Rac and WAVE in the regulation of membrane ruffling," (in eng), *Nature,* vol. 408, no. 6813, pp. 732-5, Dec 7 2000.

[112] S. Krugmann, I. Jordens, K. Gevaert, M. Driessens, J. Vandekerckhove, and A. Hall, "Cdc42 induces filopodia by promoting the formation of an IRSp53:Mena complex," (in eng), *Curr Biol,* vol. 11, no. 21, pp. 1645-55, Oct 30 2001.

[113] F. P. Lai *et al.*, "Arp2/3 complex interactions and actin network turnover in lamellipodia," (in eng), *Embo j,* vol. 27, no. 7, pp. 982-92, Apr 9 2008.

[114] H. Miki, T. Sasaki, Y. Takai, and T. Takenawa, "Induction of filopodium formation by a WASP-related actin-depolymerizing protein N-WASP," (in eng), *Nature,* vol. 391, no. 6662, pp. 93-6, Jan 1 1998.

[115] N. Nakamura *et al.*, "Phosphorylation of ERM proteins at filopodia induced by Cdc42," (in eng), *Genes Cells,* vol. 5, no. 7, pp. 571-81, Jul 2000.

[116] D. C. Edwards, L. C. Sanders, G. M. Bokoch, and G. N. Gill, "Activation of LIM-kinase by Pak1 couples Rac/Cdc42 GTPase signalling to actin cytoskeletal dynamics," (in eng), *Nat Cell Biol,* vol. 1, no. 5, pp. 253-9, Sep 1999.

[117] A. B. Jaffe and A. Hall, "Rho GTPases: biochemistry and biology," (in eng), *Annu Rev Cell Dev Biol,* vol. 21, pp. 247-69, 2005.

[118] M. Schenk, B. Aykut, C. Teske, N. A. Giese, J. Weitz, and T. Welsch, "Salinomycin inhibits growth of pancreatic cancer and cancer cell migration by disruption of actin stress fiber integrity," (in eng), *Cancer Lett,* vol. 358, no. 2, pp. 161-169, Mar 28 2015.

[119] K. Fujimura, S. Choi, M. Wyse, J. Strnadel, T. Wright, and R. Klemke, "Eukaryotic Translation Initiation Factor 5A (EIF5A) Regulates Pancreatic Cancer Metastasis by Modulating RhoA and Rho-associated Kinase (ROCK) Protein Expression Levels," (in eng), *J Biol Chem,* vol. 290, no. 50, pp. 29907-19, Dec 11 2015.

[120] R. Zinn, H. Otterbein, H. Lehnert, and H. Ungefroren, "RAC1B: A Guardian of the Epithelial Phenotype and Protector Against Epithelial-Mesenchymal Transition," (in eng), *Cells,* vol. 8, no. 12, Dec 4 2019.

[121] M. Shigeta, N. Sanzen, M. Ozawa, J. Gu, H. Hasegawa, and K. Sekiguchi, "CD151 regulates epithelial cell-cell adhesion through PKC- and Cdc42-dependent actin cytoskeletal reorganization," (in eng), *J Cell Biol,* vol. 163, no. 1, pp. 165-76, Oct 13 2003.

[122] S. H. Kim, Z. Li, and D. B. Sacks, "E-cadherin-mediated cell-cell attachment activates Cdc42," (in eng), *J Biol Chem,* vol. 275, no. 47, pp. 36999-7005, Nov 24 2000.

[123] C. D. Nobes and A. Hall, "Rho, rac, and cdc42 GTPases regulate the assembly of multimolecular focal complexes associated with actin stress fibers, lamellipodia, and filopodia," (in eng), *Cell,* vol. 81, no. 1, pp. 53-62, Apr 7 1995.

[124] C. D. Lawson and A. J. Ridley, "Rho GTPase signaling complexes in cell migration and invasion," (in eng), *J Cell Biol,* vol. 217, no. 2, pp. 447-457, Feb 5 2018.

[125] G. L. Razidlo, K. M. Burton, and M. A. McNiven, "Interleukin-6 promotes pancreatic cancer cell migration by rapidly activating the small GTPase CDC42," (in eng), *J Biol Chem,* vol. 293, no. 28, pp. 11143-11153, Jul 13 2018.

[126] C. J. Groger, M. Grubinger, T. Waldhor, K. Vierlinger, and W. Mikulits, "Meta-analysis of gene expression signatures defining the epithelial to mesenchymal transition during cancer progression," *PLoS One,* vol. 7, no. 12, p. e51136, 2012.

[127] Q. Zhou *et al.*, "Altered histone acetylation patterns in pancreatic cancer cell lines induce subtype-specific transcriptomic and phenotypical changes," (in eng), *Int J Oncol,* vol. 64, no. 3, Mar 2024.

[128] G. Lomberk *et al.*, "Distinct epigenetic landscapes underlie the pathobiology of pancreatic cancer subtypes," (in eng), *Nat Commun,* vol. 9, no. 1, p. 1978, May 17 2018.

[129] J. A. Alberts B, Lewis J, et al., *Molecular Biology of the Cell*. New York: New York: Garland Science, 2002.

[130] E. K. Rajakylä *et al.*, "Assembly of Peripheral Actomyosin Bundles in Epithelial Cells Is Dependent on the CaMKK2/AMPK Pathway," (in eng), *Cell Rep,* vol. 30, no. 12, pp. 4266-4280.e4, Mar 24 2020.

[131] S. K. Wu *et al.*, "Cortical F-actin stabilization generates apical-lateral patterns of junctional contractility that integrate cells into epithelia," (in eng), *Nat Cell Biol,* vol. 16, no. 2, pp. 167-78, Feb 2014.

[132] T. Vallenius, "Actin stress fibre subtypes in mesenchymal-migrating cells," (in eng), *Open Biol,* vol. 3, no. 6, p. 130001, Jun 19 2013.

[133] J. Haynes, J. Srivastava, N. Madson, T. Wittmann, and D. L. Barber, "Dynamic actin remodeling during epithelial-mesenchymal transition depends on increased moesin expression," (in eng), *Mol Biol Cell,* vol. 22, no. 24, pp. 4750-64, Dec 2011.

[134] N. A. Bhowmick *et al.*, "Transforming growth factor-beta1 mediates epithelial to mesenchymal transdifferentiation through a RhoA-dependent mechanism," (in eng), *Mol Biol Cell,* vol. 12, no. 1, pp. 27-36, Jan 2001.

[135] H. Ungefroren, D. Witte, and H. Lehnert, "The role of small GTPases of the Rho/Rac family in TGF-β-induced EMT and cell motility in cancer," (in eng), *Dev Dyn,* vol. 247, no. 3, pp. 451-461, Mar 2018.

[136] A. Hall, "Rho GTPases and the actin cytoskeleton," (in eng), *Science,* vol. 279, no. 5350, pp. 509-14, Jan 23 1998.

[137] R. L. Juliano, "Signal transduction by cell adhesion receptors and the cytoskeleton: functions of integrins, cadherins, selectins, and immunoglobulin-superfamily members," (in eng), *Annu Rev Pharmacol Toxicol,* vol. 42, pp. 283-323, 2002.

[138] C. Y. Yeung *et al.*, "Arhgap28 is a RhoGAP that inactivates RhoA and downregulates stress fibers," (in eng), *PLoS One,* vol. 9, no. 9, p. e107036, 2014.

[139] K. Riento, R. M. Guasch, R. Garg, B. Jin, and A. J. Ridley, "RhoE binds to ROCK I and inhibits downstream signaling," (in eng), *Mol Cell Biol,* vol. 23, no. 12, pp. 4219-29, Jun 2003.

[140] C. D. Nobes, I. Lauritzen, M. G. Mattei, S. Paris, A. Hall, and P. Chardin, "A new member of the Rho family, Rnd1, promotes disassembly of actin filament structures and loss of cell adhesion," (in eng), *J Cell Biol,* vol. 141, no. 1, pp. 187-97, Apr 6 1998.

[141] C. D. Qin *et al.*, "The Rho GTPase Rnd1 inhibits epithelial-mesenchymal transition in hepatocellular carcinoma and is a favorable anti-metastasis target," (in eng), *Cell Death Dis,* vol. 9, no. 5, p. 486, May 1 2018.

[142] M. Maeda *et al.*, "ARHGAP18, a GTPase-activating protein for RhoA, controls cell shape, spreading, and motility," (in eng), *Mol Biol Cell,* vol. 22, no. 20, pp. 3840-52, Oct 2011.

[143] M. Amano *et al.*, "Myosin II activation promotes neurite retraction during the action of Rho and Rho-kinase," (in eng), *Genes Cells,* vol. 3, no. 3, pp. 177-88, Mar 1998.

[144] H. P. Atlas. (2023.06.19). *Location of protein RhoA (2023.06.19 ed.)*. Available: https://www.proteinatlas.org/ENSG00000067560-RHOA/subcellular

[145] P. J. Thul *et al.*, "A subcellular map of the human proteome," (in eng), *Science,* vol. 356, no. 6340, May 26 2017.

[146] A. D. Dubash, C. Guilluy, M. C. Srougi, E. Boulter, K. Burridge, and R. García-Mata, "The small GTPase RhoA localizes to the nucleus and is activated by Net1 and DNA damage signals," (in eng), *PLoS One,* vol. 6, no. 2, p. e17380, Feb 24 2011.

[147] T. Tanaka *et al.*, "Nuclear Rho kinase, ROCK2, targets p300 acetyltransferase," (in eng), *J Biol Chem,* vol. 281, no. 22, pp. 15320-9, Jun 2 2006.

[148] J. Xu, Y. Li, X. Yang, Y. Chen, and M. Chen, "Nuclear translocation of small G protein RhoA via active transportation in gastric cancer cells," (in eng), *Oncol Rep,* vol. 30, no. 4, pp. 1878-82, Oct 2013.

[149] Y. Li, Y. Hu, L. Che, J. Jia, and M. Chen, "Nucleolar localization of Small G protein RhoA is associated with active RNA synthesis in human carcinoma HEp-2 cells," (in eng), *Oncol Lett,* vol. 11, no. 6, pp. 3605-3610, Jun 2016.

[150] J. Stricker, Y. Beckham, M. W. Davidson, and M. L. Gardel, "Myosin II-mediated focal adhesion maturation is tension insensitive," (in eng), *PLoS One,* vol. 8, no. 7, p. e70652, 2013.

[151] Z. Zhang *et al.*, "Direct Rho-associated kinase inhibition [correction of inhibiton] induces cofilin dephosphorylation and neurite outgrowth in PC-12 cells," (in eng), *Cell Mol Biol Lett,* vol. 11, no. 1, pp. 12-29, 2006.

[152] A. Aghdassi *et al.*, "Recruitment of histone deacetylases HDAC1 and HDAC2 by the transcriptional repressor ZEB1 downregulates E-cadherin expression in pancreatic cancer," (in eng), *Gut,* vol. 61, no. 3, pp. 439-48, Mar 2012.

[153] J. von Burstin *et al.*, "E-cadherin regulates metastasis of pancreatic cancer in vivo and is suppressed by a SNAIL/HDAC1/HDAC2 repressor complex," (in eng), *Gastroenterology,* vol. 137, no. 1, pp. 361-71, 371.e1-5, Jul 2009.

[154] S. C. Tsai and E. Seto, "Regulation of histone deacetylase 2 by protein kinase CK2," (in eng), *J Biol Chem,* vol. 277, no. 35, pp. 31826-33, Aug 30 2002.

[155] J. M. Sun, H. Y. Chen, and J. R. Davie, "Differential distribution of unmodified and phosphorylated histone deacetylase 2 in chromatin," (in eng), *J Biol Chem,* vol. 282, no. 45, pp. 33227-36, Nov 9 2007.

[156] J. Pietrzak, T. Płoszaj, Ł. Pułaski, and A. Robaszkiewicz, "EP300-HDAC1-SWI/SNF functional unit defines transcription of some DNA repair enzymes during differentiation of human macrophages," (in eng), *Biochim Biophys Acta Gene Regul Mech,* vol. 1862, no. 2, pp. 198-208, Feb 2019.

[157] H. Ono *et al.*, "C646 inhibits G2/M cell cycle-related proteins and potentiates anti-tumor effects in pancreatic cancer," (in eng), *Sci Rep,* vol. 11, no. 1, p. 10078, May 12 2021.

[158] H. S. Lee *et al.*, "A novel HDAC inhibitor, CG200745, inhibits pancreatic cancer cell growth and overcomes gemcitabine resistance," (in eng), *Sci Rep,* vol. 7, p. 41615, Jan 30 2017.

[159] M. H. Cai *et al.*, "Depletion of HDAC1, 7 and 8 by Histone Deacetylase Inhibition Confers Elimination of Pancreatic Cancer Stem Cells in Combination with Gemcitabine," (in eng), *Sci Rep,* vol. 8, no. 1, p. 1621, Jan 26 2018.

[160] I. Maietta, A. Martínez-Pérez, R. Álvarez, R. De Lera Á, Á. González-Fernández, and R. Simón-Vázquez, "Synergistic Antitumoral Effect of Epigenetic Inhibitors and Gemcitabine in Pancreatic Cancer Cells," (in eng), *Pharmaceuticals (Basel),* vol. 15, no. 7, Jul 2 2022.

[161] S. S. Nagaraja, V. Krishnamoorthy, R. Raviraj, A. Paramasivam, and D. Nagarajan, "Effect of Trichostatin A on radiation induced epithelial-mesenchymal transition in A549 cells," (in eng), *Biochem Biophys Res Commun,* vol. 493, no. 4, pp. 1534-1541, Dec 2 2017.

[162] J. Wang, M. Q. Xu, X. L. Jiang, X. Y. Mei, and X. G. Liu, "Histone deacetylase inhibitor SAHA-induced epithelial-mesenchymal transition by upregulating Slug in lung cancer cells," (in eng), *Anticancer Drugs,* vol. 29, no. 1, pp. 80-88, Jan 2018.

[163] D. Lazarova and M. Bordonaro, "ZEB1 Mediates Drug Resistance and EMT in p300-Deficient CRC," (in eng), *J Cancer,* vol. 8, no. 8, pp. 1453-1459, 2017.

[164] A. B. McLeod, J. P. Stice, S. E. Wardell, H. M. Alley, C. Y. Chang, and D. P. McDonnell, "Validation of histone deacetylase 3 as a therapeutic target in castration-resistant prostate cancer," (in eng), *Prostate,* vol. 78, no. 4, pp. 266-277, Mar 2018.

[165] E. Hessmann *et al.*, "Fibroblast drug scavenging increases intratumoural gemcitabine accumulation in murine pancreas cancer," (in eng), *Gut,* vol. 67, no. 3, pp. 497-507, Mar 2018.

[166] F. H. Hamdan and S. A. Johnsen, "Epigenetic Targeting of Aberrant Transcriptional Modulation in Pancreatic Cancer," *Epigenomes,* vol. 2, no. 2, p. 8, 2018.

Supplementary

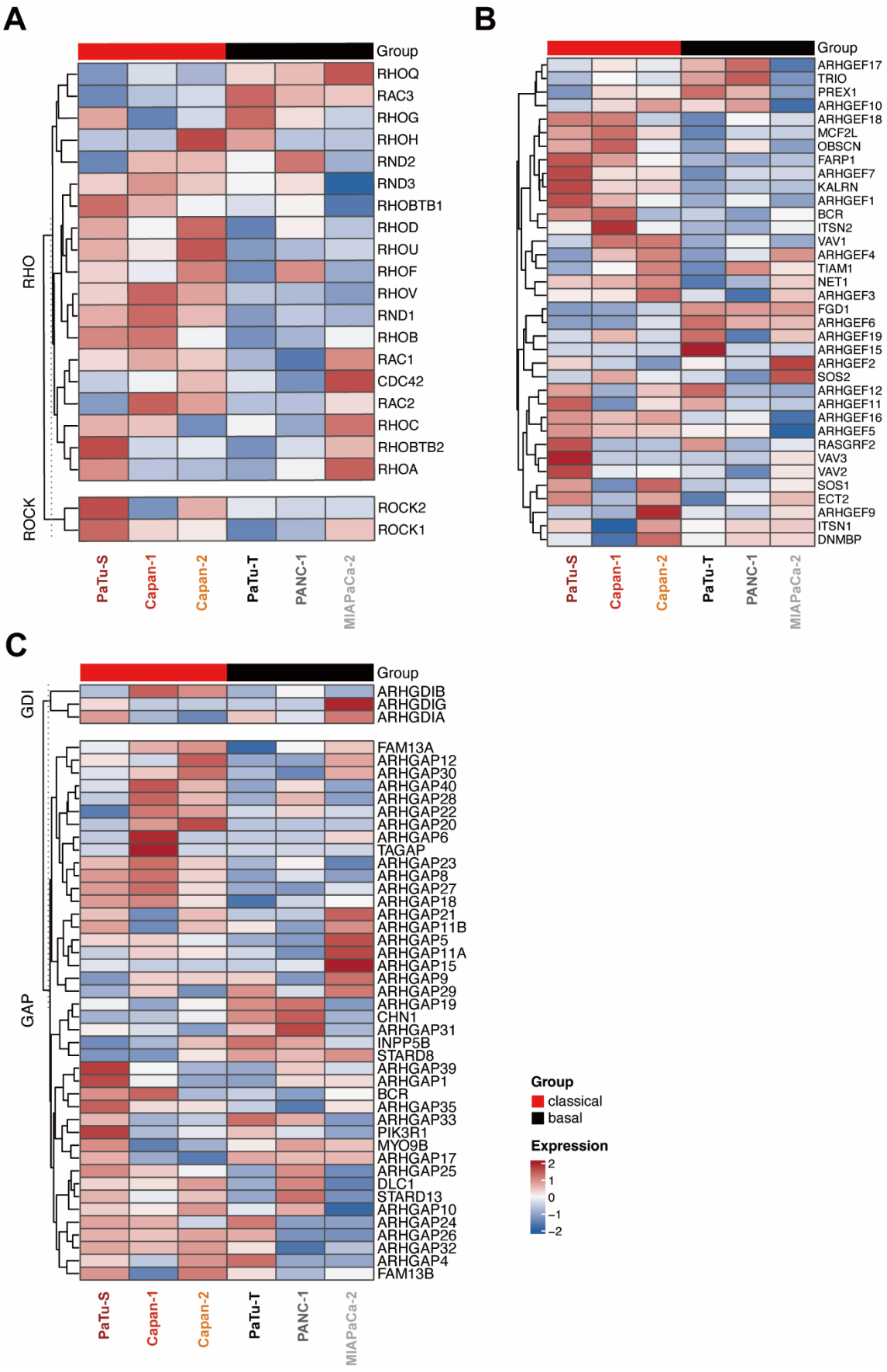

Figure S1: Transcriptional patterns of Rho signaling components in classical and basal-like cell lines. (A) Heatmap was generated from RNA-seq data to display transcriptional patterns of Rho-GTPase family in classical cell lines PaTu-S, Capan-1 and Capan-2, and basal-like cell lines PaTu-T, PANC-1 and MIAPaCa-2. **(B)** Heatmap of Rho-GEFs in classical cell lines PaTu-S, Capan-1 and Capan-2, and basal-like cell lines PaTu-T, PANC-1 and MIAPaCa-2. **(C)** Heatmap of Rho-GAPs and Rho-GDIs in classical cell lines PaTu-S, Capan-1 and Capan-2, and basal-like cell lines PaTu-T, PANC-1 and MIAPaCa-2. DEGs were selected based on logFC > 1 and $p < 0.05$.

Acknowledgement

First of all, I would like to thank everyone who has helped me in my research progress. The experience in the Med 2 lab will be an important and pleasant memory in my life.

My deepest and sincerest gratitude goes to my supervisor, **PD Dr. Ivonne Regel**. She has been the best mentor I have ever encountered, providing exceptional guidance and support throughout my academic journey. She was always patient in reviewing and correcting my posters, figure preparation, and writing, and she never put pressure on me during my work in the lab. What impressed me most was not only her academic guidance but also her personality. Her kindness, friendliness, and attitude towards students made me admire her even more. I also feel very lucky to be her student.

Besides my supervisor, I would like to express my gratitude to **Prof. Dr. Roland Kappler** and **Prof. Dr. Julia Mayerle**, who served as my thesis advisory committee (TAC) members, for their insightful suggestions on my project during the TAC meeting and lab meeting.

I would like to thank **PD Dr. Ujwal Mukund Mahajan** for his invaluable suggestions and assistance with data analysis. His knowledge greatly improved the efficiency of my work.

I am also grateful to my dear colleagues, **Lisa Fahr**, **Prince Allawadhi**, and **Ahmed Alnatsha, Nicole Schreiner** and **Julia Wolff** for their assistance with my experiments and for giving me advice on troubleshooting. Their collaboration and insights were essential to my research progress. They are not only my colleagues but also my close friends. A heartfelt thank you to technician **Maria Escobar**, who taught me cell culture techniques and provided continuous support and assistance during my experiments. I am also grateful to technician **Simon Gahr** for his support and help in lab. I would like to thank **Qi Li** and **Yonggan Xue** for their help and advice when I started working at the lab and express my gratitude to **Jianying Xu, Tianjun Song and Tahib Habsh** for our friendship. I extend my thanks to all my lab mates for their kindness, support, and assistance. I am very happy to discuss academics and share the joy of life with them.

Lastly, I would like to express my sincere gratitude to my mother and my friends for their unwavering support and understanding. They always listened to my complaints and fixed my anxiety.

Affidavit

Zhou, Quan

Surname, first name

I hereby declare, that the submitted thesis entitled

Comparative analysis of Rho-GTPase pathway dynamics and epigenetic drug responses in subtype-specific pancreatic cancer cell lines

is my own work. I have only used the sources indicated and have not made unauthorised use of services of a third party. Where the work of others has been quoted or reproduced, the source is always given.

I further declare that the dissertation presented here has not been submitted in the same or similar form to any other institution for the purpose of obtaining an academic degree.

Shanghai, China, 10.12.2024

Place, Date

Quan Zhou

Signature doctoral candidate

LMU LUDWIG-MAXIMILIANS-UNIVERSITÄT MÜNCHEN

Dean's Office Medical Faculty
Doctoral Office

Confirmation of congruency between printed and electronic version of the doctoral thesis

Zhou, Quan

Surname, first name

I hereby declare that the electronic version of the submitted thesis, entitled

Comparative analysis of Rho-GTPase pathway dynamics and epigenetic drug responses in subtype-specific pancreatic cancer cell lines

is congruent with the printed version both in content and format.

Shanghai, China, 11.12.2024

Place, Date

Quan Zhou

Signature doctoral candidate